High-Order Methods On Mixed-Element Unstructured Meshes For Aeronautical Applications

Antonios Foivos Antoniadis

Submitted for the Degree of Ph.D.

Department of Engineering Physics
Cranfield University
Cranfield, UK

2012

Cranfield University

School of Engineering

Department of Engineering Physics

PhD Candidate

Antonios Foivos Antoniadis

High-Order Methods On Mixed-Element Unstructured Meshes For Aeronautical Applications

Supervisors: Prof. Dimitris Drikakis and Dr. Nikolaos Asproulis

November 2012

Abstract

Higher resolution and reliability are the desiderata for Computational Fluid Dynamics and main drivers for the development, implementation and validation of high-order accurate methods. Complex fluid dynamic phenomena such as shock-wave boundary-layer interactions, turbulent separated flows and fluid problems involving multiple scales are adequately resolved with high-order schemes. The spatial representation of the flow field by an unstructured mesh provides flexibility, automation, fast and effortless grid generation and exceptional load balance on multiple processor computers. This plethora of advantages is mirrored by the unprecedented popularity of unstructured-based schemes.

The objective of this PhD project is the implementation of two high-order schemes for the compressible Navier-Stokes equations in the context of the finite volume "k-exact" framework: the MUSCL-TVD and WENO. The schemes are formulated in two and three space dimensions for mixed-element unstructured meshes; in addition, the Spalart-Allmaras turbulence model is implemented into the developed numerical framework. A wide range of applications are considered spanning from low-speed flows ($M = 0.08$) to supersonic conditions ($M = 5.0$); inviscid and viscous simulations in a broad spectrum of Reynolds numbers ranging from $Re = 500$ up to $Re = 37 \times 10^6$. The applications include: the Taylor-Green vortex, the ONERA-M6 wing, flat plate, the NACA-0012 and the MD 30P-30N aerofoils, and a shock-wave boundary-layer interaction.

For the examined cases, WENO schemes demonstrate superior accuracy, numerical dissipation and non-oscillatory behaviour over the MUSCL-TVD. High-order schemes inherit low numerical dissipation properties while turbulence models induce dissipation, this disequilibrium has adverse effects on the stability, convergence and accuracy of the simulation; therefore, turbulence model re-calibration would be required in order to accommodate high-order discretisation methods.

Acknowledgements

I would like to express my gratitude to Prof. Dimitris Drikakis for providing the guidance, support, encouragement and vision all along the course of the project. I would like also to thank Dr. Nikolaos Asproulis for his friendship, moral support, mathematical and technical advisements, Dr. Vladimir Titarev for the guidance and expertise on high-order methods and gas dynamics, Dr. Ioannis Kokkinakis for the interesting and fruitful conversations on fluid mechanics, Kasif Iqbal for his insights in the DG philosophy, Ramey Jamil for his professional latex skills, Dr. Antonis Milonas for sharing his knowledge in large eddy simulation, Dr. Vassilis Moraris for the aerodynamic know-hows, Dr. Christos Vamvakoulas and Dr. Marco Hahn for the advises on grid generation and Dr. Benjamin Obadia for his support and motivation.

I am sincerely thankful to Dr. Panagiotis Tsoutsanis for his friendship, support, help and guidance in programming, numerics, fluid mechanics, linux, HPC ... His contribution was fundamental for this research project.

I would like also to thank my dear friend and house-mate Thanos for inspiring me to embark on this PhD. I am deeply thankful to Reem for her love and understanding.

Last but not least, I would like to thank my parents Elena and Christos, their support even from abroad was essential and my brother Marios for his continuous belief in me.

Contents

List of Figures

List of Tables

Nomenclature

Symbols

γ	Ratio of specific heats
λ	Second viscosity coefficient
μ_l	Laminar dynamic viscosity
ω_β	Gaussian quadrature weights
ρ	Density
$\tau_{xx}, \tau_{yy}, \tau_{zz}$	Normal stresses
$\tau_{xy}, \tau_{xz}, \tau_{yz}$	Shear stresses
x_β	Gaussian quadrature point coordinates
$\vec{F}^{\mathrm{c}}$	Vector of inviscid fluxes
$\vec{F}^{\mathrm{v}}$	Vector of viscous fluxes
$\vec{n}$	Unit normal vector of element's face (pointing outwards) with Cartesian components n_x, n_y, n_z
$\vec{W}$	Vector of conserved variables
B	Total number of Gaussian quadrature points per element
dA	Area of surface
E	Total energy
i	Index of considered element
J_i	Total number of surfaces of i

p	Pressure
P_r	Prandtl number
S_u	Sutherland constant
T	Temperature
u, v, w	Cartesian components of velocity
V_i	Volume of element with index i
x, y, z	Cartesian coordinates
$\mathcal{V}$	Contravariant velocity

Acronyms

ALE	Arbitrary Lagrangian Eulerian method
BC	Boundary Condition
CAD	Computer Aided Design method
CFD	Computational Fluid Dynamics
DG	Discontinuous Galerkin method
DOF	Degree Of Freedom
ENO	Essentially Non-Oscillatory scheme
FD	Finite Difference method
FE	Finite Element method
FV	Finite Volume method
GOAHEAD	Generation Of Advanced Helicopter Experimental Aerodynamic Database for CFD code validation
HLLC	Harten, Lax, and van Leer Riemann solver plus Contact wave
HPC	High Performance Computing

MP	Monotonicity Preserving method
MUSCL	Monotone Upwind-centered Schemes for Conservation Laws
NS	Navier-Stokes equations
PDE	Partial Differential Equations
RANS	Reynolds Average Navier-Stokes
RD	Residual Distribution method
SA	Spalart-Allmaras turbulence model
SBP	Summation By Part method
SD	Spectral Difference method
SE	Spectral Element method
SSM	Staggered Spectral Methods
SV	Spectral Volume method
SWBLI	Shock-Wave Boundary-Layer Interaction
TVD	Total Variation Diminishing scheme
WENO	Weighted Essentially Non-Oscillatory scheme

CHAPTER 1

INTRODUCTION

1.1 Introduction to CFD

Computational Fluid Dynamics (CFD) is a multidisciplinary area with a broad range of applications; it is considered to be a conventional engineering tool while simultaneously being the subject of state-of-the-art research. Since the outbreak of the microchip in the mid of the 20^{th} century, CFD has become the ultimate tool for solving complex fluid dynamics problems, which are practically impossible to reproduce in an experiment or wind-tunnel e.g. re-entry of space-shuttle. The fundamental goal of modern CFD software is the complete automation of multi-disciplinary design processes with robust, efficient and ease-to-use simulation methods for a broad range of applications [1], accurately resolving at least the large energy-containing scales of motion.

CFD commenced in the core of the aeronautical/aerospace society; nevertheless, nowadays scientific breakthroughs are conceived and put in to practice with CFD. Recent notable studies in several scientific areas are given to demonstrate the multidisciplinary applicability of CFD; in the renewable industry, for the simulation of wake aerodynamics of wind turbines [2], for environmental and atmospheric flows such as contaminants in rivers [3], for the efficient ventilation in buildings [4], for oxi-coal carbon capture [5], for assessing the risk of hydrogen containers systems [6], for the development of polymer electrolyte membrane fuel cells [7], for the design of prosthetic cardiovascular devices [8, 9], for the drug release in adjacent human tissues [10] and

in the food processing industry [11]. In Europe, numerous initiatives from national aeronautic/aerospace agencies with the support of the European Commission have been producing extensive experimental databases enabling CFD code developers to validate their solvers. This movement increases the confidence level of the relatively inexpensive numerical simulations by bringing together program developers, physical scientists, application engineers and experimentalists [12, 13].

For certain aeronautical flows, the physical state of the fluid undergoes substantial changes; coupled with the fact that the error tolerance in aircraft design is considerably smaller relative to other engineering fields makes the aeronautical industry the main driver for the development of CFD methods including: numerical algorithms, grid generation and adaptation techniques, visualisation and turbulence models [14]. Conventional 2^{nd}-order methods encountered in most commercial software introduce higher uncertainty and numerical error, and fail to capture important flow phenomena [15, 16]. For instance, when 2^{nd}-order accurate methods are employed in helicopter aerodynamics, the unsteady interactions of blade vortices remain eminently unresolved, due to the excessive inherited numerical dissipation of the scheme [17]. High-order ($> 2^{nd}$) methods have been proven to perform better than the low-order ones, providing better results in terms of accuracy and overall performance [15, 18, 19]. For applications that require a relatively low error level, high-order methods are more cost efficient than their low-order counterparts, as illustrated in Figure 1.1.

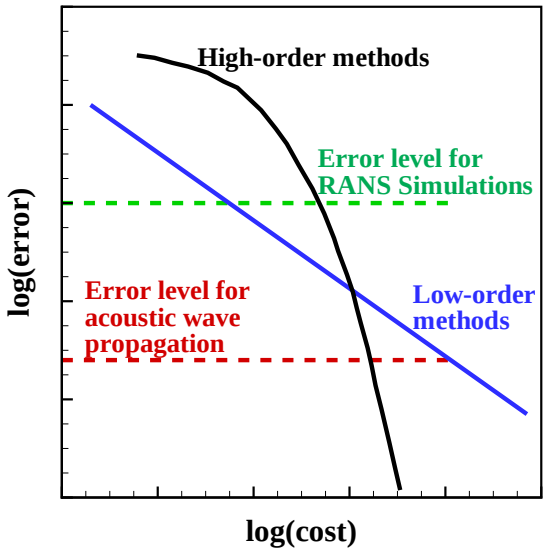

Figure 1.1: Generic error versus cost plotted for high-order and low-order methods (reproduced from [15])

For the last two decades high-order methods have become increasingly popular for computational fluid dynamics problems such as turbulent boundary layer, aeroacoustics, vortical flows and shock-wave boundary layer interactions. High-order methods are based on several mathematical formulations: the Finite Volume (FV) [20–23] ,

the Finite Difference (FD) [24–26], the Finite Element (FE) [27, 28] and the Discontinuous Galerkin (DG) methods [29–32]. These fundamental frameworks form the pillars for the development of modern high-order discretisation methods; by combining aspects of each framework an abundance of sub-methods is derived, developed and applied, naming the most popular ones: the Essentially Non-Oscillatory (ENO) [33–36], the Weighted Essentially Non-Oscillatory (WENO) [37–40], the Residual Distribution (RD) [41–44], the Spectral Volume (SV) [45–47], Spectral Element (SE) [48], Spectral Difference (SD) [49–52], Staggered Spectral Methods (SSM) [53, 54], Monotonicity Preserving (MP) [55, 56], Arbitrary-Lagrangian-Eulerian (ALE) [57–59], FD Summation by Part (SBP) [60–62] and Lifting Collocation Penalty (LCP) methods [63, 64].

A single method able to excel in all CFD aspects and employed for all fluid problems does not exist. Nonetheless, there are certain methods that have seen greater popularity such as the FV method which is widely employed in both commercial softwares and scientific research. Recently, the DG method is increasingly emerging and various authors are publishing on high-order DG-RANS schemes [65–67]. Nevertheless, DG limiters are not as robust as in the FV approach; in addition the implementation of FV schemes on unstructured grids is more straightforward, this is mainly attributed to the fact that the FV method employs one degree of freedom per element; for thorough comparisons refer to the following manuscripts [68–74]. Spectral methods employ some aspect of DG, such as the solution space where element-based discontinuous polynomials are employed but differ on how the solution is updated; one beneficial characteristic of SV is that it inherits sub-element division resolution, capturing discontinuities with a smaller error. The RD method is based on the FE, as it is continuous and on the FV, for its discretisation procedure, making it ideal for steady state simulations. These methods as they have recently been developed and applied to a limited number of problems, they require to go through thorough validation process. For detailed reviews on high-order methods refer to the following publications [15, 75–77].

The fundamental requirement of a CFD simulation is the discretisation of the spatial domain: the grid (or mesh). The grid is a representation of space where the considered fluid is simulated; the grid is tesselated into finite elements (cells), in which the fluid governing equations are numerically solved. There are two main types

of grids: structured and unstructured, for the current work the latter is considered. The main advantages of unstructured grids are: quicker and easier generation of the actual grid, geometric and grid smoothness flexibility, better load balance on multiple computers and adaptivity of the numerical schemes and the grid size (hp adaptivity) [78, 79]. Over the last fifteen years, CFD unstructured grid solvers have reached a maturity level similar to that of the structured framework, making them the predominant choice for engineers and scientists undertaking practical applications with complicated geometries.

The main obstacles faced by the CFD community are not related to the actual CFD software, but rather to the time needed for the repair of the computer aided design (CAD) models. Furthermore, the indigenous physical assumptions in CFD codes and particularly in turbulence models, have adverse effects on the computed flow physics. Audaciously, the CFD community confronts these challenges with experience and intuition, working towards the dawn of a new mathematisation wave, where CFD is integrated into the design of virtual products.

1.2 Aim and Objectives

The primary aims of this research work is the development, validation and application of high-order methods on mixed-element unstructured grids in two and three spatial dimensions for the compressible Navier-Stokes (NS) equations, in detail:

- Review the state-of-the-art of high-order methods in the context of the finite volume k-exact framework.
- Extend the Monotone Upwind-centered Schemes for Conservation Laws (MUSCL) and Weighted-Essentially Non-Oscillatory (WENO) schemes for the compressible NS equations in 2D and 3D with techniques for the gradient reconstruction, viscous flux evaluation and boundary conditions.
- Implement the Spalart-Allmaras turbulence model in the developed numerical framework with local time stepping procedure.

- Address the challenges and limitations of Spalart-Allmaras model with high-order discretisation.
- Validate the developed schemes in a broad range of aeronautical applications.
  - Inviscid flows : Taylor-Green vortex flow and transonic flow over ONERA-M6 wing.
  - Laminar flows: flow over flat plate, flow past the NACA-0012 at zero incident angle and flow past the NACA-0012 at a positive angle.
  - Turbulent flows: flow over a flat plate, flow past the NACA-0012 at zero incident angle, flow past a multi-element airfoil at high incident angle and supersonic internal flow with shock-wave boundary-layer interactions phenomena.
- Compare the different numerical solutions in terms of accuracy, efficiency, robustness, grid and element-type dependencies, convergence and speed.

1.3 Thesis Contributions

A CFD solver has been extended from the Euler equations to the compressible Navier-Stokes equations for two and three space dimensions on mixed-element unstructured meshes by combining state-of-the-art algorithms and techniques across a wide spectrum of numerical frameworks; such as high-order k-exact reconstruction, MUSCL-TVD schemes, WENO schemes and the HLLC Riemann solver. The solver is written in Fortran-90 with MPI directives for parallel runs, the initial 3D solver was modified to perform 2D simulations. A least square gradient reconstruction is adopted as well as the implementation of the boundary conditions for the NS equation. The Spalart-Allmaras turbulence model has been efficiently implemented in the numerical framework and key challenges for high-order RANS discretisations have been addressed. High-order (up to 5th order) of accuracy is achieved across a wide range of applications: from low speed to supersonic flow simulations, and from laminar to highly turbulent.

1.4 Thesis Structure

The second chapter is an introduction to the NS governing equations of fluid mechanics formulated for the FV framework. Chapter 3 is devoted to the numerical methods, starting with some preliminary aspects on unstructured grid topologies and geometrical operations, followed by the basic reconstruction and coordinate transformation. Then, the Monotone Upstream-Centered Schemes for Conservation Laws with the Total Variation Diminishing (MUSCL-TVD) method and limiter, are explained followed by the high-order WENO algorithms and their implementation to characteristic variables. The treatment of the inviscid and viscous fluxes is detailed and attention is given to the implementation of boundary conditions (BC) particularly to wall-bounded elements; time discretisation forms the final section of the chapter. The Spalart-Allmaras turbulence model and discretisation techniques form the main topic of chapter 4. The applications of the developed schemes expand from Chapter 5 to 7; including, inviscid subsonic and transonic flows, moderate Reynolds number laminar flows and high Reynolds number turbulent flows; the cases are mentioned in Section 1.2. Conclusions are drawn in Chapter 8 in addition to challenges that are encountered and finally future work recommendations are advised.

Note that, all two-dimensional grids are generated with the grid generation Pointwise® [80] software, for the three-dimensional grids also the ANSYS-ICEM-CFD® [81] was employed; in-depth analysis of the grid generation strategies are given for each case. Furthermore, the partitioning of the unstructured grids is achieved with the graph-based portioning software METIS-5.0.2 [82].

1.5 Publications

During this PhD, several journal and conference articles were published, in addition, through the GOAHEAD project (Generation Of Advanced Helicopter Experimental Aerodynamic Database for CFD code validation).

Journal and Conference Publications

- A.F. Antoniadis, P. Tsoutsanis, D. Drikakis. *High – order schemes on mixed – element unstructured grids for aerodynamic flow*, 42^{nd} AIAA Fluid Dynamics Conference and Exhibit, New Orleans 2012, USA.
- A.F. Antoniadis, K.H. Iqbal, N. Asproulis, E. Shapiro, D. Drikakis. *Comparison of high – order Finite Volume and Discontinuous Galerkin methods on 3 – D unstructured grids*, 9^{th} International Conference of Numerical Analysis and Applied Mathematics, American Institute of Physics proceedings, Halkidiki, Greece 2011.
- A.F. Antoniadis , D. Drikakis, B. Zhong, G. Barakos , R. Steijl M. Biava , L. Vigevano, A. Brocklehurst , O.Boelens , M. Dietz , M. Embacher , W.Khier and T.Renaud. *Assessment of CFD methods against experimental measurements for helicopter flows*, Journal of Aerospace Science and Technology, 1270-9638, 2011.
- B. Zhong , D. Drikakis , A. Antoniadis , G. Barakos , A. Brocklehurst , O. Boelens , M. Dietz , M. Embacher , W.Khier , T.Renaud , R. Steijl , L. Vigevano. *Assessment of CFD Methods against Experimental Flow Measurements for Helicopter Flows in the GOAHEAD Project*, 36th European Rotorcraft Forum, Paris, France, September 2010.

Technical reports

- B. Zhong, A. Antoniadis, D. Drikakis. A comparison of blind-test computations with experimental data, GOAHEAD technical report, D4.3.1, October 2009.

- A. Antoniadis, B. Zhong and D. Drikakis. A comparison of post-test computations with experimental data, GOAHEAD technical report, D4.3.2, November 2009.

CHAPTER 2

GOVERNING EQUATIONS OF FLUIDS

This chapter will form the basis of the thesis, by introducing the fundamental governing equation in fluid dynamics: the compressible NS equations in three space dimensions. The equations are written in integral form for the Cartesian coordinate system; including the time dependent term, the inviscid/convective and viscous/diffusive terms; physical assumptions and empirical constants are also mentioned. Finally, the semi-discrete formulation of the NS equations, based on the finite volume discretisation method, is explained.

2.1 Navier-Stokes Equations

Fluids are governed by a set of coupled non-linear partial differential equations (PDE), describing the fundamental laws of continuum mechanics: conservation of mass, momentum and energy. The NS equations are numerically solved on a spatial domain discretised into conforming elements; the system of equations is constituted by different terms, which are treated individually according to their physical interpretation.

Consider an element with index i, with a control volume V_i, which is bounded by surfaces ∂V_i of area $A_{\partial V_i}$ and the unit normal vector on the control volume surface is defined as $\vec{n}_{\partial V_i}$, then writing the 3D NS equations in integral form in Cartesian coordinates reads

$$\frac{\partial}{\partial t}\int_{V_i}\vec{W}_i dV_i + \oint_{\partial V_i}\left[\left(\vec{F}^{\mathrm{c}} - \vec{F}^{\mathrm{v}}\right)\vec{n}_{\partial V_i}\right] dA_{\partial V_i} = 0 \tag{2.1.1}$$

where $\vec{W}_i$ is the vector of conserved variables, $\vec{F}^{\mathrm{c}}$ is the vector of inviscid fluxes and $\vec{F}^{\mathrm{v}}$ is the vector of viscous fluxes. The fluxes are evaluated on each bounded surface; note that sources term are excluded at this point; the vector of conserved variables is given by

$$\vec{W}_i = [\rho, \rho u, \rho v, \rho w, E]^T \tag{2.1.2}$$

with ρ being the density, u, v, w are the velocity Cartesian components and E is the total energy of the fluid per unit mass i.e. the sum of the internal and the kinetic energy. The equation of state for a Calorically perfect gas is adopted to close the system of equations, thus the total energy yields

$$E = \frac{p}{\gamma - 1} + \frac{1}{2}\rho(u^2 + v^2 + w^2) \tag{2.1.3}$$

where p is the total pressure and the ratio of specific heats being γ usually set to a

value of 1.4 for a perfect gas. The inviscid flux vector is defined as

$$\vec{F}^{\mathrm{c}} = \mathcal{V}\begin{bmatrix} \rho \\ \rho u \\ \rho v \\ \rho w \\ E + p \end{bmatrix} + p\begin{bmatrix} 0 \\ n_x \\ n_y \\ n_z \\ 0 \end{bmatrix} \tag{2.1.4}$$

where n_x, n_y, n_z are the Cartesian components of the unit normal vector $\vec{n}$ and $\mathcal{V}$ is the contravariant velocity vector defined as

$$\mathcal{V} = n_x u + n_y v + n_z w \tag{2.1.5}$$

the viscous fluxes written as

$$\vec{F}^{\mathrm{v}} = n_x \mathrm{V}_x + n_y \mathrm{V}_y + n_z \mathrm{V}_z \tag{2.1.6}$$

expanding the viscous fluxes components yields

$$\begin{aligned} \mathrm{V}_x &= \begin{bmatrix} 0 \\ \tau_{xx} \\ \tau_{xy} \\ \tau_{xz} \\ u\tau_{xx} + v\tau_{xy} + w\tau_{xz} - q_x \end{bmatrix}, \mathrm{V}_y = \begin{bmatrix} 0 \\ \tau_{yx} \\ \tau_{yy} \\ \tau_{yz} \\ u\tau_{yx} + v\tau_{yy} + w\tau_{yz} - q_y \end{bmatrix}, \\ \mathrm{V}_z &= \begin{bmatrix} 0 \\ \tau_{zx} \\ \tau_{zy} \\ \tau_{zz} \\ u\tau_{zx} + v\tau_{zy} + w\tau_{zz} - q_z \end{bmatrix} \end{aligned} \tag{2.1.7}$$

where the normal stresses are written as

$$\tau_{xx} = 2\mu_l \frac{\partial u}{\partial x} + \lambda\left(\frac{\partial u}{\partial x} + \frac{\partial v}{\partial y} + \frac{\partial w}{\partial z}\right) \tag{2.1.8}$$

$$\tau_{yy} = 2\mu_l \frac{\partial v}{\partial y} + \lambda\left(\frac{\partial u}{\partial x} + \frac{\partial v}{\partial y} + \frac{\partial w}{\partial z}\right) \tag{2.1.9}$$

$$\tau_{zz} = 2\mu_l \frac{\partial w}{\partial z} + \lambda \left(\frac{\partial u}{\partial x} + \frac{\partial v}{\partial y} + \frac{\partial w}{\partial z} \right) \tag{2.1.10}$$

and the shear stresses

$$\tau_{xy} = \tau_{yx} = \mu_l \left(\frac{\partial u}{\partial y} + \frac{\partial v}{\partial x} \right) \tag{2.1.11}$$

$$\tau_{xz} = \tau_{zx} = \mu_l \left(\frac{\partial u}{\partial z} + \frac{\partial w}{\partial x} \right) \tag{2.1.12}$$

$$\tau_{yz} = \tau_{zy} = \mu_l \left(\frac{\partial v}{\partial z} + \frac{\partial w}{\partial y} \right) \tag{2.1.13}$$

with the dynamic laminar viscosity being μ_l, the second viscosity coefficient being λ and by employing Stokes assumption $\lambda = -2\mu_l/3$ the heat fluxes are defined as

$$q_x = -\gamma \frac{\mu_l}{P_r (\gamma - 1)} \frac{\partial T}{\partial x} \tag{2.1.14}$$

$$q_y = -\gamma \frac{\mu_l}{P_r (\gamma - 1)} \frac{\partial T}{\partial y} \tag{2.1.15}$$

$$q_z = -\gamma \frac{\mu_l}{P_r (\gamma - 1)} \frac{\partial T}{\partial z} \tag{2.1.16}$$

where $T = p/\rho$ is the temperature, P_r being the Prandtl number usually designated to a value of 0.72. The viscosity is related to the temperature by employing Sutherland's law, which yields

$$\frac{\mu_l}{\mu_{l0}} = \left(\frac{T}{T_0} \right)^{3/2} \frac{T_0 + S_u}{T + S_u} \tag{2.1.17}$$

where S_u is the reference Sutherland temperature (in Kelvin) and μ_0 the reference viscosity at a reference temperature T_0. The reference values are taken for air at atmospheric conditions (sea level) with $\mu = 1.7894 \times 10^{-5} kg/(ms)$, $T_0 = 288.16$K and $S_u = 110.4$K.

2.2 Finite Volume Method

By numerically evaluating each element's control volume and surface integrals, the system unknowns are considered as volume-averaged values. For a non-moving grid, the time dependent term of (2.1.1) will be independent of the integral and by employing the divergence theorem the volume integrals of element i are substituted with the

surface integrals on the bounded surfaces [23], thus the semi-discrete FV formulation is casted as

$$\frac{d\vec{W}_i}{dt} = -\frac{1}{|V_i|}\left[\sum_{j=1}^{J_i}\left(\vec{F}^{\mathrm{c}}_{\vec{n},j} - \vec{F}^{\mathrm{v}}_{\vec{n},j}\right)\Delta A\right] \tag{2.2.1}$$

where J_i is the total number of bounded surfaces of the considered element, the above equation simply reads that: the sum of all area-averaged fluxes on all element's bounded surfaces for both inviscid and viscous terms, is balanced with the time rate of change of the volume-average state of the conserved vector of the considered element; integrating the inviscid and viscous flux components yields

$$\frac{d\vec{W}_i}{dt} = -\frac{1}{|V_i|}\sum_{j=1}^{J_i}\left(\int_{A_j}\vec{F}^{\mathrm{c}}_{\vec{n}}dA - \int_{A_j}\vec{F}^{\mathrm{v}}_{\vec{n}}dA\right) \tag{2.2.2}$$

The evaluation of the surface integrals for the fluxes is approximated by a numerical integration quadrature formula. The Gaussian numerical quadrature rule is employed; the physical flux becomes a numerical flux and according to the order of approximation of the spatial discretisation scheme, an appropriate order for the Gaussian quadrature is employed. The convective fluxes are expressed as

$$\int_{A_j}\vec{F}^{\mathrm{c}}_{\vec{n},j} = \sum_{\beta=1}^{B}\vec{F}^{\mathrm{c}}_{\vec{n},j}\left(\vec{W}(\mathrm{x}_\beta, t)\right)\omega_\beta|A_j| \tag{2.2.3}$$

equivalently the viscous fluxes are written as

$$\int_{A_j}\vec{F}^{\mathrm{v}}_{\vec{n},j} = \sum_{\beta=1}^{B}\vec{F}^{\mathrm{v}}_{\vec{n},j}\left(\vec{W}(\mathrm{x}_\beta, t)\right)\omega_\beta|A_j| \tag{2.2.4}$$

where B is the total number of quadrature points with coordinates x_β and weights ω_β. In the next chapter, the numerical method for the computation of fluxes is detailed and thoroughly discussed.

CHAPTER 3

NUMERICAL METHODS

Chapter 3 details the employed numerical methods, starting with preliminary introductory remarks on unstructured grids and cell-centered techniques, including elements shapes, geometrical computations, element decompositions and coordinate transformation. Then, the basic reconstruction is discussed, followed by the MUSCL-TVD method. The high-order WENO-type scheme and its implementation to arbitrary unstructured grids is explained, attention is paid to the numerics used for the evaluation of the inviscid and viscous fluxes as well as the approximation procedures for the gradients. Boundary conditions are analysed and the final section is devoted to explicit time marching algorithms and techniques.

3.1 Geometrical Considerations for Unstructured Grids

Spatial grids can be categorized in two main categories: structured and unstructured. The main difference lies in the formulation of data describing each type of grid. Structured grids employ one type of element the quadrilateral in 2D and the hexahedral in 3D; unstructured grids use additionally the triangles in 2D or convex polyhedrons and combinations of those such as tetrahedral, prisms and pyramids in 3D. In both types, the set of node coordinates and element connectivities is mapped and stored in to multi-dimensional arrays. However, for structured grids, neighboring elements in the physical grid coincide with the neighboring elements in the computational arrays whereas for unstructured grids it is not the case; additional information is required and neighbors have to be explicitly assigned [83].

In the previous chapter the FV semi-discrete formulation was introduced in Section 2.2 for the NS equations. The vector of conserved variables from equation (2.2.1) can be evaluated either on the element's center, or on the elements's vertices; the method is said to be cell-centered or node-centered. Conventionally, a typical tetrahedral grid contains from three to six times more number of elements than nodes, resulting in higher spatial resolution for the cell-centered method [84]. This happens also in 2D; the surface triangles edges are twice as much as the number of nodes, predominantly doubling the spatial resolution. The cell-centered technique might be slightly more expensive as it includes computations of barycenters and face-centers, however, it is more straightforward to program and inherits a flexibility, particularly with the implementation of boundary conditions, that the node-center is lacking [85]. Therefore, the cell centered data storage approach is adopted for this work.

3.1.1 Geometric Elements

Three-dimensional unstructured mixed-element grids are composed by four types of elements - convex polyhedrons: the tetrahedral, the hexahedral, the prism and the pyramid (shown in Figure 3.1 on page 16). Each element type is positioned on the spatial domain for a different purpose; the hexahedral and the prism are usually placed for boundary layer cases, in the vicinity of wall boundaries, where local refinement is

required to accurately resolve the boundary layer flow. The main advantage of these two elements lies within the constant orthogonality of the normal to the surface edges. Furthermore, both algebraic and hyperbolic grid generation marching algorithms can be successfully used to generate high quality mesh with low skewness, and small aspect ratios even on complicated geometries with curved surfaces and sharp edges [86]. The tetrahedral is a fundamental geometric element in the sense that it has the least number of faces (four triangular). Moreover, all polyhedrons can be decomposed to tetrahedral and a coordinate transformation for a tetrahedral element is relatively simple compared to the other elements. Finally, the pyramid is usually placed on the interconnecting layer between the hexahedral quadrilateral face and the triangular of the tetrahedral; a detailed geometrical description of the polyhedrons can be found in Table 3.1 on page 16.

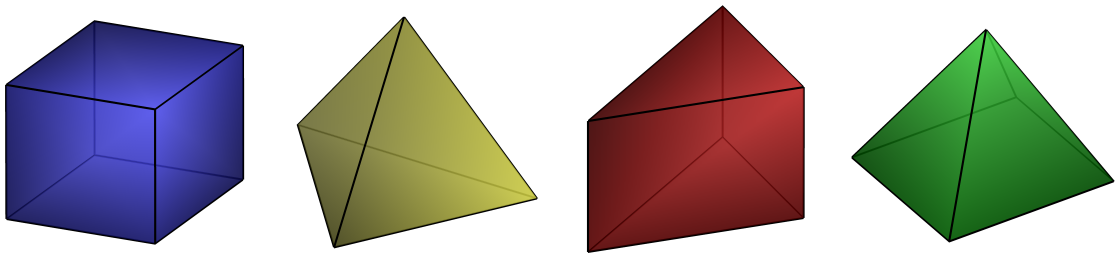

(a) Hexahedral (b) Tetrahedral (c) Prism (d) Pyramid

Figure 3.1: Convex polyhedrons

Table 3.1: Geometrical parameters of convex polyhedrons and decompositions

Geometrical Parameters	Hexahedron	Tetrahedron	Prism	Pyramid
Vertices	8	4	6	5
Triangular Faces	0	4	2	4
Quadrilateral Faces	6	-	3	1
Tetrahedral Decompositions	6	-	3	2
Triangular Decompositions	12	-	8	6

3.1.2 Elements Decompositions

All non-tetrahedral elements including: the hexahedrons, the prisms and pyramids are submitted to a lower-decomposition process, transforming them to several tetrahedral elements. This procedure has many advantages: it minimizes the computational

effort and reduces the geometric calculations from four different equations for the computations of barycenters, face-centers and volumes, to one. The polynomial reconstruction is simplified as its basis functions are expressed independently of the element shape, and the coordinate transformation is accomplished based on decomposed tetrahedrons [87]. Equivalently, each quadrilateral element's face is decomposed into two triangular.

Table 3.1 on page 16 tabulates the low-order decompositions of the polyhedrons to tetrahedrons as well as the decompositions of quadrilateral surfaces to triangles for each element. To maintain a comprehensive thesis the summation notation of the decomposed elements is omitted.

3.1.3 Coordinate Transformation

All elements in the grid are transformed from the physical Cartesian coordinate system (x, y, z) to the reference system (ξ, η, ζ), as first presented by Dumbser and Käser [88] for tetrahedral elements and extended to arbitrary-shaped elements by Tsoutsanis et al. [87]. The coordinate transformation is an unitarian procedure in the sense that it withdraws any undesirable scaling issues from the numerical method. The advantages of the transformation will be emphasized in the following sections when discussing the polynomial basis functions and the high-order WENO reconstruction. The transformation states: an element E is mapped to the reference space as $\tilde{E}$ according to the following equation:

$$\begin{pmatrix} \xi \\ \eta \\ \zeta \end{pmatrix} = \mathrm{J}^{-1} \cdot \begin{pmatrix} x - x_1 \\ y - y_1 \\ z - z_1 \end{pmatrix}, \quad \mathrm{J} = \begin{bmatrix} x_2 - x_1 & x_3 - x_1 & x_4 - x_1 \\ y_2 - y_1 & y_3 - y_1 & y_4 - y_1 \\ z_2 - z_1 & z_3 - z_1 & z_4 - z_1 \end{bmatrix} \tag{3.1.1}$$

where (x_1, y_1, z_1), (x_2, y_2, z_2), (x_3, y_3, z_3) and (x_4, y_4, z_4) are the Cartesian coordinates of the four vertices constituting a tetrahedron, $\mathrm{x} = (x, y, z)$ are the vertex coordinates of the considered polyhedron and J being the Jacobian of the transformation.

For non-tetrahedral elements, the mapping is carried out for one of the decomposed tetrahedrons and according to its transformation the whole polyhedron is mapped to the reference coordinate system, so x is expressed as $\mathrm{x_v} = (x_\mathrm{v}, y_\mathrm{v}, z_\mathrm{v})$ rather than as x,

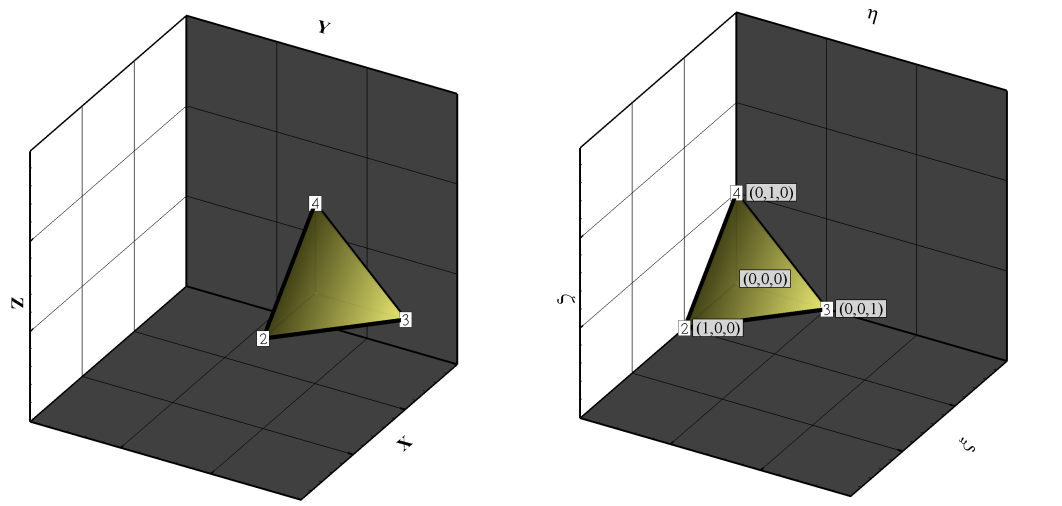

(a) Tetrahedron in Physical Coordinates (x, y, z)

(b) Tetrahedron in Reference Coordinates (ξ, η, ζ)

Figure 3.2: Tetrahedron coordinate transformation

where v is the index of the polyhedron vertices. It is worth noting, that the spatial averages do not change during the mapping procedure and the transformation retains the conservation properties of the equations.

By transforming all the geometric entities of the spatial domain, the coordinates of the gaussian quadrature points can be computed and pre-stored which are required for the evaluation of the fluxes as introduced in section (2.2.2).

3.2 Basic Reconstruction

The cornerstone of the developed numerical method lies within the FV "$k-exact$" framework, originally developed by Barth and Frederickson [89], which is an extension of Godunov's scheme [90]. The method states: *a polynomial is reconstructed where its average is equal to the average of the solution inside the element*. The reconstruction is exact for a polynomial of degree k or lower and assures conservation of the solution averages i.e. conservation of mass, momentum and energy; Van Leer [91], Collela and Woodward [92] extended the method to 2^{nd} and 3^{rd}-order of accuracy, respectively on structured grids.

Since the start of the 1990s, unstructured grid based solvers have reached an unprecedented popularity; ergo the adoption of the method was immediate, several papers where published demonstrating the multidimensional capabilities with the substantial increase of the resolution and accuracy. The method was developed to handle both inviscid and viscous flows with main interest in aeronautical applications [20–22, 84, 89, 93–103].

The basic reconstruction has as an underlying goal to reconstruct a r-degree polynomial $p_i(\xi,\eta,\zeta)$ that will have the same element averages $\overline{q}_i$ as a general property $q_i(\xi,\eta,\zeta)$ within an arbitrary shaped element of volume $|\tilde{V}_i|$ in the reference coordinate space, expressed as

$$\overline{q}_i \equiv \frac{\int_{\tilde{E}_i} p_i(\xi,\eta,\zeta)d\xi d\eta d\zeta}{|\tilde{V}_i|} = \frac{\int_{\tilde{E}_i} q_i(\xi,\eta,\zeta)d\xi d\eta d\zeta}{|\tilde{V}_i|} \tag{3.2.1}$$

note, i stands for the index of the considered element. Concurrently, the polynomial will evaluate point-wise values of $q_i(\xi,\eta,\zeta)$ written as

$$q_i(\xi,\eta,\zeta) = p_i(\xi,\eta,\zeta) + constant \cdot h^r,\ h \approx |V_i|^{1/d} \tag{3.2.2}$$

where d is the spatial dimension 3, the constant represents the constant of integration [84, 93].

3.2.1 Central Stencil Construction

The reconstruction of the r-degree polynomial requires the solution element averages of the considered element, but also the averages of each neighbouring element. Therefore, for each element in the grid, direct-side neighbouring elements are recursively accumulated forming an assembly of elements, the *Von Neumann neighborhood* or simply the stencil $\mathcal{S}$. The number of elements admitted to a stencil is proportional to the polynomial order r according to the equation

$$K = \frac{1}{6}(r+1)(r+2)(r+3) - 1 \tag{3.2.3}$$

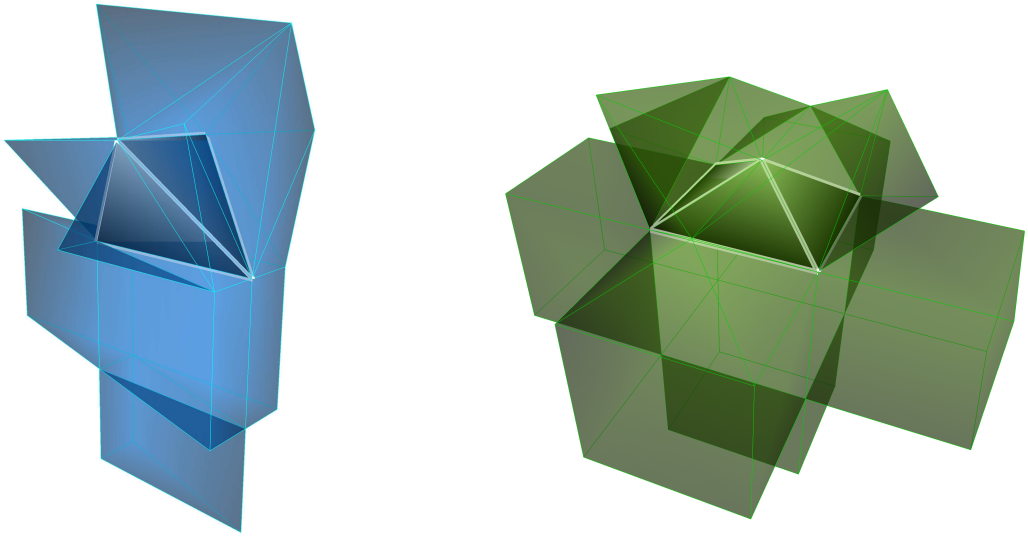

(a) Tetrahedron (b) Pyramid

Figure 3.3: Central stencil for a 3^{rd}-order polynomial reconstruction

where K is the minimum number of elements composing a single stencil. It is recommended to use between 50% to 100% more elements, to improve the robustness of the numerical scheme [104]; a total of $M \approx 2 \cdot K$ are employed for the central reconstruction [88]. The stencil $\mathcal{S}$ is also mapped to the reference coordinate system as

$$\mathcal{S} = \bigcup_{m=0}^{M} E_m \Longrightarrow \tilde{\mathcal{S}} = \bigcup_{m=0}^{M} \tilde{E}_m \tag{3.2.4}$$

The stencil is formed with a recursive algorithm which starts by adding the direct-side neighbours of the considered element, then adds the neighbours of the neighbours until the predetermined total number is reached. The stencils are constructed independently of the element's shape, Figure 3.3 on page 20 shows two mixed-elements stencils for a 3^{rd}-order accurate scheme, the considered elements for which the stencil is constructed is shown with white lines.

3.2.2 Polynomial Expansion

All admissible elements of the constructed stencil are transformed from the physical to the reference space according to the considered element. The reconstruction polynomial $p(\xi, \eta, \zeta)$ is expressed for the whole stencil rather for the considered element

and is sought as an expansion over local polynomial basis functions $\phi(\xi, \eta, \zeta)$ as

$$p(\xi, \eta, \zeta) = \overline{q}_i + \sum_{k=1}^{K} a_k \phi_k(\xi, \eta, \zeta) \tag{3.2.5}$$

where k is the index of the summation of the degrees of freedom (DOF) or solution unknowns a_k, note that k starts from 1, as 0 stands for the average of the solution for the considered element $\overline{q}_i$. The reconstruction polynomial $p(\xi, \eta, \zeta)$ is expressed in terms of its basis function where the basis function are found as

$$\phi(\xi, \eta, \zeta) = \sum_{\alpha=0}^{r} \sum_{\beta=0}^{r-\alpha} \mathcal{P}^{\alpha}(\xi)\, \mathcal{P}^{\beta}(\eta)\, \mathcal{P}^{\gamma}(\zeta) \tag{3.2.6}$$

where $\gamma = r - \alpha - \beta$ and the basis functions with respect to the polynomials $\mathcal{P}$ of degree M from equation (3.2.3). The basis functions are high-order and hierarchical, meaning that each lower-order set of functions is a subset of all high-order sets. This basic characteristic allows various orders of approximation over arbitrary shapes providing the required flexibility for unstructured grids. The basis functions are orthogonal providing stability and overall accuracy of the numerical method by maintaining a low condition number.

The orthogonal Legendre type basis are employed, and to preserve positivity, the regular singular points are shifted from $[-1, 1]$ to $[0, 1]$. The first four shifted polynomials $\mathcal{P}_r$ for ξ are given as

Table 3.2: Shifted Legendre type polynomial basis

r	$\mathcal{P}_n(\xi)$
0	1
1	$2\xi - 1$
2	$6\xi^2 - 6\xi + 1$
3	$20\xi^3 - 30\xi^2 + 12\xi - 1$
4	$70\xi^4 - 140\xi^3 + 90\xi^2 - 20\xi + 1$
⋮	⋮

Expanding the basis functions and substituting back to equation (3.2.5) for the

reconstructed polynomial $p(\xi,\eta,\zeta)$ yields

$$
\begin{aligned}
p_i(\xi,\eta,\zeta) &= \overline{q}_i + \sum_{k=1}^{K} a_k \phi_k(\xi,\eta,\zeta) \\
&\equiv \overline{q}_i + \sum_{k=1}^{K} a_k \left[\psi_k(\xi,\eta,\zeta) - \frac{\int_{\tilde{E}_i} \psi_k \, d\xi d\eta d\zeta}{|\tilde{V}_i|} \right], \quad k = 1, 2, \dots K \\
&\text{where} \quad \psi_k = -1 + 2\xi, -1 + 2\eta, -1 + 2\zeta, 1 - 6\xi + 6\xi^2, (-1 + 2\xi)(-1 + 2\eta), \\
&(-1 + 2\xi)(-1 + 2\zeta), 1 - 6\xi + 6\xi^2 \dots
\end{aligned}
\tag{3.2.7}
$$

The system unknowns a_k are found by substituting the above expression to the conservation conditions (3.2.2) by requiring that the element average of the polynomial $p_m(\xi,\eta,\zeta)$ being equal to the element average of the solutions $\overline{q}_m$, where subscript $m = 1, \dots M$ is the index of the admitted elements to the stencil $\tilde{\mathcal{S}}$, yielding

$$
\overline{q}_m = \overline{q}_i + \frac{1}{|\tilde{V}_m|} \sum_{k=1}^{K} \int_{\tilde{E}_m} a_k \phi_k d\xi d\eta d\zeta = \frac{\int_{\tilde{E}_m} p(\xi,\eta,\zeta) d\xi d\eta d\zeta}{|\tilde{V}_m|} \tag{3.2.8}
$$

As the total number of elements in the stencil (M) is greater than the DOF (a_k), the system (3.2.8) is over-determined and is solved with a least-square method.

3.2.3 Least-Square Method

Least-square methods have been widely employed for the reconstruction of the solution and the gradient in the unstructured grid framework, as the inherit flexibility and it is consistent with mixed-element grids [104–107]. In detail, the over-determined system (3.2.8) can be written in matrix form by assigning the integral of the basis functions for a stencil element as $\mathrm{A}_{(m,k)}$ and b_m the difference between the average of the stencil element with the considered element written as

$$
\mathrm{A}_{(m,k)} = \int_{\tilde{E}_m} \phi_k d\xi d\eta d\zeta, \quad b_m = |\tilde{V}_m|(\overline{q}_m - \overline{q}_i) \tag{3.2.9}
$$

so the (3.2.8) takes the following form

$$\sum_{k=1}^{K} \mathrm{A}_{(m,k)} a_k = b_m, \quad m = 1, 2, \ldots M \tag{3.2.10}$$

The least square solution is obtained by computing the minimum of the squared difference of (3.2.10), yielding

$$\sum_{m=1}^{M} \left\{ \sum_{k=1}^{K} \left(\mathrm{A}_{(m,k)} a_k - b_m \right)^2 \right\} \rightarrow \min \tag{3.2.11}$$

The above minimization procedure results in a linear system of equations and by differentiating with respect to a_p, where $p = 1, \ldots K$ yields

$$\sum_{k=1}^{K} \left\{ \sum_{m=1}^{M} \left(\mathrm{A}_{(m,k)} a_k - b_m \right) \mathrm{A}_{(m,p)} \right\} = 0, \quad p = 1, \ldots K \tag{3.2.12}$$

rearranging the system for a_k the to final form reads

$$\sum_{k=1}^{K} \left\{ \sum_{m=1}^{M} \mathrm{A}_{(m,p)} \mathrm{A}_{(m,k)} \right\} a_k = \sum_{k=1}^{K} \sum_{m=1}^{M} \mathrm{A}_{(m,p)} b_m \tag{3.2.13}$$

For computational efficiency, the symmetric linear matrix $\mathrm{A}_{(m,k)}$ is pre-computed and stored in the computer memory as it is strictly geometric dependent. Nevertheless, the memory required for three-dimensional grids could be relatively high [108]. The mapping procedure (3.1.1) assures numerical stability with respect to geometric characteristics and withdraws any scaling effects, thus inverse weighting techniques are not currently employed. The orthogonal QR decomposition [94] is employed to solve the linear least-square system (3.2.13), it has been reported in the literature that for unstructured grids the system could have a high condition number [104, 109], therefore, the Householder reflection method is used to assure a well-conditioned system, numerical stability and robustness.

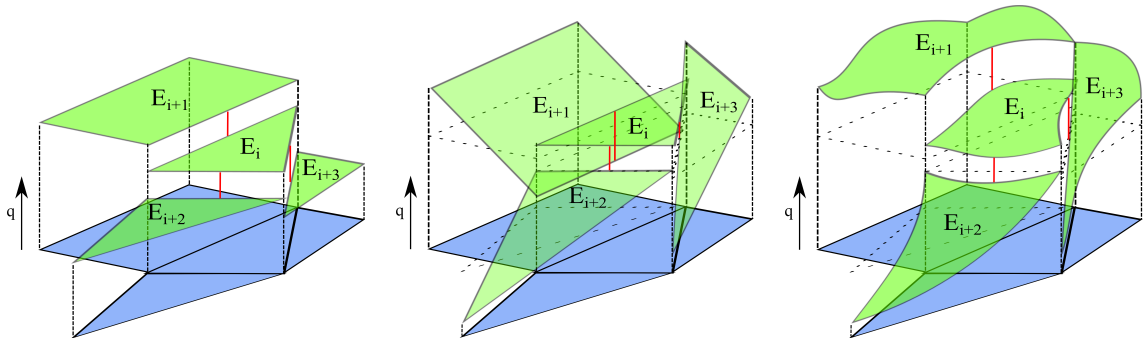

(a) Piecewise constant 1^{st}-order (b) Piecewise linear 2^{nd}-order (c) Piecewise non-linear higher-order

Figure 3.4: Schematics of reconstruction types on 2D mixed-element unstructured grid

3.3 MUSCL-TVD Scheme

Any numerical schemes employed for the solution of hyperbolic conservation laws i.e. Euler equations, has to satisfy the monotonicity criterion: prevent the creation of local extrema. In other words, the numerical flux has to remain increasing monotone or decreasing monotone. In the vicinity of large gradients, high-order linear methods produce unphysical oscillations due to the "Gibbs phenomenon" which can decrease the overall accuracy of the numerical method and even produce negative densities and pressures.

Monotone Upstream-Centered Schemes for Conservation Laws (MUSCL), were first introduced by van Leer [91] and are the first class of high-order schemes that address this unphysical phenomenon. The fundamental concept of the method lies within the employment of reconstructed piecewise linear states (cell-averaged) instead of piecewise constant of Godunov's scheme [90] in conjunction with a Total Variation Diminish (TVD) limiting function; Figure 3.4 on page 24 illustrates this concept for mixed-element unstructured 2D grids.

The elementary requirement of TVD schemes is the preservation of monotonicity: the absolute total variation of the numerical approximation of the solution would not increase with time, no new local extrema may be created; with the main objective being to mitigate Godunov Theorem that states: "*Linear numerical schemes for solving PDEs, having the property of not generating new extrema (monotone scheme) can be at most* 1^{st} *– order accurate*" [110, 111]. Upwind TVD schemes use averages of

the convective fluxes with an artificial dissipation term which depends on the sign of characteristics speeds.

Harten [24] first introduced the notion of "total variation non-increasing" scheme with a 2^{nd}-order accurate scheme by maintaining the robustness of 1^{st}-order of accuracy near discontinuities. Shu and Osher [112] demonstrated the accuracy and performance of TVD schemes, achieving good shock capturing abilities, while, Sweby [113] introduced a technique to examine the behavior of flux limiters and visualize the ratio of forward to backward differences in the solution with the $\psi - R$ diagram. For the sake of monotonicity preservation, various concepts have been borrowed from the structured mesh framework, and efficiently extended and implemented for unstructured grids. The flux difference splitting method has been developed by Fezoul and Stoufflet [100], the MUSCL-type scheme under the finite volume approach first introduced by Barth and Jespersen for unstructured grids [22], applied also to magnetohydrodynamics by Tanaka [114]. Since, the establishment of the method, it became broadly popular amongst the scientific community with various authors having published on TVD schemes for unstructured grids in 3D [96, 115–119]. The robustness of the method is mirrored in the fact that all modern CFD commercial packages are standardly equipped with the MUSCL schemes and TVD limiters e.g. ANSYS-Fluent [81], STAR-CCM+ [120] and OpenFOAM® [121].

A limiting function is applied to the final form of the reconstructed system of equation (3.2.8), the function has the main goal of preventing the creation of new local extrema during the reconstruction process, this yields

$$q_m = \overline{q}_i + \Phi_i \frac{1}{|\tilde{V}_m|} \sum_{k=1}^{K} \int_{\tilde{E}_m} a_k \phi_k \, d\xi d\eta d\zeta, \quad \Phi_i \in [0,1] \tag{3.3.1}$$

where Φ_i is a limiting function, a flux or slope limiter [118]; there are various limiters for FV formulations such as the *van Leer* [91], *superbee* [41], *Barth – Jespersen* [22] and *van Albada* [122] all initially formulated for one-dimensional cases. The Barth-Jespersen limiter is employed as it is compact (two-points) and besides being monotone, is also linearity preserving and can be extended to higher dimensions and arbitrary shaped elements [22].

The first step is to find the minimum and maximum values in the Von Neumann

neighbourhood i.e. $q_i^{min} = \min(q_i, q_l)$ and $q_i^{max} = \max(q_i, q_l)$ where $l = 1, ..L$ is the total neighbours of element i. The gradient ∇q_i is an approximation of the solution gradient inside the element i computed previously during the reconstruction process and it incorporates information from the entire central stencil. The gradient ∇q_i is computed at each integration point on the element i bounded surfaces, this reads

$$q_{i,j,\beta} = q_i^c + \Phi_i \nabla q_i \cdot \mathrm{x}_\beta \tag{3.3.2}$$

where q_i^c is the value for the general quantity at the element centroid and x_β are the coordinates of the quadrature points. The limiter seeks the minimum value of the slope limiter for all the points that satisfy the TVD conditions, written as

$$\Phi_i = \min(\overline{\Phi}_{i,m_1}, \overline{\Phi}_{i,m_2}, ...\overline{\Phi}_{i,M}) \tag{3.3.3}$$

Then, the limiting function is applied, composed by three different states according to the difference of the reconstructed value of the considered element $q_{(i,j,\beta)}$ and each of its neighbours q_l, yielding

$$\overline{\Phi}_{i,j,\beta} = \begin{cases} \min\left(1, \dfrac{q_{i,j,\beta}^{max} - q_{i,j,\beta}}{q_l - q_{i,j,\beta}}\right), & \text{if } q_l - q_{i,j,\beta} > 0 \\ \min\left(1, \dfrac{q_{i,j,\beta}^{min} - q_{i,j,\beta}}{q_l - q_{i,j,\beta}}\right), & \text{if } q_l - q_{i,j,\beta} < 0 \\ 1, & \text{if } q_l - q_{i,j,\beta} = 0 \end{cases} \tag{3.3.4}$$

Despite the fact that the central stencil is engaged for the reconstruction process, the reconstructed values are limited only for the direct-side neighbours; this makes the schemes piecewise linear and the accuracy is at most 2^{nd}-order accurate in space.

3.4 WENO Scheme

Higher than 2^{nd}-order spatial accuracy was achieved with the pioneering work of Harten et al. [33] on Essentially Non-Oscillatory (ENO) schemes for structured grids, where element averages are employed to reconstruct the solution using piecewise polynomials. ENO schemes aim to achieve high-order accuracy in smooth flow regions and to reduce spurious oscillations in the vicinity of strong gradients.

In the past, various authors have implemented ENO schemes into unstructured grid frameworks, including Abgrall's [36] 3^{rd}-order ENO scheme for triangular 2D grids and Liu's et al. [38] ENO reconstruction based on the modification of the "smoothest" stencil selection, with a weighted convex combination method, where all elements of the stencil were considered for the Weighted-ENO (WENO) reconstruction. Furthermore, Jiang and Shu [40] have extensively analysed the robustness of the WENO schemes and extended the order of accuracy to 5^{th}-order for 2D problems. Friedrich [37] demonstrated the WENO schemes superiority in terms of accuracy and stability over ENO schemes on unstructured grids. Balsara and Shu [123] introduced monotonicity preserving bounds to WENO schemes, Hu and Shu [39] implemented WENO schemes on 2D triangular grids and investigated their effectiveness for handling negative linear weights [124].

In three dimensions, Zhang and Shu [125] developed a 3^{rd}-order WENO reconstruction on uniform tetrahedral grids. Dumbser and Käser [88] introduced a hybrid ADER/WENO method up to 6^{th}-order accurate for hyperbolic conservation laws and extended its applicability to the compressible Navier-Stokes equations in [126]. Finally, Tsoutsanis et al. [87, 127, 128] extended the WENO schemes to arbitrary 3D unstructured grids for the Euler equations.

The main characteristic of the WENO schemes is a non-linear combination of polynomials arising from different reconstruction stencils in a solution dependent manner. The approach employed here is a WENO k-exact method similar to the implementation of Tsoutsanis et al. [87] and Dumbser and Käser [88] for mixed-element 2D and 3D unstructured grids.

3.4.1 Directional Stencil Construction

WENO stencils are composed by a central and several "directional" or "sectorial" stencils, uniformly covering all outwards marching directions from the considered element bounded surfaces. The directional stencils are assembled based on predefined geometric sectors as proposed by Titarev et al. [127] for 2D and Tsoutsanis et al. [87] for 3D. For 2D, the geometric sectors are constructed based on two neighboring vertices defining an edge and the barycenter of the element. This procedure is extended to

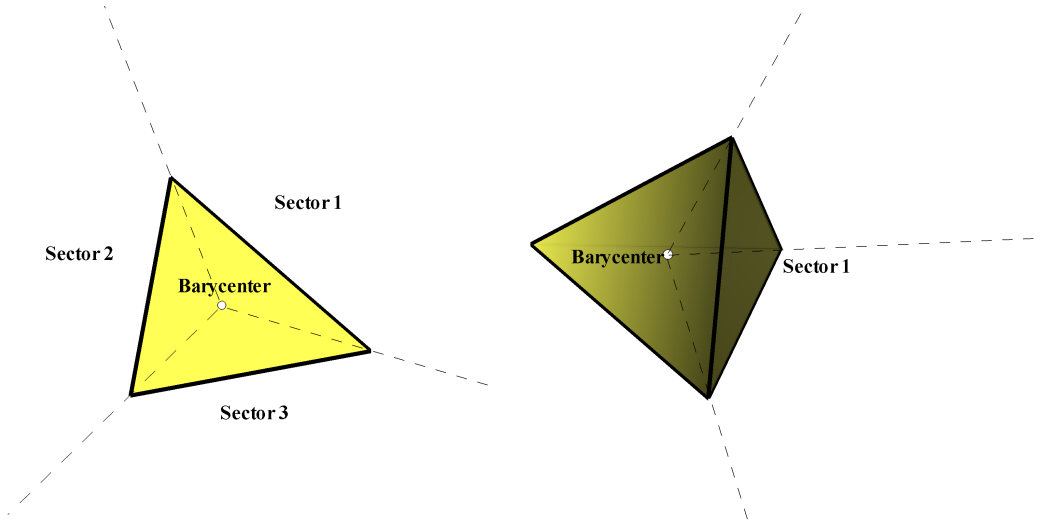

(a) Triangle (b) Tetrahedron

Figure 3.5: Geometric sectors in 2D and 3D

3D, where the vertices form a bounded-surface rather than an edge; Figure 3.5 on page 28 illustrates the sectors for a triangle and a tetrahedron. The main advantage of this method is that it uses half the number of directional stencils, thus it is computationally more efficient compared with methods in [109, 129, 130].

The admissible directional stencils are selected based on the condition that the barycenter of the considered element lies inside a predefined geometrical sector. For elements that are located away from boundaries, the number of directional stencils is usually equal to the number of element's faces $\mathcal{S}_{m_s} = \mathcal{S}_L$.

The directional stencils are constructed by recursively adding direct-side neighbours subjected to the directionality conditions mentioned above. Additionally, another substantial condition is enforced to ensure that no overlapping elements exist in the stencils. In other words, if an element is added to one directional stencil it will not be included in any other one. The latter condition, if satisfied, is labelled as a "strong" directionality enforcement condition; otherwise, it is labelled as "weak". The aspect of distinct element selection improves the robustness of the scheme for flow problems with sharp gradients [131].

Figures 3.6 and 3.7 demonstrate this concept, 3.6 shows 3^{rd} and 5^{th}-order WENO reconstruction stencils for an hexahedral element located on the bottom surface representing a wall, and a pyramidal element coupling the tetrahedral and hexahedral

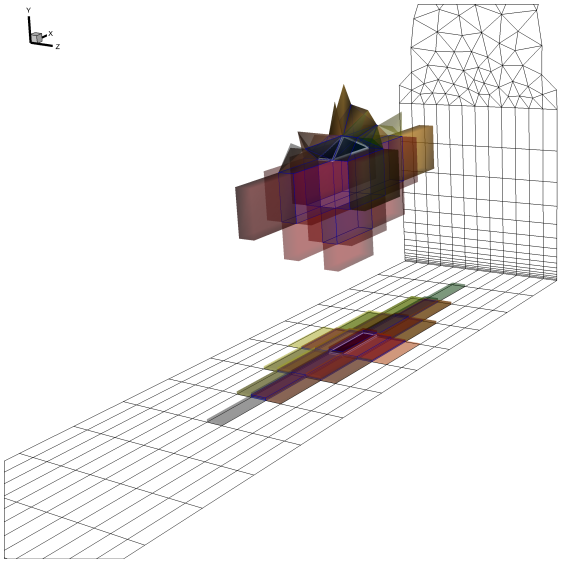

(a) 3^{rd}-order WENO stencils with weak directionality condition

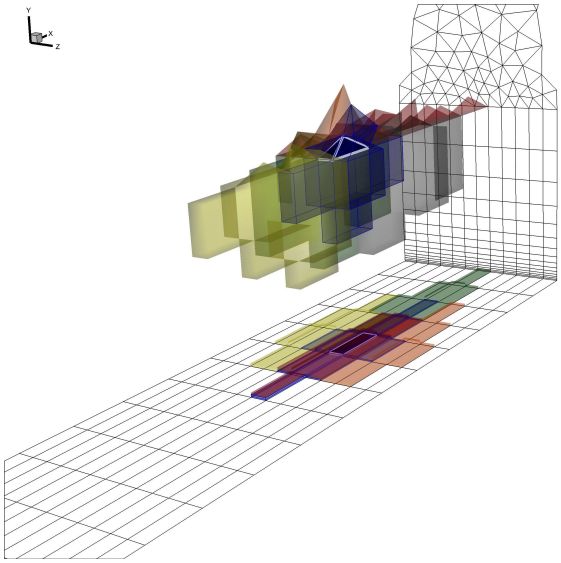

(b) 3^{rd}-order WENO stencils with strong directionality condition

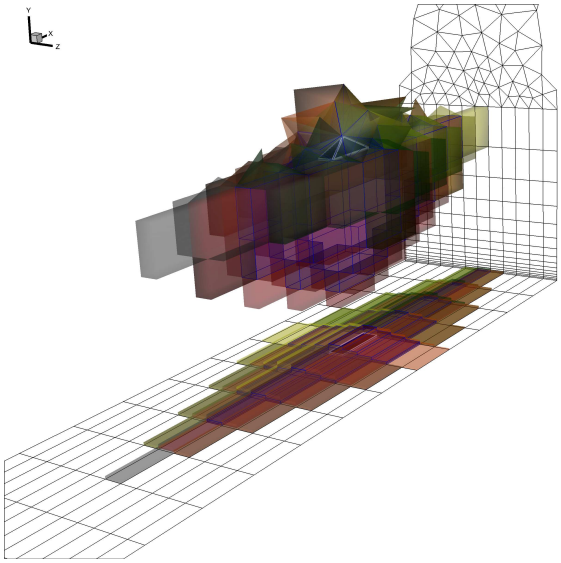

(c) 5^{th}-order WENO stencils with weak directionality condition

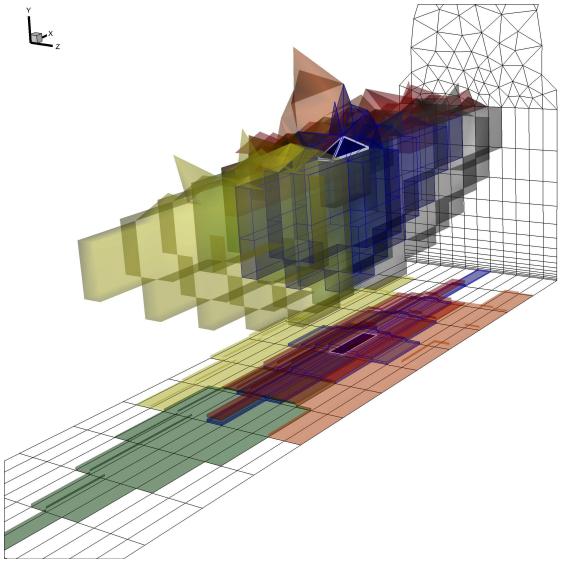

(d) 5^{th}-order WENO stencils with strong directionality condition

Figure 3.6: Central and directional stencils for the hexahedral-pyramid-tetrahedra grid; the considered element is shown with white edge and its central central stencil with blue.

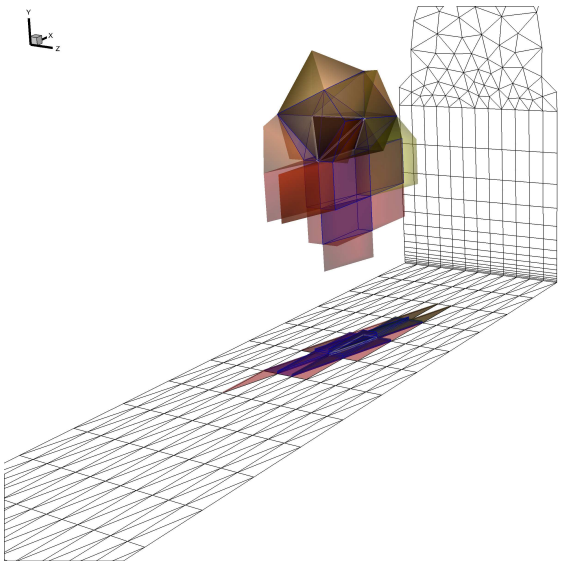

(a) 3^{rd}-order WENO stencils with weak directionality condition

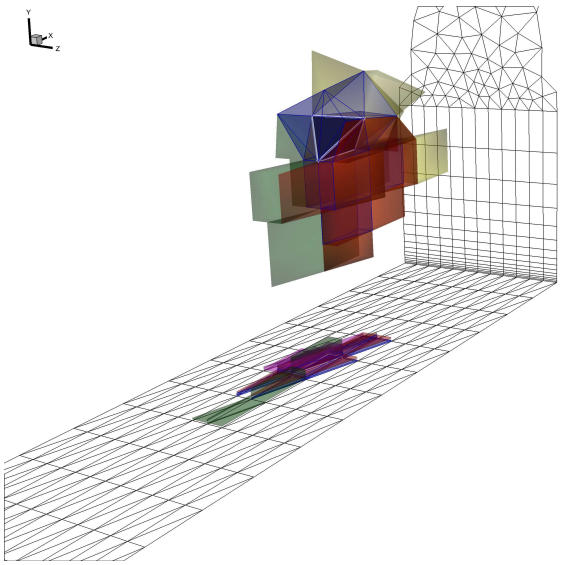

(b) 3^{rd}-order WENO stencils with strong directionality condition

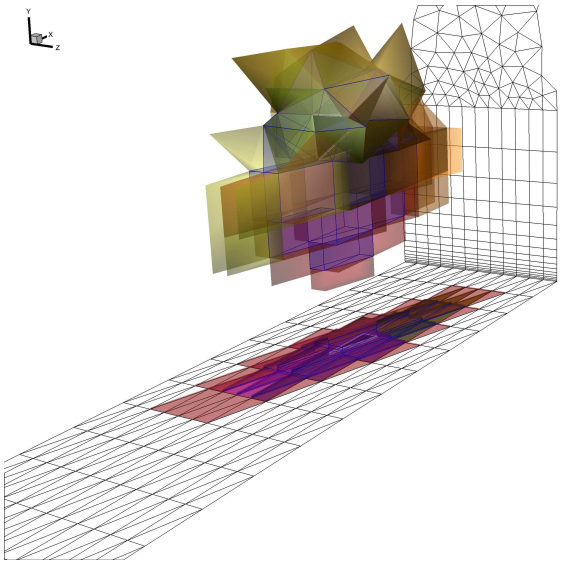

(c) 5^{th}-order WENO stencils with weak directionality condition

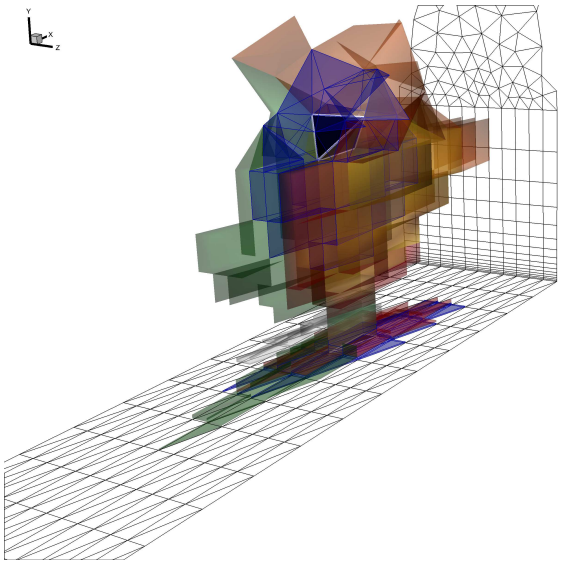

(d) 5^{th}-order WENO stencils with strong directionality condition

Figure 3.7: Central and directional stencils for the prism-tetrahedra grid; the considered element is shown with white edge and its central central stencil with blue.

grid-blocks. The directional stencil are shown with colors, the considered element is shown with white lines and the central stencils with blue lines. The left figures show a directional stencil construction with weak enforcement, the right ones with strong, note that the weak has overlapping elements and cover notably a smaller area than the strong ones. Equivalently, the concept is applied for an tetrahedral and a prismatic element in Figures 3.7.

3.4.2 WENO Formulation

WENO schemes are based on the non-linear solution-adaptive combination of the directional stencils or simply WENO stencils. The WENO stencils are represented in a similar fashion as for the basic reconstruction by high-order polynomials. The non-linearity of the reconstruction is achieved with non-linear weights determined by linear weights in conjunction with the smoothness of the solution for each of the WENO stencils [40, 124, 125]. Consider a reconstruction polynomial $p_m(\xi, \eta, \zeta)$ obtained for each individual stencil $\tilde{\mathcal{S}}_m$ as

$$p_i^{\text{weno}} = \sum_{m=1}^{m_s} \omega_m p_m(\xi, \eta, \zeta) \tag{3.4.1}$$

where m_s is the total number of WENO stencils, substituting back to equation (3.2.7) for $p_m(\xi, \eta, \zeta)$, we obtain the following expression

$$p_m(\xi, \eta, \zeta) = \sum_{m=0}^{K} a_k^{(m)} \phi_k(\xi, \eta, \zeta) \tag{3.4.2}$$

following the condition that the sum of all weights is unity, yields

$$\begin{aligned} p_i^{\text{weno}} &= \overline{q}_i + \sum_{k=1}^{K} \left(\sum_{m=0}^{m_s} \omega_m a_k^m \right) \phi_k(\xi, \eta, \zeta) \\ &\equiv \overline{q}_i + \sum_{k=1}^{K} \tilde{a}_k \phi_k(\xi, \eta, \zeta) \end{aligned} \tag{3.4.3}$$

where $\tilde{a}_k$ is the reconstructed DOF, the non-linear weight is ω_m and is defined as presented in [87, 132], yielding

$$\omega_m = \frac{\tilde{\omega}_m}{\sum_{m=0}^{m_s} \tilde{\omega}_m} \quad \text{where} \quad \tilde{\omega}_m = \frac{\lambda_m}{(\epsilon + \mathcal{I}_m)^b} \tag{3.4.4}$$

where ϵ is a small number to avoid division by zero, $\mathcal{I}_m$ is the smoothness indicators of the solution and b is a integer determining the decay rate of ω_m for steep (non-smooth) stencils, typical values are employed $\epsilon = 10^{-6}$ and $b = 4$ [88]. The linear weights λ_m have been assigned a higher value for the central stencil $\lambda_{\text{central}} \approx 10^3$ and for the directional stencil a value of $\lambda_{\text{WENO}} \approx 1$ [88]. For problems with extreme discontinuities and sharp gradients e.g. supersonic and hypersonic flows, a smaller value for the central stencil linear weight is required $\lambda_{\text{central}} \approx 100$. The solution adaptive character of the schemes is incorporated in the smoothness indicator defined as

$$\mathcal{I}_m = \sum_{1 \leq |\beta| \leq r} \int_{\tilde{E}_i} \left(\mathcal{D}^\beta p_m(\xi, \eta, \zeta) \right)^2 (d\xi, d\eta, d\zeta) \tag{3.4.5}$$

where β is a multi-index, r is the polynomial's order and D is the derivative operator [88]. The grid-dependent parameter usually accounted in the smoothness indicator as presented in [39] is emitted, since the coordinate transformation to the reference system removes any spatial related ambiguities [87]. The smoothness indicator is a quadratic functions of the DOF (a_k^m) and can be expressed as universal mesh-independent oscillation indicator matrix as defined in [132].

WENO reconstruction can be carried out in terms of conserved or characteristic variables. In this work, the WENO reconstruction is carried out in terms of characteristics variables because it enhances the robustness of the schemes as well as makes them more suitable for higher spatial discretisation methods.

3.4.3 Characteristics Based Reconstruction

The characteristic reconstruction utilises the characteristic variables for determining the non-linear weights of the WENO algorithm. To enhance computational efficiency, the characteristic-based reconstruction is employed on the DOF as introduced

by Dumbser et al [132] rather than the element averages. Furthermore, the entire polynomial is reconstructed with the WENO algorithm and the characteristic decomposition is applied for each quadrature point of each face for the considered element. The method differs from [132] as it reconstructs entire polynomials without considering the ENO-type scheme based on the smoothest stencil selection.

In more detail, consider element i with $\vec{n}$ being the unit normal vector on the face j, one of its neighboring elements i_j and the arithmetic average of a general variable q defined as $\overline{q}^{\vec{n}}_{i,i_j} = 1/2(q_i + q_{i_j})$. The hyperbolic conservation law is derived from the system of equations (2.1.1) by excluding the viscous components. The projection of the inviscid flux tensor according to the normal direction computed at the average state $\overline{q}^{\vec{n}}_{i,i_j}$ is written as

$$\mathrm{J}_j = \left.\frac{\partial \vec{F}^{\mathrm{c}}_{\vec{n}}}{\partial q}\right|_{q=\overline{q}^{\vec{n}}_{i,i_j}} \tag{3.4.6}$$

where J_j is the Jacobian matrix with R_j and L_j being the right and left eigenvector matrices respectively, see Appendix-Section 9.1 for the complete formulation of the Jacobian for the Euler's equations. For a stencil $\mathcal{S}$ composed by M elements, the characteristic projections of the DOF (a_k) are computed as

$$\mathrm{B}^m_{i,j,k} = \mathrm{L}_j \mathrm{A}^m_{i,j}, \qquad m = 0, \ldots, M \quad k = 0, \ldots, K \tag{3.4.7}$$

Reconstructing each projected DOF according to the WENO method in Section 3.4.2, the reconstructed DOF $\tilde{\mathrm{B}}^m_{i,j,k}$ are projected back by multiplying with the right eigenvector R_j, then the reconstructed WENO polynomial is written as

$$p^{\mathrm{weno}}_{i,j}(\xi,\eta,\zeta) = \overline{q}_i + \sum_{k=1}^{K} \tilde{\mathrm{A}}^m_{i,j,k}\phi_{i,k}(\xi,\eta,\zeta) \quad \tilde{\mathrm{A}}^m_{i,j,k} = \mathrm{R}_j \mathrm{B}^m_{i,j,k} \tag{3.4.8}$$

where $\phi_{i,k}$ are the polynomial basis functions and $\tilde{\mathrm{A}}^m_{i,j,k}$ are the DOF which are depended also on the considered face j. By extending equation (3.4.8) for each integration point the reconstruction takes the following form

$$p^{\mathrm{weno}}_{i}(\xi_\beta,\eta_\beta,\zeta_\beta) = \overline{q}_i + \sum_{k=1}^{K} \tilde{\mathrm{A}}^m_{i,j,k}\phi_{i,k}(\xi_\beta,\eta_\beta,\zeta_\beta) \tag{3.4.9}$$

where index β corresponds at each point, and to enhance computational performance

the basis functions $\phi_{i,k}(\xi_\beta, \eta_\beta, \zeta_\beta)$ are computed once and stored in the memory. The characteristic based reconstruction is employed on each reconstructed polynomial, thus is more efficient than in [132] where the smoothest stencil is considered.

Furthermore, for flows with excessive discontinuities such as strong shocks and rarefaction waves, WENO schemes might fail in these proximities, and to account for this issue the reconstruction order is dropped to a lower one only for the troubled elements. This is achieved by examining the difference of the cell-centered values, if the difference is severely large, then the order reduction is applied. This technique is adopted from [133] with minor modifications to account for arbitrary unstructured grids. This method increases the robustness of the solver and does not affect the overall order of accuracy of the scheme in the smooth flow regions [133].

3.5 Inviscid Fluxes

Recalling the semi-discrete FV formulation of the NS equations (2.2.1) where the fluxes are evaluated according to the normal vector on the bounded face of element i by integrating over the face area. The integration is achieved by employing a classical multidimensional Gaussian quadrature formula [134, 135]. Rewriting the inviscid fluxes $\vec{F}^c_{i,j}$ of equation (2.2.3)

$$\vec{F}^c_{i,j} = \sum_{j=1}^{L} \sum_{\beta=1}^{B} \vec{F}^c_{\vec{n},j} \left(\bar{W}(\mathrm{x}_\beta, t) \right) \omega_\beta |A_j| \tag{3.5.1}$$

where $\bar{W}(\mathrm{x}_\beta, t)$ is the solution vector at time t, $\vec{F}^c_{\vec{n},j}$ is the projection of the flux tensor on the normal direction, x_β being the Gaussian integration point coordinates, with a total points employed B per face, with its corresponding weight ω_β evaluated over the face surface area $|A_j|$.

For linear reconstruction only one Gaussian quadrature point is required per face, but for higher order reconstruction i.e. 3^{rd} and 5^{th}, a quadrature rule of appropriate order is engaged. It must be stressed, that any quadrature formula that includes negative weights might lead to unstable numerical integration and must be avoided. Table 3.3 on page 35 shows the quadrature points coordinates and weights for a

triangle.

Table 3.3: Gaussian quadrature point coordinates and weights for a triangle

Order	x_ξ	x_η	ω
1^{st}	0.333333333333333	0.333333333333333	1.000000000000000
2^{nd}	0.666666666666667	0.166666666666667	0.333333333333333
	0.166666666666667	0.166666666666667	0.333333333333333
	0.166666666666667	0.666666666666667	0.333333333333333
3^{rd}	0.333333333333333	0.333333333333333	-0.56250000000000
	0.600000000000000	0.200000000000000	0.520833333333333
	0.200000000000000	0.600000000000000	0.520833333333333
	0.200000000000000	0.200000000000000	0.520833333333333
4^{th}	0.816847572980459	0.091576213509771	0.109951743655322
	0.091576213509771	0.816847572980459	0.109951743655322
	0.091576213509771	0.091576213509771	0.109951743655322
	0.108103018168070	0.445948490915965	0.223381589678011
	0.445948490915965	0.108103018168070	0.223381589678011
	0.445948490915965	0.445948490915965	0.223381589678011
5^{th}	0.333333333333333	0.333333333333333	0.225000000000000
	0.797426985353087	0.101286507323456	0.125939180544827
	0.101286507323456	0.797426985353087	0.125939180544827
	0.101286507323456	0.101286507323456	0.125939180544827
	0.059715871789769	0.470142064105115	0.132394152788506
	0.470142064105115	0.059715871789769	0.132394152788506
	0.470142064105115	0.470142064105115	0.132394152788506

Each conserved variable is approximated by piece-wise polynomials, where the solution is continuous throughout the element but discontinuous on the boundary interfaces, as shown in Figure 3.4 on page 24 with red lines. Two approximated values exist for the reconstructed solution at the boundary with respect to the elements sharing a face. $\vec{W}_\beta^-$ is the extrapolated value computed by the polynomial p_i for the considered element and $\vec{W}_\beta^+$ is the extrapolated value of its neighbouring element. For a Godunov upwind scheme the physical normal flux is replaced by a numerical flux, yielding

$$\vec{F}^c_{i,j} = \sum_{j=1}^{L} \sum_{\beta=1}^{B} \hat{F}_{\vec{n},j}(\vec{W}_\beta^-, \vec{W}_\beta^+)\omega_\beta |A_j| \tag{3.5.2}$$

where the projection of the flux tensor to the normal direction $\vec{F}^c_{\vec{n},j}$ from equation (3.5.1) is replaced by $\hat{F}_{\vec{n},j}$ which is a function, a building block of a high-order scheme also known as a Riemann solver [90]. For each bounded surface, the projected flux

tensor $\hat{\mathrm{F}}_{\vec{n},j}$ is rotated according to a constant rotational matrix T following the rotational invariance concept [136], yielding

$$\hat{\mathrm{F}}_{\vec{n},j} = \mathrm{T}^{-1}\vec{F}(\mathrm{T}_j\vec{W}_\beta) \tag{3.5.3}$$

where the rotational matrix T is given by

$$\mathrm{T} = \begin{bmatrix} 1 & 0 & 0 & 0 & 0 \\ 0 & \cos\theta\sin\varphi & \sin\theta\sin\varphi & \cos\varphi & 0 \\ 0 & -\sin\theta & \cos\theta & 0 & 0 \\ 0 & \cos\theta\cos\varphi & \sin\theta\cos\varphi & -\sin\varphi & 0 \\ 0 & 0 & 0 & 0 & 1 \end{bmatrix} \tag{3.5.4}$$

where θ is the azimuthal angle and φ is the polar angle [137]. By substituting back to equation (3.5.2) the following expression reads

$$\vec{F}^{\mathrm{c}}_{i,j} = \sum_{j=1}^{L}\sum_{\beta=1}^{B} \mathrm{T}^{-1}\vec{F}\left(\hat{W}^{-}_{\beta}, \hat{W}^{+}_{\beta}\right)\omega_\beta|A_j| \tag{3.5.5}$$

where $\hat{W}^{-}_{\beta}$ and $\hat{W}^{-}_{\beta}$ are the rotated conserved variable vectors given by

$$\hat{W}^{-}_{\beta} = \mathrm{T}_j\vec{W}^{-}_{\beta} \quad \hat{W}^{+}_{\beta} = \mathrm{T}_j\vec{W}^{+}_{\beta} \tag{3.5.6}$$

For each quadrature point (β) the monotone flux function $\hat{\mathrm{F}}_{\vec{n},j}$ is calculated according to the one 1D Riemann problem written as

$$\frac{\partial}{\partial t}\hat{W} + \frac{\partial}{\partial s}\hat{F} = 0, \quad \hat{F} = \vec{F}\left(\hat{W}\right), \quad \hat{W}(s,0) = \begin{cases} \hat{W}^{-}_{\beta}, s < 0 \\ \hat{W}^{+}_{\beta}, s > 0 \end{cases} \tag{3.5.7}$$

The Harten-Lax-van Leer-Contact (HLLC) [136, 138] solver is employed, resolving a three-wave structure where the wave S^-, S^* and S^+ are estimated as follows

$$\hat{\mathrm{F}}^{\mathbf{HLLC}} \begin{cases} \hat{F}^{-}, & \text{if } 0 \le S^{-}, \\ \hat{F}^{*-} = \hat{F}^{-} + S^{-}\left(\hat{W}^{*-} - \hat{W}^{-}\right), & \text{if } S^{-} \le 0 \le S^{*}, \\ \hat{F}^{*+} = \hat{F}^{+} + S^{+}\left(\hat{W}^{*+} - \hat{W}^{+}\right), & \text{if } S^{*} \le 0 \le S^{+}, \\ \hat{F}^{+}, & \text{if } 0 \ge S^{+}, \end{cases} \tag{3.5.8}$$

where

$$\hat{W}^{*\pm} = \rho^{\pm}\left(\frac{S^{\pm}-u^{\pm}}{S^{\pm}-S^{*}}\right)\begin{bmatrix} 1 \\ S^{*} \\ v^{\pm} \\ w^{\pm} \\ \frac{E^{\pm}}{\rho^{\pm}}(S^{*}-u^{\pm})\left(S^{*}+\frac{p^{\pm}}{\rho^{\pm}(S^{\pm}-u^{\pm})}\right) \end{bmatrix} \tag{3.5.9}$$

$\hat{W}^{*\pm}$ is computed either for the considered element "$-$", or for its neighbour "$+$" and the wave speeds are estimated according to the sign. The HLLC flux incorporates all possible waves in the Riemann problem solution without employing any linearisation of the equations and it has been proven to work well for transonic problems without any modifications [133].

3.6 Viscous Fluxes

Currently, the treatment of viscous gradient and fluxes for mixed-element unstructured grids in 2D and specifically in 3D is a topic of continuous research. Diskin et al [85] demonstrated the superiority of cell-centered based data storage over cell-vertex based data for evaluating the gradient on mixed-element grids, provided a grid independence during the flow simulation. Sharov and Nakahashi [139] introduced edge-based data structure, which is an accurate and efficient way to evaluate the gradient on the nodes at each midpoint edge, Frink [93] presented a method where face-centers approximation were employed for a tetrahedral face where the averaging from the nodes to the face-centers is achieved by a midpoint trapezoidal rule. Haselbacher et al [140] proposed a modified averaging procedure for the evaluation of the gradient where a directional derivative based on the edge's length is introduced.

Edge-based methods will produce accurate gradient approximations but they have difficulties in handling non-uniform grids, therefore, inverse-weighting is necessary to maintain numerical stability. The outcome is complicated and expensive schemes both in terms of memory and computationally cost. Gassner et al [141, 142] derived a generalized diffusive Riemann solver for the treatment of the viscous fluxes, although the computed solutions have reached convergence of the order of the reconstruction, the extension to advection-diffusion problems remains at large.

The calculation of the viscous fluxes requires the computation of the spatial derivatives of the cartesian velocities and temperature at the element's faces for each quadrature point. The method employed for the viscous discretisation is compact, as only the central stencil is employed for the evaluations of the gradients, regardless of the scheme's order. The viscous fluxes $\vec{F}^{\mathrm{v}}_{i,j}$ from equation (2.1.6) are expressed for a Gaussian integration point β, on the considered element's face j written as

$$\vec{F}^{\mathrm{v}}_{i,j} \approx \sum_{j=1}^{L} \sum_{\beta=1}^{B} \vec{F}^{\mathrm{v}}_{\vec{n},j} \omega_\beta |A_j| \tag{3.6.1}$$

where the interface viscous flux, $\vec{F}^{\mathrm{v}}_{\vec{n},j}$ is composed by the normal and shear stresses including the heat fluxes in (2.1.6) which are computed by averaging the boundary extrapolated values from the considered element and its neighbour given by

$$\begin{aligned} &\overline{u}_\beta = \frac{1}{2}\left(u^+_\beta + u^-_\beta\right),\ \overline{v}_\beta = \frac{1}{2}\left(v^+_\beta + v^-_\beta\right),\ \overline{w}_\beta = \frac{1}{2}\left(w^+_\beta + w^-_\beta\right), \\ &\overline{\mu}_\beta = \frac{1}{2}\left(\mu^+_\beta + \mu^-_\beta\right) \end{aligned} \tag{3.6.2}$$

where u, v, w are the velocities components and μ_l is the laminar viscosity (Southerland) required for the evaluation of the viscous stresses and heat fluxes.

3.6.1 Gradient Reconstruction

The velocity and the temperature gradients at the interface are also computed by averaging the boundary extrapolated gradients as

$$\overline{(\nabla \mathcal{U})}_\beta = \frac{1}{2}\left(\nabla \mathcal{U}^-_\beta + \nabla \mathcal{U}^+_\beta\right),\ \overline{(\nabla T)}_\beta = \frac{1}{2}\left(\nabla T^-_\beta + \nabla T^+_\beta\right) \tag{3.6.3}$$

where the velocity gradient components are labeled as $\nabla \mathcal{U} : (u \vee v \vee w)$ and the temperature gradient being ∇T. The gradient is reconstruction according to the central reconstruction detailed in Section 3.2, where the spatial derivatives are transformed from the physical to the reference coordinate space by employing the inverse Jacobian

of the transformation in (3.1.1), yielding

$$\begin{pmatrix} \frac{\partial q}{\partial x} \\ \frac{\partial q}{\partial y} \\ \frac{\partial q}{\partial z} \end{pmatrix}_i^j = \left(\mathrm{J}^{-1}\right)_i^{\mathrm{T}} \begin{pmatrix} \frac{\partial p(\xi,\eta,\zeta)}{\partial \xi} \\ \frac{\partial p(\xi,\eta,\zeta)}{\partial \eta} \\ \frac{\partial p(\xi,\eta,\zeta)}{\partial \zeta} \end{pmatrix}_i^j \tag{3.6.4}$$

where $\left(\mathrm{J}^{-1}\right)_i^{\mathrm{T}}$ is the transpose of the inverse Jacobian for a considered variable q, so the velocity and temperature gradients read

$$(\nabla \mathcal{U}_k) = (\mathrm{J}^{-1})^{\mathrm{T}} \begin{pmatrix} \frac{\partial \mathcal{U}_k}{\partial \xi} \\ \frac{\partial \mathcal{U}_k}{\partial \eta} \\ \frac{\partial \mathcal{U}_k}{\partial \zeta} \end{pmatrix}_k^i, \quad (\nabla T_k) = (\mathrm{J}^{-1})^{\mathrm{T}} \begin{pmatrix} \frac{\partial T_k}{\partial \xi} \\ \frac{\partial T_k}{\partial \eta} \\ \frac{\partial T_k}{\partial \zeta} \end{pmatrix}_k^i \tag{3.6.5}$$

In more details, denote the components of the transpose inverse Jacobian matrix as

$$\left(\mathrm{J}^{-1}\right) = \begin{pmatrix} b_{11} & b_{12} & b_{13} \\ b_{21} & b_{22} & b_{23} \\ b_{31} & b_{32} & b_{33} \end{pmatrix} \tag{3.6.6}$$

then the gradient and its derivatives for a property q takes the following form

$$(\vec{n}, \nabla q_k) = \left(n_x, n_y, n_z\right) \begin{pmatrix} b_{11} & b_{12} & b_{13} \\ b_{21} & b_{22} & b_{23} \\ b_{31} & b_{32} & b_{33} \end{pmatrix} \begin{pmatrix} \frac{\partial q_k}{\partial \xi} \\ \frac{\partial q_k}{\partial \eta} \\ \frac{\partial q_k}{\partial \zeta} \end{pmatrix} = (c_1, c_2, c_3) \times \begin{pmatrix} \frac{\partial q_k}{\partial \xi} \\ \frac{\partial q_k}{\partial \eta} \\ \frac{\partial q_k}{\partial \zeta} \end{pmatrix} \tag{3.6.7}$$

where c_1, c_2 and c_3 are given by

$$\begin{aligned} c_1 &= n_x b_{11} + n_y b_{21} + n_z b_{31} \\ c_2 &= n_x b_{12} + n_y b_{22} + n_z b_{32} \\ c_3 &= n_x b_{13} + n_y b_{23} + n_z b_{33} \end{aligned} \tag{3.6.8}$$

The least square reconstruction of the velocity and temperature gradients for wall-bounded elements is conceived with a special treatment in order to avoid even-

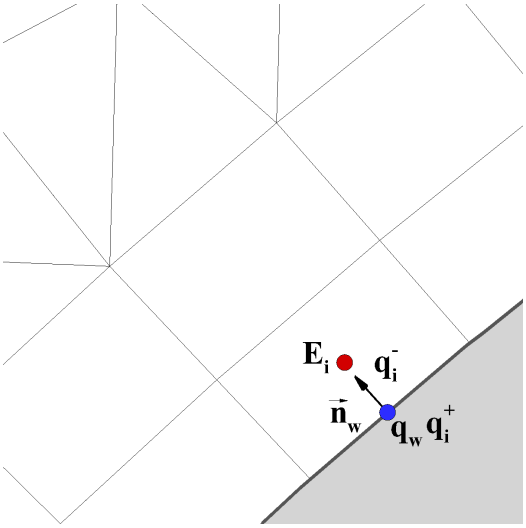

Figure 3.8: Wall boundary

decoupling and ill-conditioned matrices. This numerical treatment is discussed in the following sections.

3.7 Implementation of Boundary Conditions

In any numerical simulation, the spatially discretised domain requires boundary conditions to close the system by prescribing meaningful values for the physical quantities. The selection and implementation of the boundary conditions requires attention, as it affects the overall stability and convergence of the simulation. In contrast to the structured grid framework, where fictitious or ghost cells are employed for the approximation of the physical quantities at the boundary interface [143], their implementation on unstructured grids becomes highly complicated in terms of grid generation and overlapping elements. Therefore, the treatment and implementation of the boundary conditions is conceived in a different, characteristic-wise, adaptive approach, explained in the following subsections.

3.7.1 Adiabatic No-Slip Wall

Solid-wall is the most widely employed boundary condition for engineering applications. In the vicinity of the wall, viscous terms become dominant as the shear forces increase substantially. The relative velocity of the fluid on the wall surface is zero thus, for a non-moving wall, the cartesian velocities at the surface are $u = v = w = 0$. An adiabatic wall is considered so there is no heat transfer between the fluid and the boundary $\vec{n}|_w \nabla T = 0$. As a result the convective fluxes from equation (3.5.1) reduce to the pressure term, the viscous fluxes from equation (2.1.7) take the following form

$$\mathrm{V}_x|_w = \begin{bmatrix} 0 \\ \tau_{xx} \\ \tau_{xy} \\ \tau_{xz} \\ q_x \end{bmatrix}, \mathrm{V}_y|_w = \begin{bmatrix} 0 \\ \tau_{yx} \\ \tau_{yy} \\ \tau_{yz} \\ q_y \end{bmatrix}, \mathrm{V}_z|_w = \begin{bmatrix} 0 \\ \tau_{zx} \\ \tau_{zy} \\ \tau_{zz} \\ q_z \end{bmatrix} \tag{3.7.1}$$

The numerical flux at the boundaries is computed with the inverse Riemann problem [132] by assigning an extrapolated value outside the domain for each conserved variable in order to obtain the correct numerical flux at the interface for the Riemann problem therefore obtain the physical conditions on the boundary. The schematic representation of the concept is shown in Figure 3.8 on page 40 for 2D, where the boundary extrapolated values for outside q_i^+ and for the considered element q_i^- are rotated normal to the boundary surface (line). The conditions for the conserved variables and the gradients on the wall boundary are imposed as

$$\begin{gathered} \rho^+ = \rho^-,\ E^+ = E^-,\ \nabla \mathcal{U}^- = \nabla \mathcal{U}^+ \\ u^+ = -u^-,\ v^+ = -v^-,\ w^+ = -w^-, \nabla \hat{T}^- = -\nabla \hat{T}^+ \end{gathered} \tag{3.7.2}$$

where u, v, w are the cartesian velocity components, ρ and E being the density and total energy respectively, the velocity gradient is written as $\nabla \mathcal{U}$ and $\nabla \hat{T}$ is the temperature gradient rotated according to the normal vector $\vec{n}_w$.

The no-slip wall boundary conditions require a selective reconstruction of the solution in order to maintain accuracy and to avoid an ill-conditioned system. This is achieved by reconstructing the system of equation for the velocity and the temperature terms individually.

No-slip boundary condition for velocity

During the pre-processing stage, the average basis functions of the polynomial are pre-stored for a wall-bounded element, taking also into consideration their weights on the face adjacent to the wall. Applying the non-slip conditions for the considered face, we obtain the least-square system for the velocity components according to the Dirichlet condition as

$$\overline{q}_i + \sum_{k=1}^{K} a_k \phi_k(x|_w) = 0 \tag{3.7.3}$$

where the reference co-ordinates of the face-center adjacent to the wall are $x|_w = (\xi_w, \eta_w, \zeta_w)$. Assuming that the basis function on the wall can not take zero values $\phi_1(x|_w) \neq 0$, the first degree of freedom a_1 is eliminated yielding the following expression

$$a_1 = -\frac{1}{\phi_1(x|_w)} \left\{ \overline{q}_i + \sum_{k=1}^{K} a_k \phi_k(x|_w) \right\} \tag{3.7.4}$$

Substituting back to expression (3.2.8), yields

$$\sum_{k=2}^{K} \left\{ \mathrm{A}_{mk} - \frac{\mathrm{A}_{m1}\phi_k(x|_w)}{\phi_1(x|_w)} \right\} a_k = b_m + \frac{\mathrm{A}_{m1}}{\phi_1(x|_w)} q_i \quad m = 1, \ldots M \tag{3.7.5}$$

note, k starts from the value 2 as a_1 was eliminated, for all elements M in the stencil; the new system can be rewritten as

$$\sum_{k=2}^{K} \tilde{\mathrm{A}}_{mk} a_k = \tilde{b}_m, \quad \tilde{\mathrm{A}}_{mk} = \mathrm{A}_{mk} - \frac{\mathrm{A}_{m1}\phi_k(x|_w)}{\phi_1(x|_w)}, \quad \tilde{b}_m = b_m + \frac{\mathrm{A}_{m1}}{\phi_1(x|_w)} u_i \tag{3.7.6}$$

Adiabatic boundary condition for temperature

The adiabatic condition for the temperature is treated equivalently to the approach utilized for the velocity. The temperature gradient ∇T at adiabatic boundaries follows the Neumann boundary condition written as

$$\vec{n}|_w \nabla T = n_x \frac{\partial T}{\partial x} + n_y \frac{\partial T}{\partial y} + n_z \frac{\partial T}{\partial z} = 0 \tag{3.7.7}$$

where $\vec{n}|_w = (n_x, n_y, n_z)$ is the normal vector at the wall. The above condition is applied

to the least square system (3.2.8) yielding

$$\sum_{k=1}^{K} a_k(\vec{n}, \nabla\phi_k)|_w = \sum_{k=1}^{K} a_k \left\{ n_x \frac{\partial \phi_k}{\partial x} + n_y \frac{\partial \phi_k}{\partial y} + n_z \frac{\partial \phi_k}{\partial z} \right\} = 0 \tag{3.7.8}$$

by substituting for the temperature gradient to the equation (3.6.7) with the corresponding derivatives constants from (3.6.8), the conditions is rewritten as

$$\sum_{k=1}^{K} a_k \varphi_k (x|_w) = 0 \tag{3.7.9}$$

where

$$\varphi_k = c_1 \frac{\partial \phi_k (x|_w)}{\partial \xi} + c_2 \frac{\partial \phi_k (x|_w)}{\partial \eta} + c_3 \frac{\partial \phi_k (x|_w)}{\partial \zeta} \tag{3.7.10}$$

in similar fashion as for the velocities, a_1 is eliminated assuming that $\varphi_1(x|_w) \neq 0$, yields

$$\sum_{k=1}^{K} \varphi_k|_w = 0 \quad \Rightarrow \quad a_1 = -\frac{1}{\varphi_1(x|_w)} \left\{ \sum_{k=2}^{K} a_k \varphi_k(x|_w) \right\} \tag{3.7.11}$$

substituting back to (3.2.8), the final system is obtained

$$\sum_{k=2}^{K} \tilde{\mathrm{A}}_{mk} a_k = b_m, \quad \tilde{\mathrm{A}}_{mk} = \mathrm{A}_{mk} - \frac{\mathrm{A}_{m1} \varphi_k(x|_w)}{\varphi_1 x|_w} \tag{3.7.12}$$

Since high-order numerical integration by a Gaussian quadrature rule will generate several integration points per face or edge, it is highly possible that the number of points will exceed the DOF for wall-bounded elements, over-constraining the least square matrix and decreasing the robustness of the scheme [104]. Thereafter, the least square system with conditions (3.7.6) for the velocity and (3.7.12) for the temperature is only constrain at one point, located at the center of the considered wall-bounded face or edge.

3.7.2 Inflow and Outflow

Flows past aerofoils and wings are considered as external flows where the far field boundary conditions are imposed with free-stream values. For external flows the far

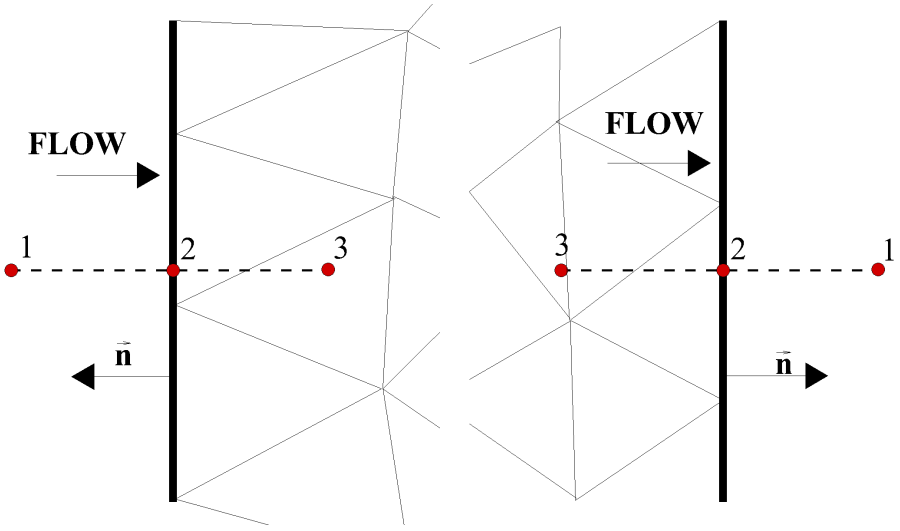

(a) Inflow (b) Outflow

Figure 3.9: Schematics of characteristic inflow and outflow boundary conditions

field has to be placed very far from the body to correspond to an infinite domain. This is a necessary requirement for subsonic and transonic viscous flows as it affects the vortex formation and therefore the lift and drag predictions on the body. For transonic cases, where the local speed is in the regions of the characteristic (speed of sound), the elliptic equations become quite sensitive to the implementation of the far field boundary conditions and phenomena as backwards reflections are often encountered.

To avoid unphysical reflections, characteristic variables are used where the sign of the eigenvalues of the convective flux Jacobian (3.4.6) is utilized as a switch for engaging either subsonic or supersonic condition [144]. The local speed of sound and Mach number are computed and the values at the boundary interface are updated accordingly. The following four boundary conditions are considered

- subsonic inflow
- subsonic outflow
- supersonic inflow
- supersonic outflow

For subsonic inflow conditions, where from the total five characteristics, four enter the

domain and their values are assigned according to the free-stream conditions, the one that leaves is linearly extrapolated from the interior [137]. Figure 3.9 on page 44 (a) shows the three points employed for the estimation of the subsonic inflow conditions: 1 represents the free-stream values, 2 the values at the boundary interface and 3 the extrapolated values from the interior, computed as

$$\begin{aligned}
p_2 &= \frac{1}{2}\left[(p_1 + p_3 - \rho_3 a_3)\left(n_x(u_1 - u_3) + n_y(v_1 - v_3) + n_z(w_1 - w_3)\right)\right] \\
\rho_2 &= \rho_1 + \frac{p_2 - p_1}{a_3^2} \\
u_2 &= u_1 - n_x \frac{p_1 - p_2}{\rho_3 a_3} \\
v_2 &= v_1 - n_y \frac{p_1 - p_2}{\rho_3 a_3} \\
w_2 &= w_1 - n_z \frac{p_1 - p_2}{\rho_3 a_3}
\end{aligned} \tag{3.7.13}$$

where a_3 is the speed of sound in the interior of the domain. For subsonic outflow the pressure is specified usually as the free-stream static pressure as shown in Figure 3.9 on page 44 (b), then the speed of sound is computed and the remaining primitive variables are extrapolated from the interior of the domain, the values at the boundary are computed as follows

$$\begin{aligned}
p_2 &= p_1 \\
\rho_2 &= \rho_3 + \frac{p_2 - p_3}{a_1^2} \\
u_2 &= u_3 - n_x \frac{p_3 - p_2}{\rho_1 a_1} \\
v_2 &= v_3 - n_y \frac{p_3 - p_2}{\rho_1 a_1} \\
w_2 &= w_3 - n_z \frac{p_3 - p_2}{\rho_1 a_1}.
\end{aligned} \tag{3.7.14}$$

Supersonic conditions are less sensitive as all eigenvalues have the same sign, therefore for supersonic inflow all primitive variables are determined by the free-stream values, written as

$$\rho_2 = \rho_1, \quad u_2 = u_1, \quad v_2 = v_1, \quad w_2 = w_1, \quad p_2 = p_1 \tag{3.7.15}$$

and for supersonic outflow the values at the boundary are set by the interior of the domain yielding

$$\rho_2 = \rho_3, \quad u_2 = u_3, \quad v_2 = v_3, \quad w_2 = w_3, \quad p_2 = p_3. \tag{3.7.16}$$

Independent of the spatial order, the accuracy will drop at the boundary as only one state is considered for evaluating the flux.

3.7.3 Symmetric and Periodic

Symmetric and periodic boundary conditions are widely employed in engineering application as well as in fundamental flows as they simplify the problem by reducing the spatial domain and therefore the computational effort. For flows over wings, aircrafts and automobiles, where the body is symmetrical in the span-wise direction, only half of it is modeled and simulated. Assuming that the span-wise values have insignificant variations, then a symmetry plane is applied at the middle cross-section. On this plane the following conditions have to be imposed: no flux through the boundary, thus the normal velocity is zero, the gradient of a scalar quantity is zero. Furthermore, the gradient normal to the boundary of the tangential velocity and the gradient along the boundary of the normal velocity is also zeroed out. Assuming that the symmetry plane is tangential to the z axis, the conditions are written as

$$\begin{aligned} &\vec{n}(u, v, w) = 0 \\ &\frac{\partial T}{\partial z} = 0 \\ &\frac{\partial u}{\partial z} = \frac{\partial v}{\partial z} = 0 \\ &\frac{\partial w}{\partial x} = \frac{\partial w}{\partial y} = 0. \end{aligned} \tag{3.7.17}$$

For certain cases the flow can be considered as periodic in its behavior with respect to one or several directions. The elements with a periodic boundary are explicitly combined with their translational mirrored elements and all conserved variables are directly obtained. Elements with periodic boundaries are considered during the stencil construction phase by satisfying all appropriate conditions, and the coordinates of all

stencil's elements are shifted to match the ones of the considered element.

3.8 Time Discretisation

Having completed the numerical framework related to the spatial domain, and by setting appropriate initial conditions, the solution is advanced in time. The time dependent terms are discretised with the 3^{rd}-order TVD Runge-Kutta method [35], where the average vector of conserved variables $\overline{W}_i$ is advanced in time as follows

$$\begin{aligned}
\overline{W}_i^{n+1/3} &= \overline{W}_i^n + \Delta t \cdot \mathrm{RHS} \cdot \overline{W}_i^n, \\
\overline{W}_i^{n+2/3} &= \frac{3}{4}\overline{W}_i^n + \frac{1}{4}\overline{W}_i^{n+1/3} + \frac{1}{4}\Delta t \cdot \mathrm{RHS} \cdot \overline{W}_i^{n+1/3}, \\
\overline{W}_i^{n+3/3} &= \frac{1}{3}\overline{W}_i^n + \frac{2}{3}\overline{W}_i^{n+2/3} + \frac{2}{3}\Delta t \cdot \mathrm{RHS} \cdot \overline{W}_i^{n+2/3}
\end{aligned} \tag{3.8.1}$$

where RHS is the right hand side of the semi-discrete formulation (2.2.1) and Δt is the time step calculated as

$$\Delta t = \frac{\mathrm{CFL}}{d_i} \cdot \min\left(\frac{h_i}{S_i} + \frac{1}{2}\frac{h_i^2}{\mu_l + \kappa}\right) \tag{3.8.2}$$

where S_i is the maximum propagation speed for the considered element, d_i is a integer number, either 2 or 3 depending on the spatial dimensions, μ_l is the laminar dynamic viscosity, κ is the heat conductivity, h_i is the characteristic length of the element and CFL is the Courant-Friedrichs-Levy number $\leq 1/3$; it has to be noted that by increasing the discretisation order the a greater value for CFL can be employed. The characteristic length is the radius of the inscribed sphere for the considered element in three dimensions and the edge with the minimum length for two dimensions. The propagation speed is given by the following expression

$$S_i = \left|\left(n_x \cdot u + n_y \cdot v + n_z \cdot w\right)\right| \alpha \tag{3.8.3}$$

where α is the speed of sound computed as $\alpha = \sqrt{p \cdot \gamma / \rho}$. For steady-state simulations and to speed up convergence, a local time stepping method in conjunction with the

2^{nd}-order Forward Euler method are employed, the scheme is written as

$$\begin{aligned} \overline{W}_i^{n+1/2} &= \overline{W}_i^n + \frac{1}{2}\Delta t_i \cdot \mathrm{RHS} \cdot \overline{W}_i^n, \\ \overline{W}_i^{n+2/2} &= \overline{W}_i^n + \frac{1}{2}\Delta t_i \cdot \mathrm{RHS} \cdot \overline{W}_i^{n+1/2}, \end{aligned} \tag{3.8.4}$$

where Δt_i is the time step for the considered element computed according to equation (3.8.2).

CHAPTER 4

TURBULENCE MODELLING

Chapter 4 concludes the methodology part of the thesis. The chapter is devoted to turbulence modelling, starting with introductory remarks on turbulence, with a focus on the widely employed Spalart-Allmaras (SA) model. The original SA formulation is presented with all closure functions and constants, followed by Edwards modifications. The discretisation methods employed for the SA model are described, including the convective, conservative and source terms.

4.1 Introduction to Turbulence Modelling

In most fluid engineering applications such as flows over aerofoils and high-lift devices, the flow is characterized by Reynolds numbers well beyond the critical limits of turbulence, where the laminar flow transitions to turbulent. Turbulent flows contain self-sustaining fluctuations of flow properties imposed on the main flow [145].

The physical quantities are submitted to fluctuations in a wide spectrum of scales. The whole scale range can be completely resolved with Direct Numerical Simulation (DNS), where it is of crucial importance that the size of the grid and the time step are sufficiently fine to accurately capture the physical disturbances of the smallest eddies in the Kolmogorov scale. To understand the numerical effort required for DNS, consider the three-dimensional flow with a Reynolds number of $5,000$, the grid size will be in the hundreds of billions of grid points, making it unrealistic with current computational resources [146].

Over the last decades approximating methods have been developed based on averaging the fluid quantities and neglecting the small scale fluctuations, which have similar structures in all turbulent flows. By relating these fluctuations to the main flow properties, turbulence modelling is conceived. This averaging procedure introduces additional stress terms in the momentum equations called Reynolds stresses. Based on the Boussinesq hypothesis [147], the Reynolds stresses are proportional to the strain rate and therefore to the gradient of the mean flow velocity, and can be expressed as a scalar quantity: the eddy viscosity μ_t.

The evaluation of the eddy viscosity is performed with turbulence models which are based on semi-empirical observations including closure constants and functions calibrated with experimental data, DNS and Large Eddy Simulation (LES) predictions. Consequently, no single turbulence model will be adequate to accurately resolve any fluid flow. Turbulence models can be categorised as zero equation or algebraic, and one or two equations models depended on the number of PDE's employed.

The one-equation model of Spalart and Allmaras (SA) is utilised in this work as it has been extensively employed for aerodynamic applications for flows over wings and airfoils. Rogers et al. [148] have conducted an investigation comparing several turbu-

lence models: the Baldwin-Barth, the Menter's $k-\omega$ SST, the Durbin-Mansour and the Spalart-Allmaras models for a high-angle of attack multi-element airfoil subsonic flow. The pressure distribution was predicted with very little variations between the models. Furthermore, the SA model was the only one predicting stall conditions and showed the greatest amount of mixing in the wakes. The model is also "coordinate-variant", meaning that it is dependent on distances from walls, removing ambiguities related to the definition of distance functions, and is more tuned with high-order schemes in conjunction with turbulence modelling [149]. The main advantage of the SA model compared with the two-equations models is the fact that only one PDE-transport equation is solved leading to less computations and memory usage.

4.2 The Spalart-Allmaras Model

The SA turbulence model is derived based on empiricism, dimensional analysis, Galilean Invariance and the Boussinesq assumption [150]. The Boussinesq's approximation [147] relates the viscous stress tensor τ_{ij} to the Reynolds stresses through the eddy viscosity μ_t, effectively modeling the momentum transfer by turbulent eddies, written as

$$\tau_{ij} = 2\left(\mu_l + \mu_t\right)\left(s_{ij} - \frac{1}{3}\frac{\partial u_k}{\partial x_k}\delta_{ij}\right) \tag{4.2.1}$$

for simplicity and compactness two dimensions are considered, where $i = 1,2$ and $j = 1,2$ are indices, $x_i = x,y$ the Cartesian coordinates in 2D, k is the thermal conductivity, δ_{ij} is the Kronecker delta and s_{ij} is the strain rate tensor defined as

$$s_{ij} = \frac{1}{2}\left(\frac{\partial u_i}{\partial x_j} + \frac{\partial u_j}{\partial x_i}\right). \tag{4.2.2}$$

The SA model utilizes one equation to solve a transport working variable $\tilde{\nu}$ which is related to the eddy viscosity. The original SA model with the transport equation is

written in conservative, dimensionless form

$$\begin{aligned}
&\frac{\partial(\rho\tilde{\nu})}{\partial t} + \overbrace{\frac{\partial(\rho u\tilde{\nu})}{\partial x} + \frac{\partial(\rho v\tilde{\nu})}{\partial y}}^{\text{Convective term}} = \\
&\overbrace{\frac{1}{Re_a}\frac{1}{\sigma}\left[\left(\frac{\partial}{\partial x}\left(\rho\left(\nu+\tilde{\nu}\right)\frac{\partial\tilde{\nu}}{\partial x}\right) + \frac{\partial}{\partial y}\left(\rho\left(\nu+\tilde{\nu}\right)\frac{\partial\tilde{\nu}}{\partial y}\right)\right) + \left(\left(\nu+\tilde{\nu}\right)\left(\frac{\partial\tilde{\nu}}{\partial x}\frac{\partial\rho}{\partial x} + \frac{\partial\tilde{\nu}}{\partial y}\frac{\partial\rho}{\partial y}\right)\right)\right]}^{\text{Conservative diffusive term}} \\
&+ \overbrace{\frac{\rho}{Re_a}\frac{C_{b2}}{\sigma}\left[\left(\frac{\partial\tilde{\nu}}{\partial x}\right)^2 + \left(\frac{\partial\tilde{\nu}}{\partial y}\right)^2\right]}^{\text{Non-conservative diffusive term}} + \overbrace{\rho C_{b1}\left[1-f_{t2}\right]\left(S\tilde{\nu} + \frac{1}{Re_a}\frac{\tilde{\nu}^2}{k^2d^2}f_{v2}\right)}^{\text{Production term}} \\
&- \overbrace{\frac{\rho}{Re_a}\left[C_{w1}f_w - \frac{C_{b1}}{k^2}f_{t2}\right]\left(\frac{\tilde{\nu}}{d}\right)^2}^{\text{Near-wall destruction term}} + \overbrace{\rho Re_a f_{t1}\left(\Delta U\right)^2}^{\text{Transition ``trip-term''}} .
\end{aligned} \tag{4.2.3}$$

The turbulence parameter $\tilde{\nu}$ is related to the eddy viscosity μ_t as

$$\mu_t = \rho\tilde{\nu}f_{v1} \tag{4.2.4}$$

where

$$f_{v1} = \frac{\mathcal{X}^3}{\mathcal{X}^3 + C_{v1}^3} \quad \text{and} \quad \mathcal{X} = \frac{\rho\tilde{\nu}}{\mu_l} \quad \text{where} \quad C_{v1} = 7.1 \tag{4.2.5}$$

where μ_l is the laminar viscosity computed according to Sutherland's approximation and C_{v1} is a model constant. At this point only fully turbulent flows are considered so the "trip-terms" f_{t1} and f_{t2} related to transition locations are zeroed out.

Edwards modification of the SA model is employed as it improves near-wall convergence, both in terms of smoothness and speed [151]. The main difference from the original model is in the production source term of equation (4.2.3), where the vorticity magnitude S is replaced with strain-rate norm $\tilde{S}$, thus the production term can be rewritten in dimensional form as

$$\text{Production} = C_{b1}\tilde{S}\tilde{\nu}\rho \quad \text{and} \quad \tilde{S} = \bar{S}\left(f_{v1} + \frac{1}{\max(\mathcal{X}, \epsilon_c)}\right) \quad \text{where} \quad C_{b1} = 0.1355 \tag{4.2.6}$$

where

$$\bar{S} = \sqrt{2\left[\left(\frac{\partial u}{\partial x}\right)^2 + \left(\frac{\partial v}{\partial y}\right)^2\right] + \left(\frac{\partial u}{\partial y} + \frac{\partial v}{\partial x}\right)^2 - \frac{2}{3}\left(\frac{\partial u}{\partial x} + \frac{\partial v}{\partial y}\right)}. \tag{4.2.7}$$

To preserve positivity of the model the $\bar{S}$ is limited to take only positive values [151].

The destruction term is redefined in dimensional form as

$$\text{Destruction} \;=\; C_{w1}\, f_w(r)\tilde{\nu}\rho \quad \text{where} \quad r = \frac{\tanh\left(\dfrac{\tilde{\nu}\rho}{(\kappa d)^2\,\tilde{S}}\right)}{\tanh(1.0)} \tag{4.2.8}$$

where d is the distance between the element centroid to the nearest wall (face-center), for computational efficiency, the distance is computed and pre-stored during the initialisation procedure. The auxiliary functions of the destruction source terms are given

$$f_w(r) = g\left(\frac{1 + C_{w3}^6}{g^6 + C_{w3}^6}\right)^{1/6} \quad \text{where} \quad g = r + C_{w2}\left(r^6 - r\right) \tag{4.2.9}$$

the non-conservative diffusion in dimensional form is defined as

$$\text{Diffusion} \;=\; \frac{\rho C_{b2}}{\sigma}\|\nabla\tilde{\nu}\|^2 \tag{4.2.10}$$

and finally the closure constants

$$\begin{aligned} &C_{b2} = 0.622, \quad C_{w1} = \frac{C_{b1}}{\kappa^2} + \frac{1 + C_{b2}}{\sigma}, \quad C_{w2} = 0.3 \\ &C_{w3} = 2.0, \quad \sigma = 2/3, \quad \kappa = 0.41. \end{aligned} \tag{4.2.11}$$

The eddy viscosity is coupled with the NS equations during the evaluation of the viscous fluxes (2.1.7), the normal and shear stresses are redefined as

$$\begin{aligned} &\tau_{xx} = 2(\mu_l + \mu_t)\frac{\partial u}{\partial x} + \lambda\left(\frac{\partial u}{\partial x} + \frac{\partial v}{\partial y}\right), \;\; \tau_{yy} = 2(\mu_l + \mu_t)\frac{\partial v}{\partial y} + \lambda\left(\frac{\partial u}{\partial x} + \frac{\partial v}{\partial y}\right), \\ &\tau_{xy} = \tau_{yx} = 2(\mu_l + \mu_t)\left(\frac{\partial u}{\partial y} + \frac{\partial v}{\partial x}\right) \end{aligned} \tag{4.2.12}$$

and the heat fluxes

$$q_x = -\left(\frac{\mu_l}{P_r} + \frac{\mu_t}{P_t}\right)\left(\frac{1}{\gamma - 1}\right)\frac{\partial T}{\partial x}, \quad q_y = -\left(\frac{\mu_l}{P_r} + \frac{\mu_t}{P_t}\right)\left(\frac{1}{\gamma - 1}\right)\frac{\partial T}{\partial y} \tag{4.2.13}$$

where P_t is the turbulent Prandtl number, for turbulent flows a value of 0.9 is assigned, based on empiricism.

At the edge of the boundary layer, the eddy viscosity value becomes free-stream over a minute narrow layer; if not resolved appropriately, $\tilde{\nu}$ can exhibit unphysical

behaviour and even drop to negative values [152, 153]. This must be avoided as there is no physical meaning of negative viscosity and it will lead to divergence of the solution. Maintaining $\tilde{\nu}$ positive also enables the 1^{st} and 2^{nd}-order derivatives to be continuous [154]. One ad-hoc solution for positivity preserving of $\tilde{\nu}$ is to limit the turbulence parameter $\tilde{\nu}$; if it becomes negative then clip it to zero [154]. Nevertheless, during the reconstruction of the turbulence parameter gradient $\nabla\tilde{\nu}$ for an element having in its stencil a troubled element ($\tilde{\nu} = 0$), $\tilde{\nu}$ becomes several orders of magnitude lower compared with its direct-side neighboring element value, ergo the solution diverges.

4.3 Turbulence Model Discretisation

The discretisation of the turbulence transport equation conservative terms is performed in a similar fashion as the Navier-Stokes fluxes, each term convective, diffusive and sources is treated with an appropriate numerical scheme. High-order discretisation of the turbulence parameter and coupling with the main governing equations convective flux algorithm under-predicts the amount of turbulent viscosity, introduces excessive artificial dissipation with negative values of $\tilde{\nu}$ consequently leading to a failure of the model [65]. Therefore, the convective term of the SA turbulence requires a low-order discretisation and a decoupled formulation from the main governing equations. However, the diffusive and source terms of the SA model contain 1^{st} and 2^{nd} order derivatives that are reconstructed in similar manner as the gradients of the NS equations.

4.3.1 Convective Term

The convective turbulent flux can be evaluated in a similar fashion to the mean variable convective fluxes by employing an appropriate high-order Gaussian quadratures rule. Nevertheless, there are several subtle issues that arise when higher than 1^{st}-order accurate discretisation methods are used for the turbulent convective flux such as low estimation of the eddy viscosity, negative values of the turbulence parameter and ultimately divergence of the model. This behaviour was recently studied by Burgess and Mavriplis [65] confirming that the most stable combination is the 1^{st}-order FV

discretisation uncoupled from the Riemann solver, generating an artificial dissipation in equilibrium; not too low for the turbulence parameter to drop to negative levels, not high enough for the eddy viscosity to reach low values and misleading physical behaviours.

First-order upwind discretisation is proven to be a robust choice for the convective turbulent fluxes of the SA model. DLR's *TAU* solver [155] employs a fully upwind 1^{st}-order discretisation combined with Edwards modification of the SA model; it has been widely employed for aerodynamic flows with overall accurate predictions [156]. TAU's convective discretisation of the turbulence parameter $\tilde{\nu}$ is implement as presented by Dwight [157] uncoupled from the mean flow variables and Riemann solver. The convective turbulent flux ${}^{c}\hat{F}^{\tilde{\nu}}$ is computed as

$$ {}^{c}\hat{F}^{\tilde{\nu}} = \frac{1}{2}\left[\mathcal{N}\left((\rho\tilde{\nu})^{-} + (\rho\tilde{\nu})^{+}\right) - |\mathcal{N}|\left((\rho\tilde{\nu})^{+} - (\rho\tilde{\nu})^{-}\right)\right] \tag{4.3.1} $$

where $(\rho\nu)^{-}$ and $(\rho\nu)^{+}$ are the cell-centered values for the considered element and of its direct side neighbour respectively, with $\mathcal{N}$ defined as

$$ \mathcal{N} = \frac{1}{2}\left[n_x\left(u^{-} + u^{+}\right) + n_y\left(v^{-} + v^{+}\right)\right] \tag{4.3.2} $$

where $u^{\pm}$, $v^{\pm}$ are the cell-centered values for the Cartesian velocity components. For a high-order discretisation of the NS equations it would be attractive to employ reconstructed boundary extrapolated values for the density and/or the velocities instead of the cell-centered ones. Unfortunately, this has an adverse effect on the convergence, predicting unsatisfactory levels of eddy viscosity and oscillations in the vicinity of strong vortical flows; Figure 4.1 on page 56 demonstrates this unphysical behaviour where μ_t/μ_∞ contours are plotted for the turbulent flow past a multi-element aerofoil. This can be attribute to the fact that the values for the turbulence parameter are not piecewise constant as inner-cell variations are introduced. Furthermore, the employment of a limiting function for piecewise linear reconstruction does not guarantee either stability of the turbulence model [65].

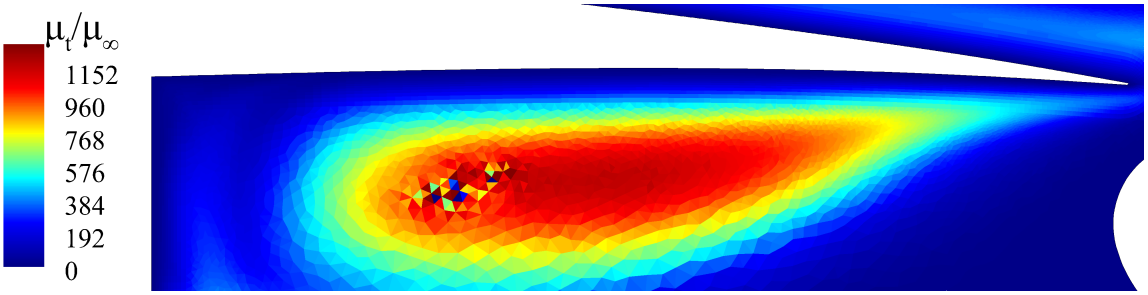

Figure 4.1: Flow contaminations with inaccurate eddy viscosity values, by employing reconstructed boundary extrapolated values for the SA turbulent convective discretisation; normalised eddy viscosity with free-stream viscosity contours are shown (μ_t/μ_∞) for the turbulent flow past the MDA 30P-30N three-element aerofoil ($M_\infty = 0.2$, $\alpha = 16^\circ$ and $R_e = 9.0 \times 10^6$).

4.3.2 Diffusive Term

The conservative diffusive fluxes of the turbulence transport equation are evaluated in a similar manner as the viscous fluxes of the NS equation. The reconstruction of the turbulent parameter gradient $\nabla\tilde{\nu}$ is performed in a similar fashion as the temperature gradient of the NS equations in Section 3.6.1. The conservative diffusive flux of SA model is written as

$$ {}^{d}\vec{F}^{\tilde{\nu}} = -\frac{1}{|V_i|}\sum_{j=1}^{L}\sum_{\beta=1}^{B} {}^{d}\hat{F}^{\tilde{\nu}}_{j,\beta}\,\omega_\beta |A_j| \tag{4.3.3} $$

where the ${}^{d}\hat{F}^{\tilde{\nu}}_{j,\beta}$ is evaluated by averaging the extrapolated values and gradients from left and right states yielding

$$ {}^{d}\hat{F}^{\tilde{\nu}}_{j,\beta} = \frac{1}{\sigma}\left[\left(\frac{\mu_l^- + \mu_l^+}{2} + \frac{\mu_t^- + \mu_t^+}{2}\right)\nabla\tilde{\nu}\right] \tag{4.3.4} $$

where the gradient is computed as

$$ \nabla\tilde{\nu} = n_x\frac{1}{2}\left(\frac{\partial\tilde{\nu}}{\partial x}\bigg|^{-} + \frac{\partial\tilde{\nu}}{\partial x}\bigg|^{+}\right) + n_y\frac{1}{2}\left(\frac{\partial\tilde{\nu}}{\partial y}\bigg|^{-} + \frac{\partial\tilde{\nu}}{\partial y}\bigg|^{+}\right). \tag{4.3.5} $$

4.3.3 Source Terms

In the previous section the original source terms along with the modification of Spalart-Allmaras-Edwards were introduced. The source terms are evaluated with a standard volume Gaussian quadrature formula for a triangle as previously presen-

ted in Table 3.3 on page 35 or with Keast quadrature formula for a tetrahedron in three dimensions [158]. In two dimensions quadrilateral surfaces are decomposed to two triangles and the source terms are discretised as

$$\mathrm{S}_i = \frac{1}{|V_i|} \sum_{k=1}^{K} \sum_{\beta=1}^{B} |V_k| \, \mathbf{S}(\mathrm{x}_\beta) \omega_\beta \tag{4.3.6}$$

where $\mathbf{S}$ = Production − Destruction + Diffusion, K is the total number of element decompositions, x_β being the volume Gaussian quadrature point coordinates, required for the computations of the velocity gradients for estimating the mean strain rate $\bar{S}$ in (4.2.7) as well as the square gradient of the turbulence parameter $\|\nabla\tilde{\nu}\|$ in (4.2.10), see Table 3.3 on page 35.

One of the flows undertaken in Chapter 7 is the supersonic flow through an inclined channel at a high Reynolds number, where shock-wave turbulent boundary-layer interactions occur. It has been reported that the original SA model will inefficiently predict the skin friction and the wall heat flux [159]. There are several modification to account for supersonic regimes and compressibility effects, a review can be found in [159]. A robust and elegant modification is adopted by simply including in the square gradient of the turbulence parameter $\|\nabla\tilde{\nu}\|$ the density [160]. This modification applies only for the non-conservative diffusive term, yielding

$$\text{Diffusion} \;=\; \frac{\rho C_{b2}}{\sigma} \|\nabla\rho\tilde{\nu}\|^2. \tag{4.3.7}$$

CHAPTER 5

INVISCID APPLICATIONS

The previous chapters elucidate all aspects related to the theoretical fundamentals and numerical frameworks. Consequently, starting with this chapter, a broad envelope of applications are simulated for validating and scrutinizing the developed numerical methods. This chapter covers inviscid flow computations including grid convergence and grid dependence studies and the performance of the scheme is assessed in terms of performance and robustness. The Taylor-Green vortex flow is emulated to study the dynamics of turbulence transition; and assess the numerical dissipation of the developed WENO schemes to several grid types. The second test case is the transonic inviscid flow over the ONERA-M6 wing at a positive angle of attack, evaluating the shock capturing abilities of WENO algorithms on complex three-dimensional geometries.

5.1 Taylor-Green Vortex

The Taylor-Green vortex (TGV) flow is considered a benchmark case for studying transition to turbulence, triggered by vortex stretching and production of smaller scales [161]. In the context of the implicit large eddy simulation (ILES) approach by high-order non oscillatory finite volume schemes, the small scales are implicitly resolved [162], where the non-linear limiters (WENO) behave as sub-grid scale (SGS) filters encountered in the LES framework [163]. Boris [164] demonstrated that this behaviour emerges from the truncation (discretisation) error of these schemes which in turns arises from the high-order reconstruction of the convective fluxes. In other words, high-order WENO algorithms will produce numerical dissipation, enough to account for a turbulent regime, even though no viscous terms are computed [143, 165, 166]; the quantification of the inherited numerical dissipation and consequently the resolved physical viscosity (or corresponding Reynolds number) is conceived by computing the evolution of total kinetic energy spectra K_{total} and the kinetic energy dissipation rate $-dK^*/dt$ and comparing them with DNS results [161, 167].

Since, the grid size employed is significantly larger than the Kolmogorov scale, the viscous effects can be neglected, and the inviscid Euler's equations are solved. The TGV flow is a three-dimensional, incompressible flow initialised with two-dimensional solenoidal velocity components defined as:

$$\begin{aligned} u_0 &= \sin(kx)\cos(ky)\cos(kz), \\ v_0 &= -\cos(kx)\sin(ky)\cos(kz), \\ w_0 &= 0 \end{aligned} \tag{5.1.1}$$

where, the wavenumber relating to the length scale is $k = 2\pi/\lambda = 1$, the density and pressure are given by

$$\begin{aligned} \rho_0 &= 1, \\ p_0 &= 100 + \frac{\rho}{16}\left[(\cos(2z)+2)\left(\cos(2x)+\cos(2y)\right)-2\right] \end{aligned} \tag{5.1.2}$$

the initial pressure is derived from the pressure poison equation, the value 100 is chosen to limit the pressure so the flow remains in the incompressible regime [168] at a Mach number of $M \approx 0.08$. Note that, the two-dimensional velocity initial profile

will evolve to a three-dimensional flow driven by the pressure gradient in equation (5.1.2).

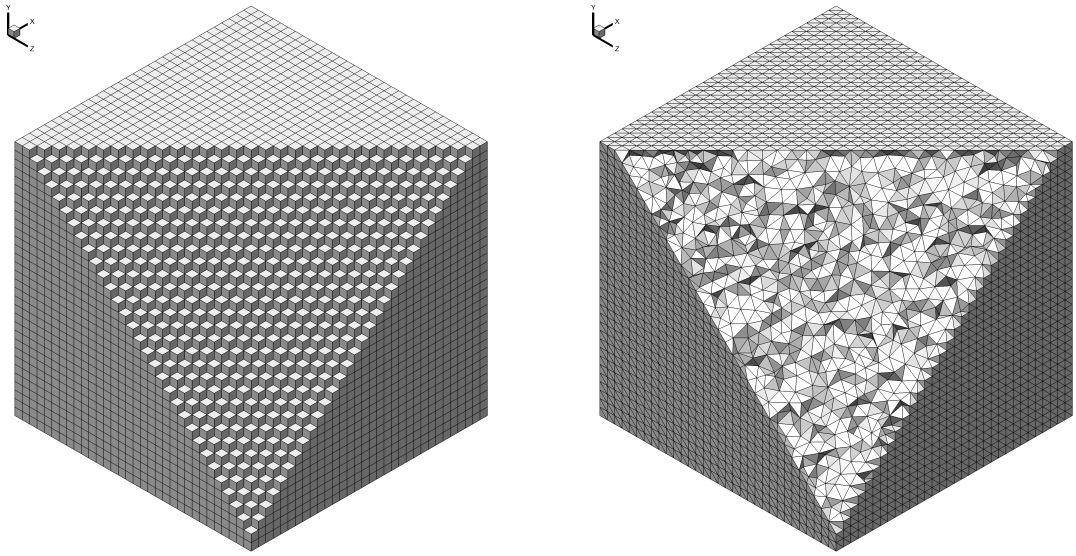

(a) Medium hexahedral (b) Medium tetrahedral

Figure 5.1: Medium grids [32^3] employed for Taylor-Green vortex flow

Six cube-shaped spatial grids are employed for the TGV flow, three hexahedral and three tetrahedral; the grids parameters are shown in Table 5.1 on page 61, where the degrees of freedom are shown per conserved variable for each scheme. The outer spatial domain is located at $(x, y, z) \in [0, 2\pi] \times [0, 2\pi] \times [0, 2\pi]$; with periodic boundary conditions being enforced on all six outer surfaces; the grids were generated with ANSYS-ICEMCFD [81]; Figures 5.1 show the medium [32^3] grids. The computations were performed with the 3^{rd} and 5^{th}-order WENO schemes, a CFL number of 0.28 with the 3^{rd}-order TVD Runge-Kutta time advancement algorithm.

Table 5.1: Grid parameters for Taylor-Green vortex flow

	Nodes	Elements	DOF×10^6	
			WE3	WE5
Hexahedral				
Coarse [16^3]	4,913	4,096	0.25	0.97
Medium [32^3]	35,937	32,768	2.06	7.79
Fine [64^3]	274,625	262,144	16.51	62.39
Tetrahedral				
Coarse [16^3]	5,033	25,320	1.13	4.30
Medium [32^3]	22,399	115,804	5.21	19.68
Fine [64^3]	274,625	1,572,864	70.77	267.38

The objective of the TGV computations are summarized

- study the dynamics of homogeneous decaying turbulence
- quantify the inherited numerical dissipation of WENO schemes depended upon the polynomial order and the employed grid (type and size)
- compare the conservation error of the developed WENO scheme with the original WENO formulation

In theory, for an inviscid incompressible flow, the kinetic energy should be conserved, as no viscous effects are considered to damp it to heat [169, 170]. Actually, the kinetic energy dissipation trends will resemble the viscous effects; furthermore, the dissipation is beneficial for numerical schemes as long as it is less than the physical viscosity. The observation of the kinetic energy dissipation enables to study and analyse the inner mechanisms of dissipation, depending upon the type of scheme and grid employed. In Figure 5.4 on page 65 the volumetrically averaged kinetic energy decay in time is shown for all simulations, for reference Shu et al. [168] results are included. As expected, by either applying polynomial or grid refinement the kinetic energy is further conserved and the numerical dissipation is reduced.

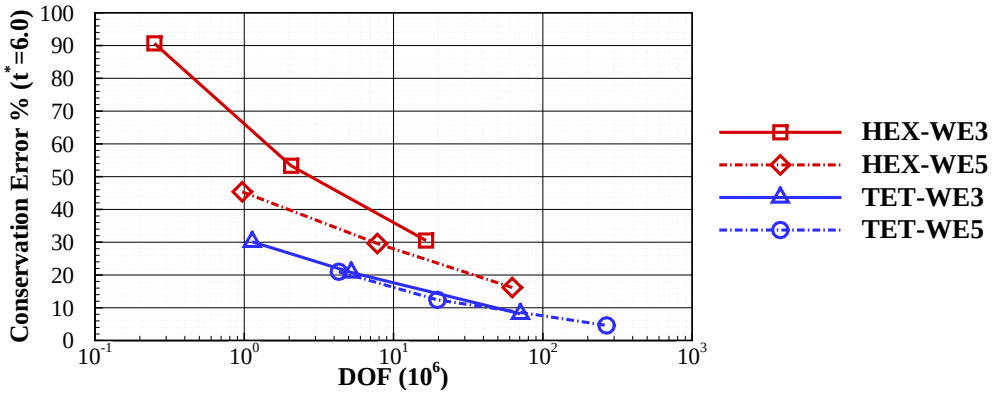

Figure 5.2: Kinetic energy conservation error at time $t^* = 6.0$ against the degrees of freedom (DOF) per conserved variable, for the Taylor-Green vortex flow for all grids and schemes

The immediate observation is that the tetrahedral grids outperform the hexahedral ones in terms of kinetic energy conservation, even with the hexahedral grid at higher resolutions; this is also supported with Figure 5.2 on page 62 where the conservation error is plotted against the DOF per conserved variable. The tetrahedral performance seems to originate from its geometrical characteristics, where its arbitrary orientation in space is more in tune with the chaotic three-dimensional vortical structure illustrated in Figure 5.5 on page 66. Furthermore, the fact that tetrahedra possess four faces compared to six of the hexahedra, results in a markedly compacter stencil which is beneficial for maintaining a low numerical dissipation.

For the same grid size the 5^{th}-order WENO scheme of Shu et al. [168] inherits a greater dissipation compared with the hexahedral 5^{th}-order WENO scheme predictions. It must be noted, that the method employed by Shu et al. is based on the original WENO formulation, with the Lax-Friedrichs flux splitting method. In addition, the k-exact method of this current work is computational more expensive than this of Shu et al. [168].

As mentioned earlier, the kinetic energy dissipation rate is a useful measure to study the trends of the dissipation mechanisms of each scheme and grid by comparing them with DNS results. Brachet [161, 167] conducted DNS simulations of the TGV flow and predicted the energy dissipation peak at $t^* \approx 9$ for the following Reynolds numbers $Re = 800, 1600, 3000$ shown in Figure 5.3 on page 63; where the kinetic energy dissipation rates is plotted in time for hexahedral, tetrahedral and fine grids. It is immediately obvious that the cases with low kinetic energy dissipation (greater grid

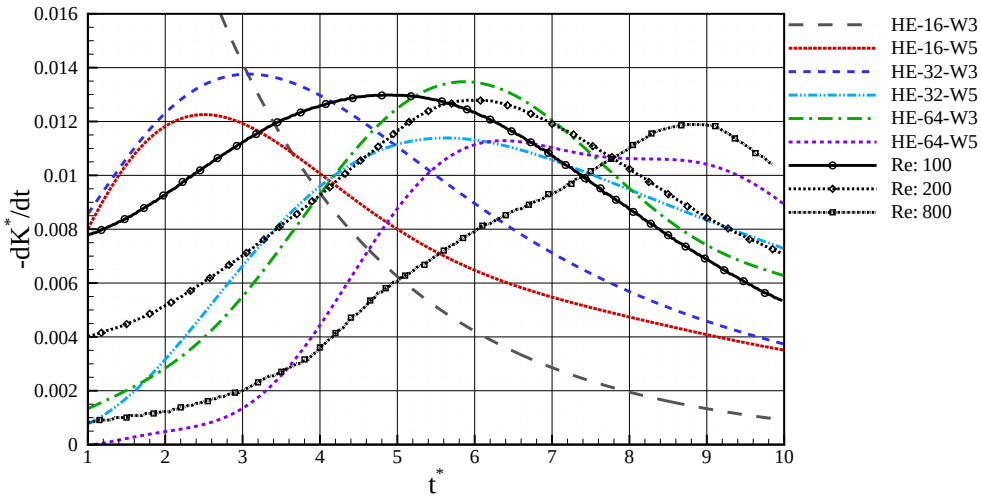

(a) Hexahedral grids

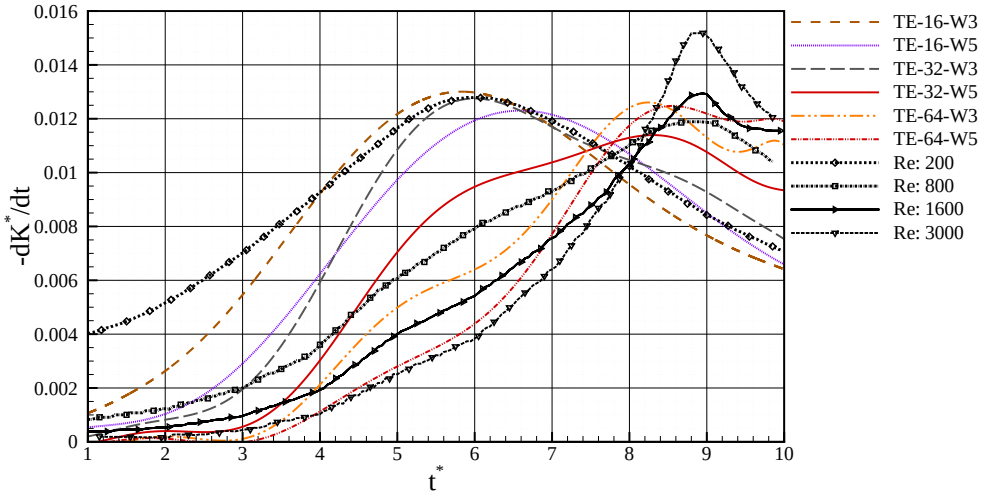

(b) Tetrahedral grids

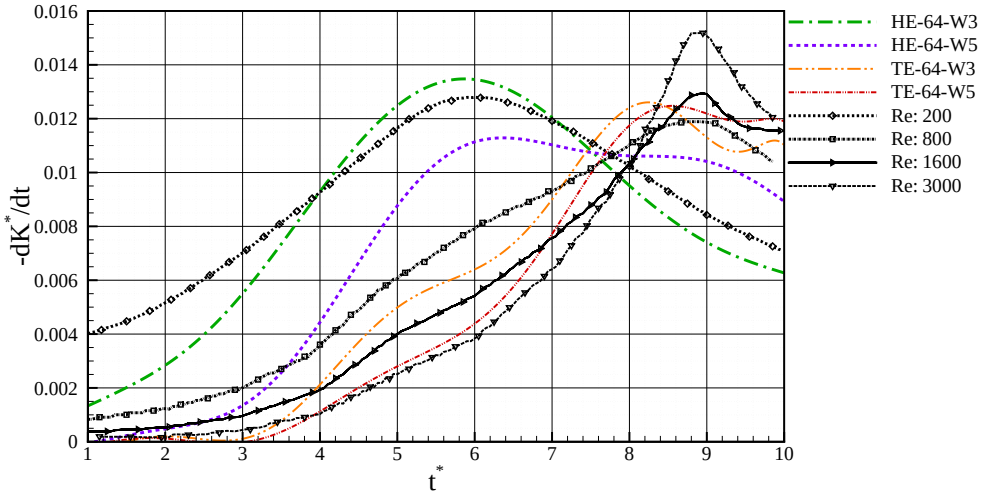

(c) 64^3 grids

Figure 5.3: Volumetrically averaged kinetic energy decay rate (dK^*/dt) in time (t^*) for the Taylor-Green vortex flow, shown for all schemes and grids where HE and TE refers to hexahedral and tetrahedral grids respectively, and W3 and W5 for 3^{rd} and 5^{th}-order WENO schemes; Reynolds numbers (Re) correspond to DNS results from Brachet et al. [167].

and/or polynomial refinement) correspond to a higher Re trend. It appears that for the higher Re, the peaks remain nearly identical for almost twice the Re, suggesting a Re-independence limit [171]. This seems to be the pattern for the 64^3 cases in Figure 5.3 on page 63 (c), where the tetrahedral WE3 and WE5 corresponding to a higher Re number have smaller peak difference compared with the hexahedral WE3 and WE5; this suggest, that the Re-independence limit could be correlated with a numerical dissipation independence limit.

The dynamics of the TGV flow regime are shown in Figure 5.5 on page 66; where the iso-contours show the Q-Criterion [172] at a value zero, colored with the kinetic energy at six times snapshots. The instantaneous visualisations are computed for the WENO 5^{th}-order scheme on the fine tetrahedral grid (64^3), for preserving consistency, the levels of Q-Criterion and kinetic energy are the same for all snapshots. At $t^* = 2$ the vortices structure is organised and large symmetric features dominate the dynamics of the flow. Advancing in time, these large scale vortices transition to smaller ones, gradually breaking the symmetrical patterns to a disorganized decaying flow field characterized by the chaotic nature of turbulence [173].

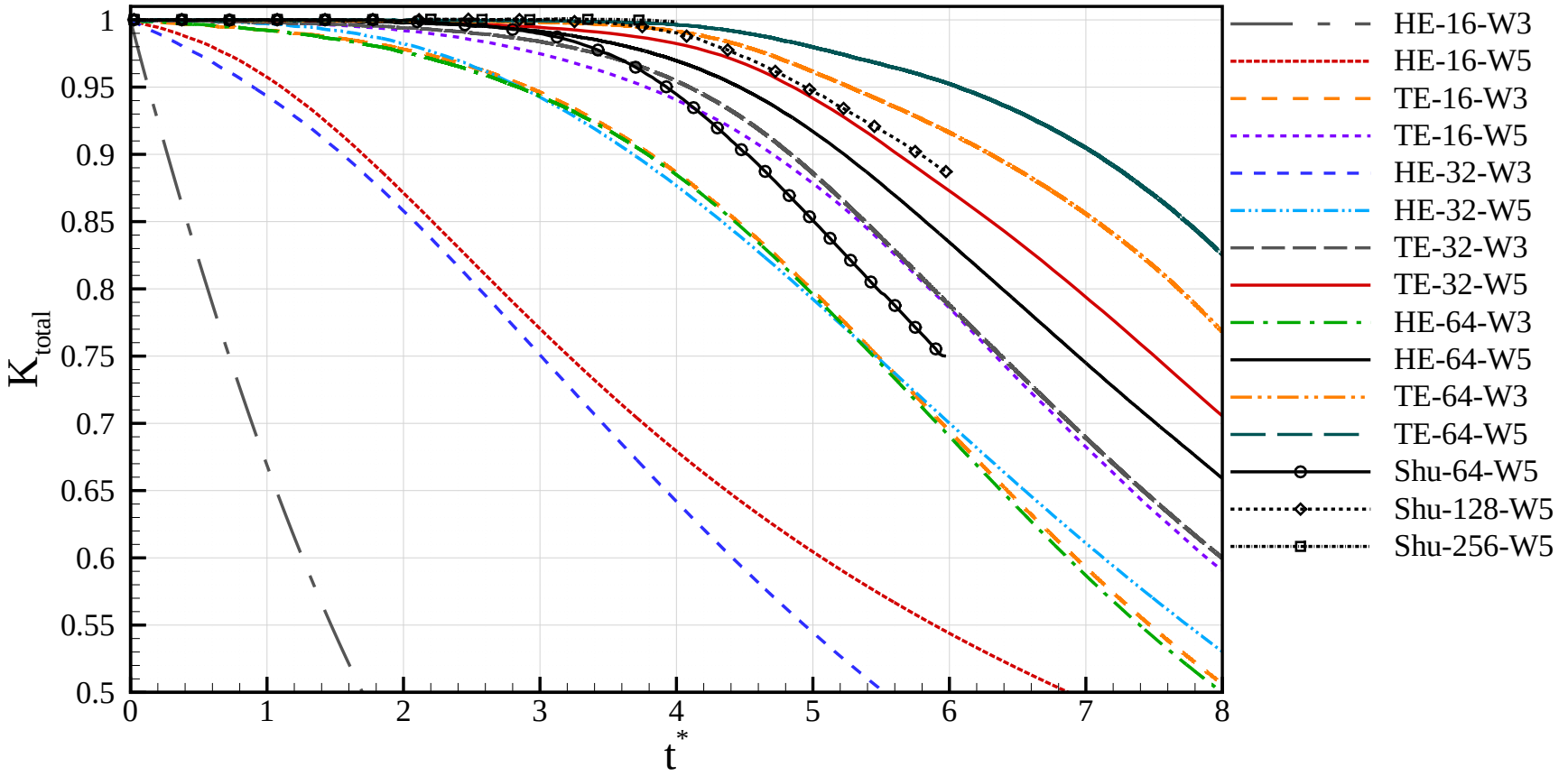

Figure 5.4: Time evolution of the normalised kinetic energy K_{total} for the Taylor-Green vortex flow, plotted for 8 sec^* for all schemes and grids and compared with the WENO 5^{th}-order accurate results of Shu et al. [168] for three structured grids 64^3, 128^3 and 256^3, performed with the original WENO 5^{th}-order formulation.

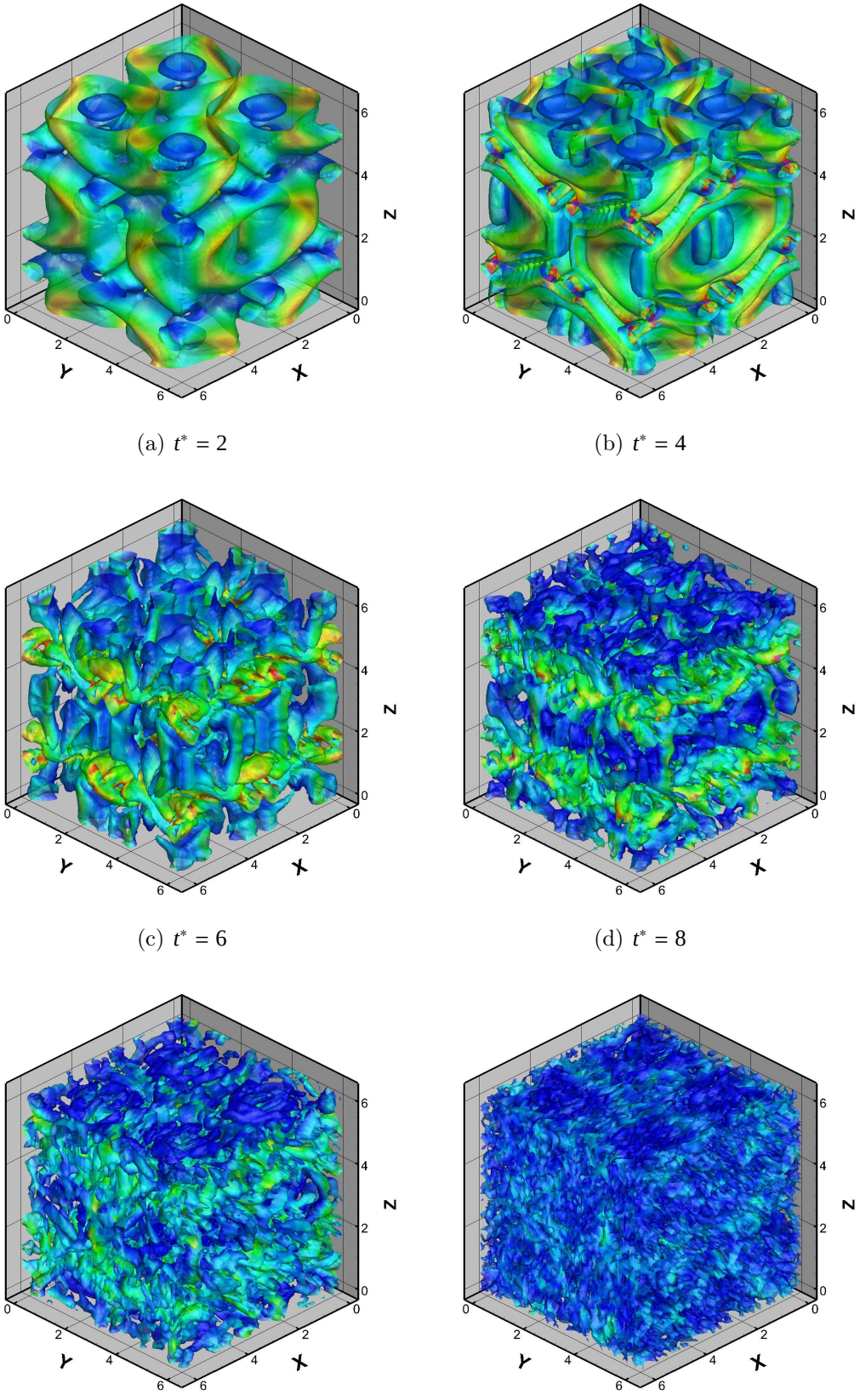

(a) $t^* = 2$ (b) $t^* = 4$

(c) $t^* = 6$ (d) $t^* = 8$

(e) $t^* = 10$ (f) $t^* = 14$

Figure 5.5: Instantaneous visualizations of the Taylor-Green vortex flow, employing iso-surfaces of Q-Criterion= 0 colored with kinetic energy, results shown for the fine tetrahedral (64^3) with the WENO 5^{th}-order scheme.

5.2 Transonic Flow over ONERA-M6 Wing

A standard validation problem for three-dimensional CFD solvers is the ONERA-M6 wing; solutions are computed for the inviscid flow around the wing with a freestream Mach number of $M_\infty = 0.84$ and an angle of attack at $a = 3.06°$. This test case is particularly important as it enables to capture the characteristics of inviscid transonic phenomena. Experiments were performed in 1979 by Schmitt and Charpin [174], where pressure coefficient was measured with an estimated error of ± 0.02. Even though the experiment and the actual physical conditions involve viscous features at a relatively high Reynolds number $Re = 2.6 \times 10^6$, the transonic effects such as multiple shock configurations (λ-structure double shock), can be efficiently captured with Euler's formulation [71, 175–178]. The actual geometry configuration is a swept, semi-span wing, with no twist, and symmetrical airfoil sections with a rounded tip; Table 5.2 on page 67 details the wing's geometry parameters.

Table 5.2: Geometry parameters of ONERA-M6 wing

Span(b)	1.1963 meters
Mean aerodynamic chord (c)	0.64607 meters
Aspect ratio	3.8
Taper ratio	0.562
Leading-edge Sweep	30.0°
Trailing-edge Sweep	15.8°

The objectives of this test case are:

- validate the high-order discretisation for the inviscid terms for 3-D transonic flows, including the HLLC Riemann solver and the WENO characteristic based reconstruction
- assess the shock-capturing abilities of WENO limiters on two spatial grids
- compare the computed pressure coefficient with the experimental data

Two unstructured tetrahedral-based grids were generated, one relatively coarse and one fine, referred to GRID-1 and GRID-2 respectively; Table 5.3 on page 68

details the statistics of each grid. Figure 5.6 on page 69 illustrates the element distributions on the wing's surface, note that: GRID-1 is constructed with arbitrary distributed triangles, while GRID-2, quadrilaterals were first generated and then diagonilized to triangles to improve the overall smoothness and homogeneity of the wing's surface elements. ANSYS-ICEM-CFD® [81] grid-generation software was used to create GRID-1, whereas for GRID-2, the surfaces were meshed with Pointwise® [80] software and imported to ANSYS-ICEM-CFD® to generate the final volume mesh with the advancing front technique [179]. The far field is located at $[-15 \leq x \leq 15] \times [-15 \leq y \leq 15] \times [0 \leq z \leq 15]$, characteristic boundary conditions are imposed on the outer boundaries, the z plane is set as symmetric BC and inviscid wall BC for the wing's surface.

Table 5.3: Grid parameters for the inviscid flow over the ONERA-M6 wing.

	Tetrahedrals	Nodes	Triangles on wing's surface	DOF $\times 10^6$
GRID-1-WE3	347,847	62,438	9,355	15.65
GRID-1-WE5	347,847	62,438	9,355	59.13
GRID-2-WE3	1,663,912	303,529	100,766	74.87

The 3^{rd} and 5^{th}-order WENO schemes were employed for the simulations with the 3^{rd}-order TVD-Runge-Kutta explicit time advancing scheme and a CFL number of 0.4. Figure 5.7 on page 71 shows the computed Mach number contour lines and pressure coefficient contours for both the upper and lower parts of the wing for GRID-1 using WENO 3^{rd} and 5^{th}-order schemes. The induced λ-structure shock in the vicinity of the leading edge and tip, formed by the collision of the shock-wave pair, is clearly depicted. The WE5 scheme captures the shocks more sharply than WE3, with fewer noise, this can be observed for the Mach number line at 0.97. The coalesced pair of shocks on the upper wing's surface is also visible for the coefficient of pressure contour levels, where the pressure reaches its minimum value downstream from the strong shock on the leading edge of the wing.

Any shock-capturing numerical scheme will drop to 1^{st}-order of accuracy near a discontinuity as the error at this location is proportional to the grid size [15]. This aspect makes grid refinement the fundamental requirement for accurately resolving a

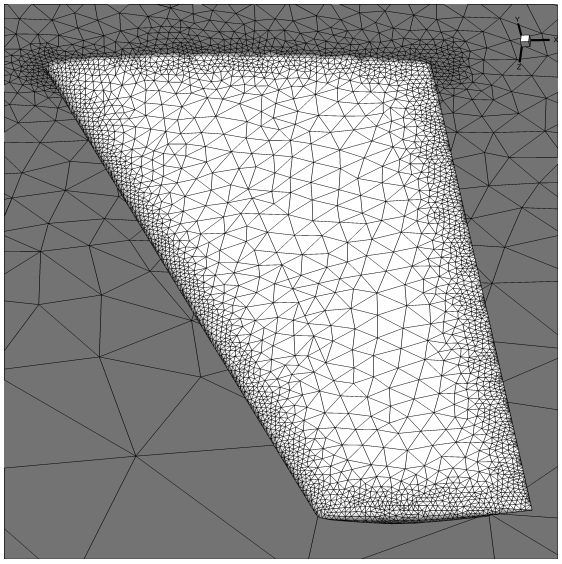

(a) GRID-1

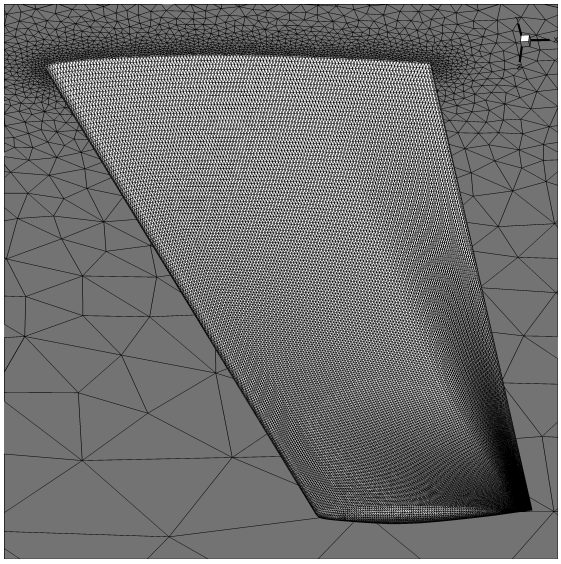

(b) GRID-2

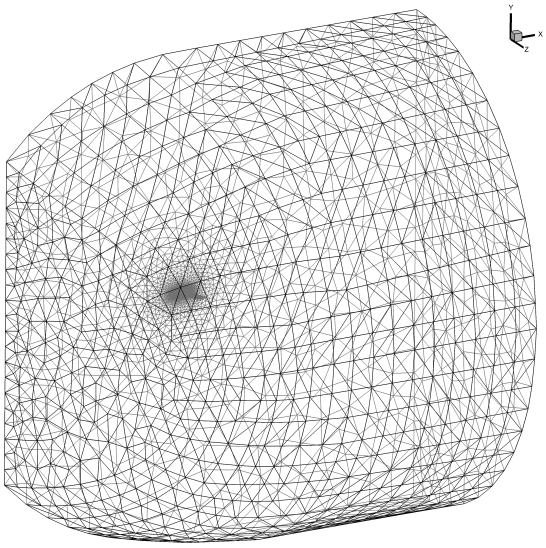

(c) Far-field GRID-2

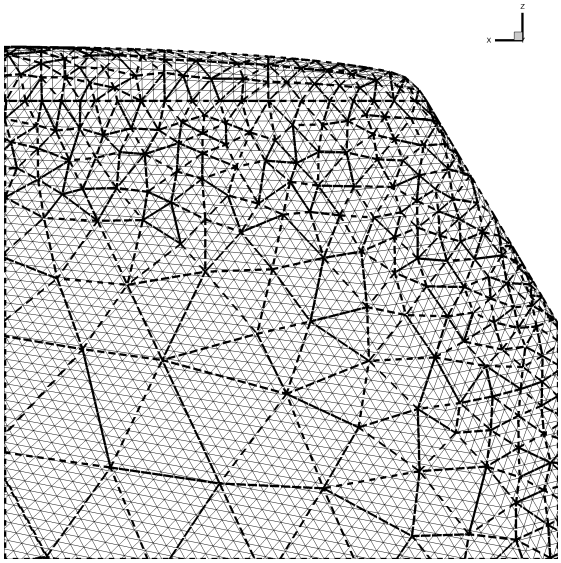

(d) Zoomed surface grids

Figure 5.6: (a) and (b) illustrate the triangle distributions on the wings's upper surface for GRID-1 and GRID-2 respectively, (c) is an overview of the far-field domain and (d) shows the differences of the triangles distribution of GRID-1 and GRID-2 near the wing's leading edge and tip.

shock, demonstrated in Figure 5.8 on page 72 where Mach number contour lines and coefficient of pressure contours are shown for GRID-2 employing WENO 3^{rd}-order scheme. GRID-2 having more than ten times the number of elements on the wing's surface than GRID-1, captures the shock considerably better than both WE3 and WE5 schemes with GRID-1, where details such as the curvature of the weak shock (Mach number line :0.97) are hardly noticeable with GRID-1. The complex nature of this double-shock configuration is substantiated from the results of GRID-2, where secondary flow features become apparent i.e. the mirrored scaled-down λ shock on the leading part of the tip and the small rise of pressure downstream of the collision of the pair of shocks.

Figure 5.9 on page 74 shows the computed wall pressure coefficients for all simulations and grids compared with the experimental data of Schmitt and Charpin [174] at six span-wise sections. The abscissa in the plots is the ratio of the x cartesian coordinate over the local chord c and the ordinate is the coefficient of pressure (C_p). All numerical results are consistent with the experimental data and capture the shocks reasonably well in terms both of location and intensity. Furthermore, the strong shock on the leading edge at $x/c \approx 0$ for all stations is resolved better with the GRID-2-WE3 results, discrepancies are noticed for the GRID-2-WE3 for the station near the wing root $z/b = 20\%$ at the upper side at $x/c \approx 0.6$ where the shock location is slightly translated towards the trailing edge. This discrepancy stems from the inviscid nature of Euler's equations contradicting with the viscous turbulent regime of the physical reality, similar behavior has been extensively reported in [175, 178, 180]. To account for this issue it has been suggested one should modify the geometry of the wing to be used for inviscid flow simulations [181].

At stations $(z/b = 65\%)$ and $(z/b = 80\%)$, GRID-1-WE3 suggests a smeared shock at the midsection of x/c, this is attributed to the poor quality of the grid at this location where the double shock is resolved only in one element; however, by increasing the order of the scheme with WE5 the shock location is captured more accurately. The overshoot of C_p for the finer grid at stations $z/b = 80\%$ and $z/b = 90\%$ between $0.3 < x/c < 0.5$ can be associated with the fact that the finer grid inherits a lower numerical dissipation compared with the coarser grid, coupled with the fact that the physical diffusion of the viscous and turbulent terms is not modelled, leads to the prediction of discontinuities with sharper profiles. Finally, for all stations for the

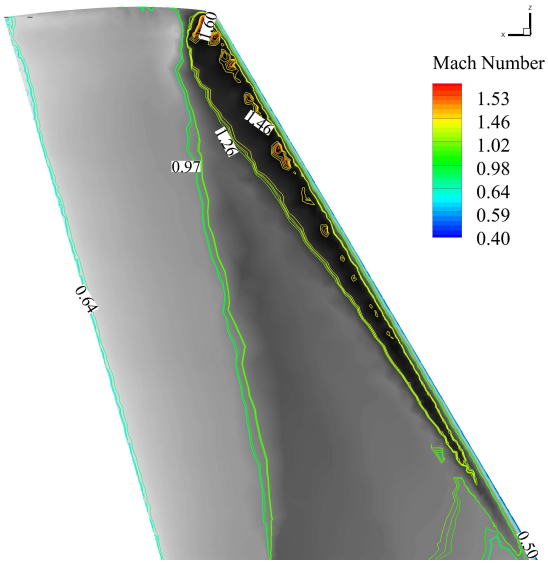

(a) Mach Number WE3

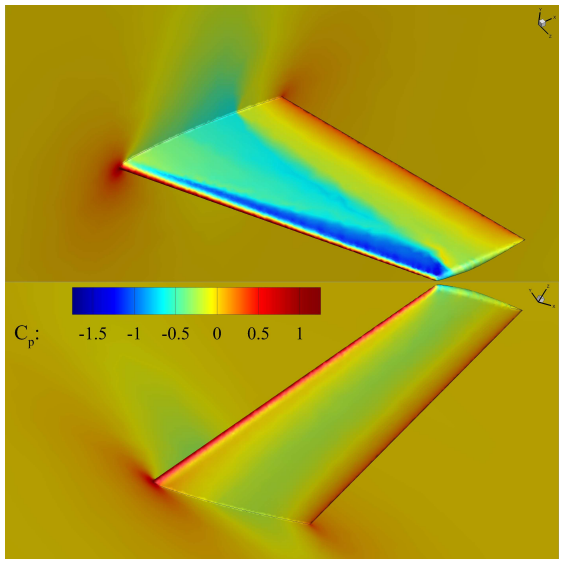

(b) C_p WE3

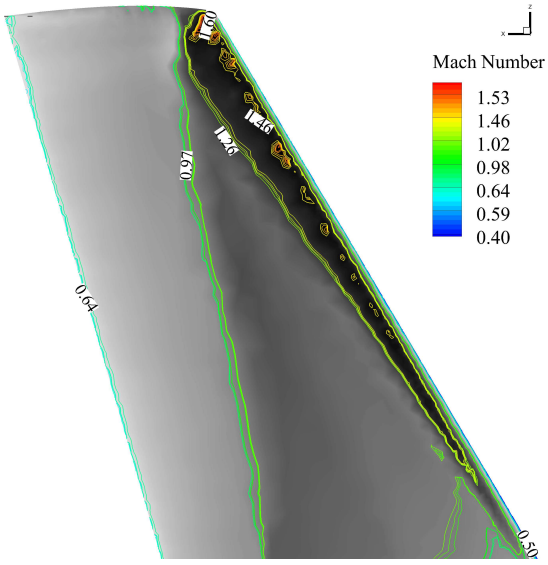

(c) Mach Number WE5

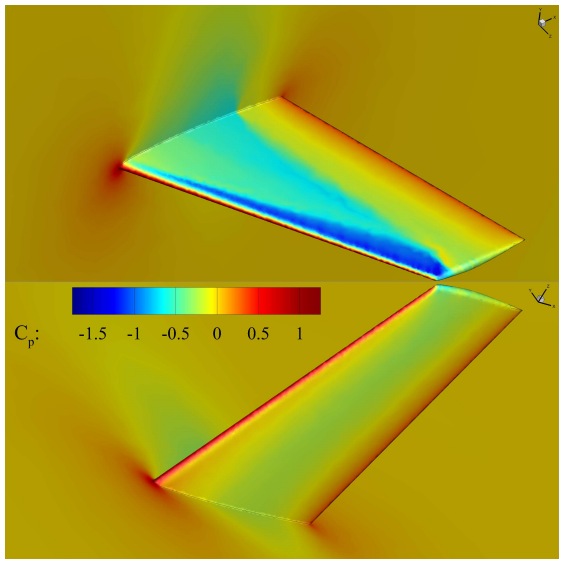

(d) C_p WE5

Figure 5.7: Computed Mach number contour lines and pressure coefficient contours for upper and lower wing sides; solutions shown for GRID-1 for 3^{rd} and 5^{th}-order WENO simulations ($M_\infty = 0.84$ and $a = 3.06°$).

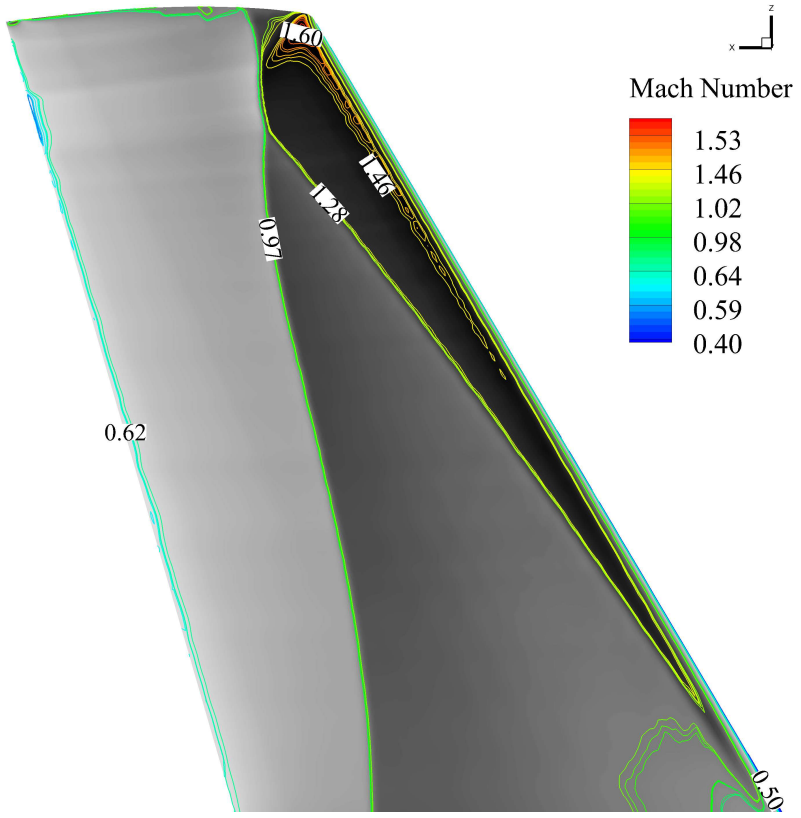

(a) Mach Number

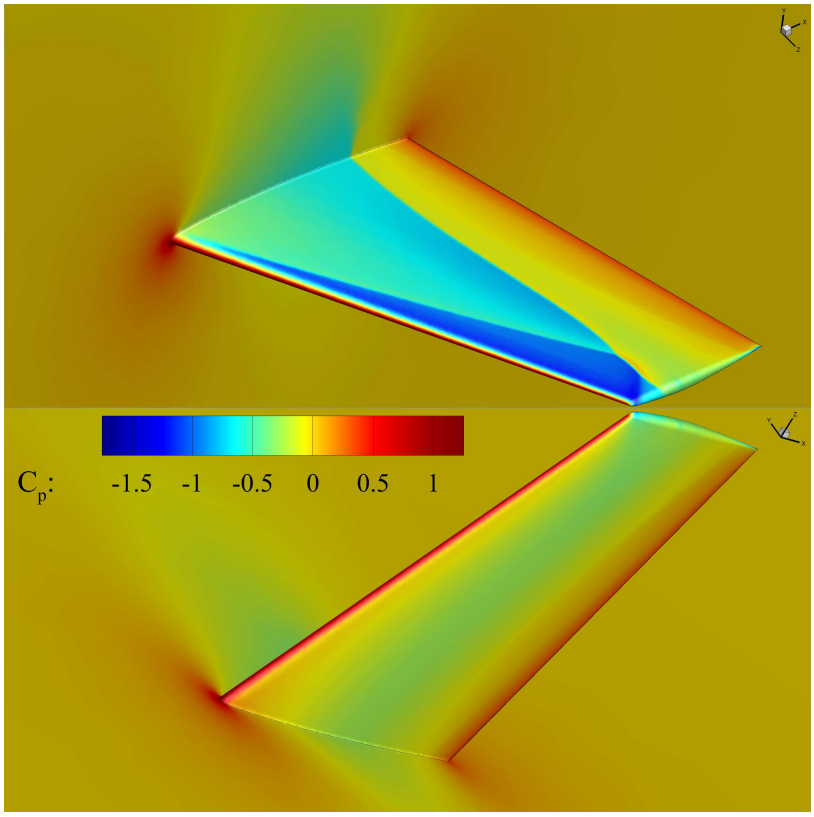

(b) C_p

Figure 5.8: Computed Mach number contour lines and pressure coefficient contours for upper and lower wing sides; solutions shown for GRID-2 with the 3^{rd}-order WENO scheme ($M_\infty = 0.84$ and $a = 3.06°$).

lower part of the wing, the C_p is reasonably computed, where either grid or polynomial refinement results in even better agreement with the experimental measurements.

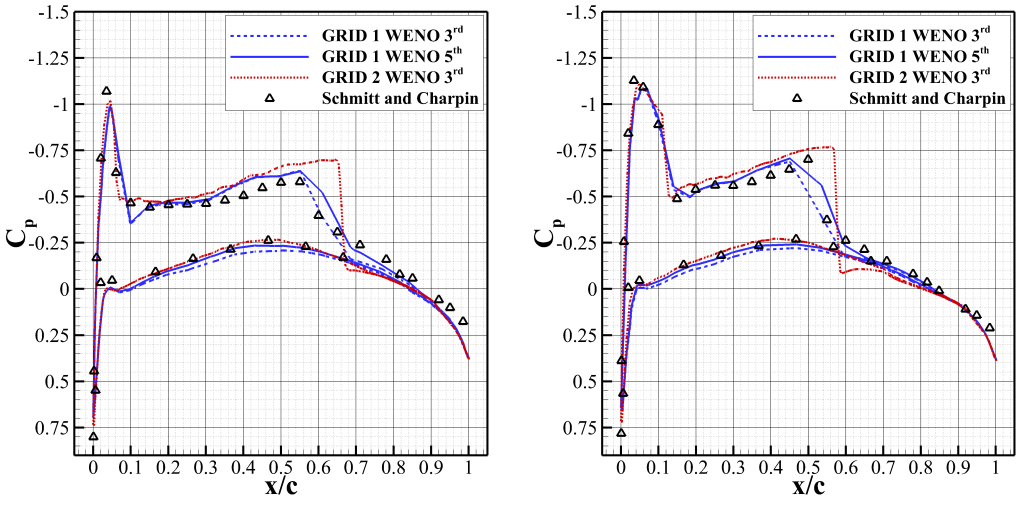

(a) z/b = 20%

(b) z/b = 44%

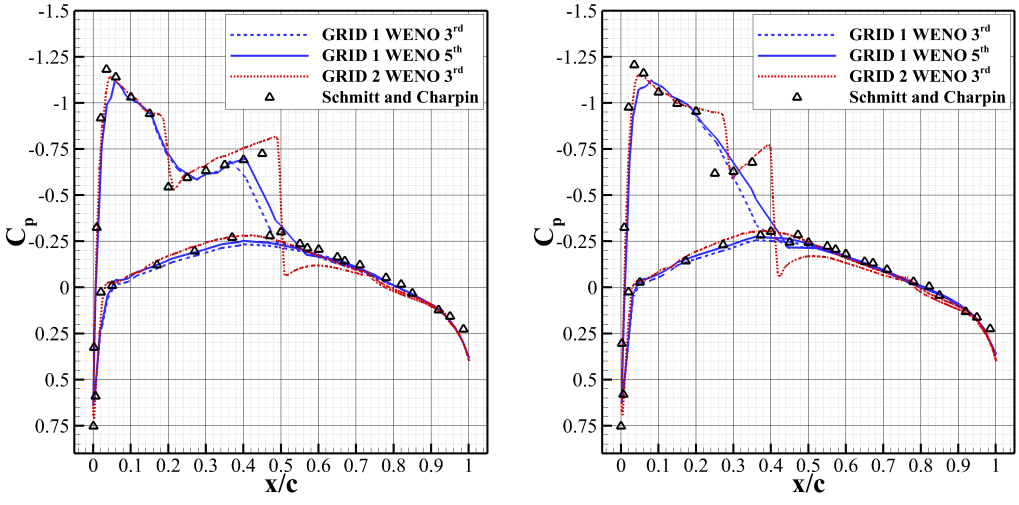

(c) z/b = 65%

(d) z/b = 80%

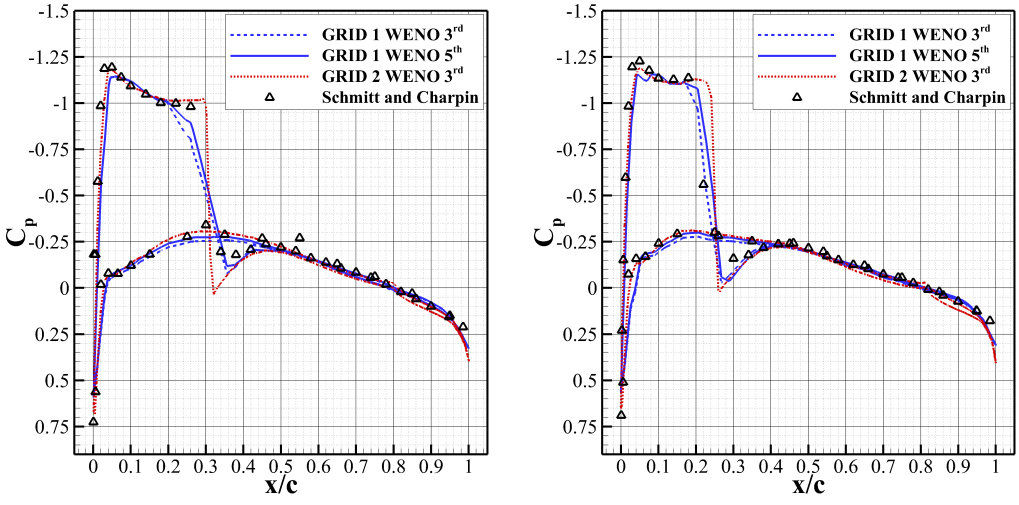

(e) z/b = 90%

(f) z/b = 95%

Figure 5.9: Computed pressure coefficient for 3^{rd} and 5^{th}-order WENO schemes for GRID 1 and 3^{rd}-order WENO scheme for GRID 2, compared with experimental data on six different span-wise stations (z/b) [174] ($M_\infty = 0.84$ and $a = 3.06°$).

CHAPTER 6

LAMINAR APPLICATIONS

This chapter is devoted to a series of applications for laminar flows. The cases under investigation are the 3D laminar flow over a flat plate, where different types and sizes of grids are employed and compared to the analytical solution. The subsonic flow over the NACA-0012 aerofoil is simulated at angle of attack $\alpha = 0°$ and at transonic conditions at $\alpha = 10°$. Laminar flows are often considered facile compared with turbulent, where unsteadiness and uncertainties are introduced into the physical system. However, there are several elusive aspects for laminar flows that several authors have studied [182, 183], therefore an extensive numerical analysis is conducted, including grid convergence studies, element-type dependencies, computational speed comparisons, performance assessment of the developed schemes in terms of accuracy and efficiency as well as boundary condition effects on the solution.

6.1 Flow over a Flat Plate

Analytical Solution

In 1908, H. Blasius and L. Prandtl obtained the first analytical solution of the Navier-Stokes equations [184] by transforming each PDE to a nonlinear ordinary differential equation (ODE) for a laminar flow over an infinite length flat plate [185]. As a matter of fact, the proposed solution is semi-analytical, by employing an independent variable transformation approach by introducing the traverse similarity variable η to converge only to a restricted region. Most recently, Liao introduced an explicit totally analytic approximate solution for the same problem using the Homotopy Analysis Method (HAM), non-perturbation technique [186], for further reading on analytical methods on laminar flows refer to the following publications [187–196].

Assuming a 2D, steady state, incompressible (ρ = constant), laminar flow, with zero pressure gradient $\partial p/\partial x = 0$ on the horizontal flat plate, meaning no streamline curvature $\partial p/\partial y = 0$, only diffusion in cross-stream, the fluid is considered to be Newtonian thus $\tau = \mu \partial u/\partial y$ described by the following equations in differential form of continuity and momentum respectively.

$$\frac{\partial u}{\partial x} + \frac{\partial v}{\partial y} = 0 \tag{6.1.1}$$

$$u\frac{\partial u}{\partial x} + v\frac{\partial u}{\partial y} = u_e\frac{du_e}{dx} + v\frac{\partial^2 u}{\partial y^2} \Rightarrow \rho\left(u\frac{\partial u}{\partial x} + v\frac{\partial v}{\partial y}\right) = \mu\frac{\partial^2 u}{\partial y^2} \tag{6.1.2}$$

where u and v are the velocity components in x and y respectively, u_e is the exit velocity and v the kinematic viscosity defined as $v = \mu/\rho$, μ the dynamic viscosity and ρ the density. With the following boundary conditions

$$u = v = 0 \text{ at } y = 0, \quad u = \mathrm{U}_\infty \text{ at } y = \infty. \tag{6.1.3}$$

The solution of parabolic equations (6.1.1) and (6.1.2) can be performed progressively, hence they are independent of the length scale x, this suggests that

$$Re_x = \frac{U_x}{\mu} \tag{6.1.4}$$

Blasius proposed to solve the system of equations (6.1.1) and (6.1.2) in a way that the normalized velocity profile by the freestream velocity u/U_∞ should be similar for all x values on the wall against the nondimensional distance y from the wall, thus the above relation states also that u/U_∞ can be written in terms of a dimensionless similarity variable η as follow

$$\eta = \frac{y}{x}\sqrt{Re_x} = \frac{y}{x}\sqrt{\left(\frac{u_e x}{\mu}\right)}. \tag{6.1.5}$$

A new variable is introduced ξ, which expresses the governing equations in terms of a stream function ψ; for the complete derivation see [197]. By applying the boundary conditions to the stream function and numerically calculate its derivatives, the momentum equation (6.1.2) reduces to an ODE as η being the only independent variable; the coefficient of friction C_f can be calculated as

$$C_f = \mu U_\infty a \sqrt{\frac{U_\infty}{2\mu x}} = \frac{0.664}{\sqrt{Re}_x} \tag{6.1.6}$$

where $a = 0.4696$ is the constant of integration, the boundary layer displacement thickness δ is given as

$$\delta = 1.721\sqrt{\frac{\mu x}{U_\infty}}. \tag{6.1.7}$$

Computed Solutions

The laminar flow over a semi-infinite flat plate is simulated at a free-stream Mach number of $M_\infty = 0.5$, a Reynolds number of $Re = 10,000$ and a Prandtl number of $P_r = 0.72$. Two element-type of grids are considered, which defer with respect to the type of elements resolving the boundary layer region, i.e. prisms or hexahedral. Each hexahedral is split into two prisms to generate the prismatic grids, the grid parameters are shown in Table 6.1 on page 79 and in Figure 6.1 on page 78 illustrates the computational grids. All grids for this case were generated with the Pointwise® [80] software.

Two schemes are employed for the considered computations, the 3^{rd}-order MUSCL-TVD and the 3^{rd}-order WENO schemes, for time discretisation the 3^{rd}-order Runge-Kutta algorithm is employed with a CFL of 0.4. No-slip adiabatic wall condition is set

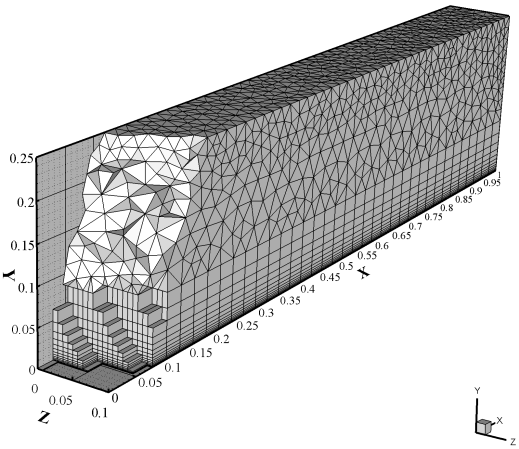

(a) Coarse hexahedral-based grid

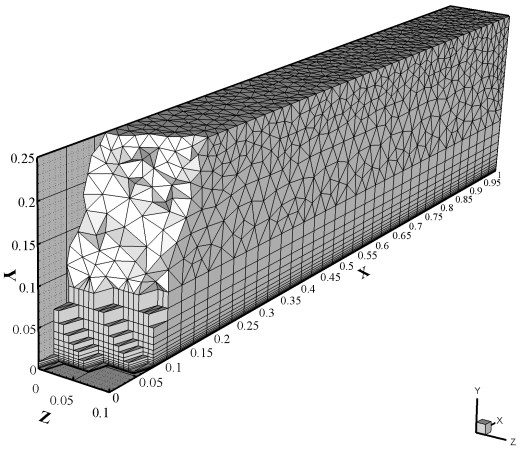

(b) Coarse prismatic-based grid

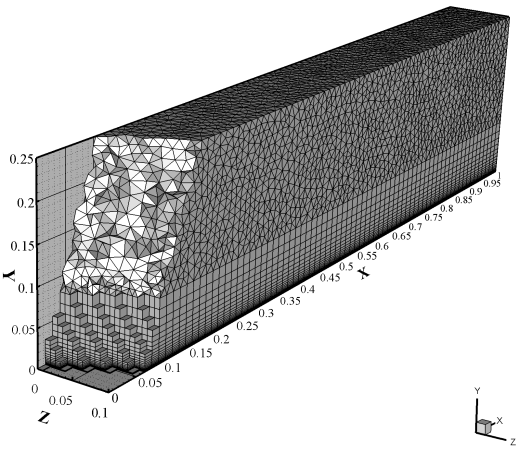

(c) Medium hexahedral-based grid

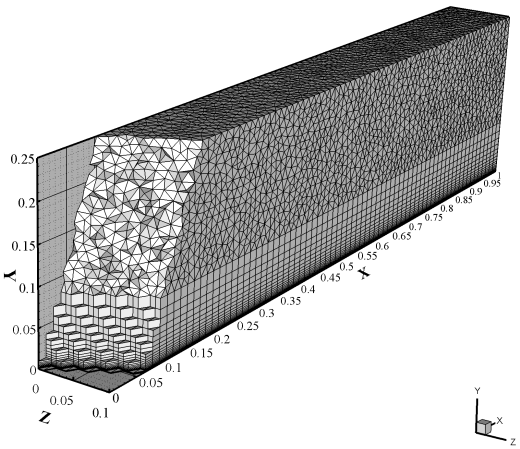

(d) Medium prismatic-based grid

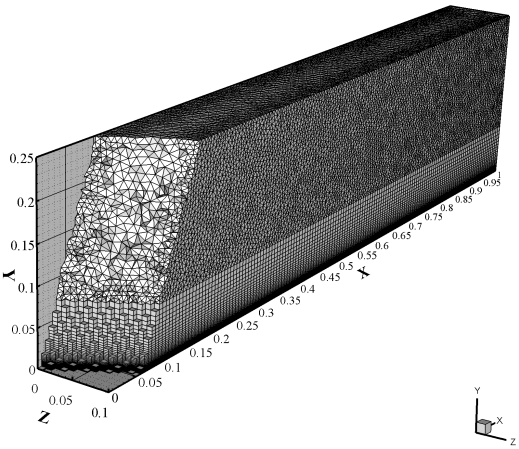

(e) Fine hexahedral-based grid

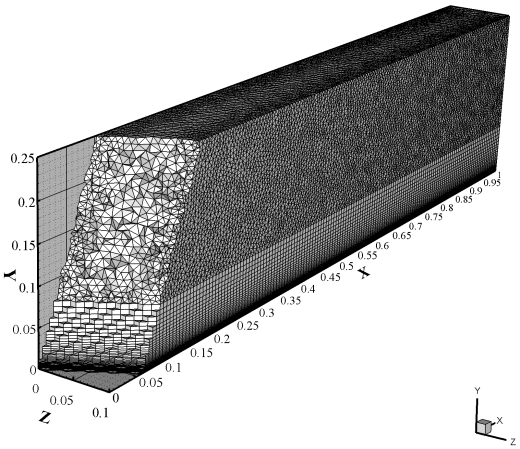

(f) Fine prismatic-based grid

Figure 6.1: Mixed-element grids employed for the laminar flow over a flat plate.

for the plate, where characteristic boundary conditions (subsonic) were enforced on the outer boundaries with symmetry condition imposed on both span-wise surfaces. The objectives of this test case are summarized:

- validate the developed viscous discretisation methods including: gradient reconstruction and wall-boundary treatment for 3D laminar boundary layer flow
- assess the accuracy of the computed solutions for the employed schemes against the analytical solution
- perform grid convergence and assess the performance of element types
- analyse the computational performance of developed schemes for 3D wall-bounded viscous flows

Table 6.1: Parameters for the prismatic and hexahedral based grids employed for the laminar flow over a flat plate

Grid	Nodes	Elements	Hexahedra	Tetrahedra	Pyramids	Prisms
Coarse	12,074	31,311	-	15,771	-	15,540
Medium	40,542	121,396	-	73,096	-	48,300
Fine	148,602	443,584	-	261,780	-	181,804
Coarse	12,614	26,036	7,770	17,748	518	-
Medium	39,916	92,110	24,150	66,910	1,050	-
Fine	153,956	382,948	90,902	289,932	2,114	-

The similarity variable η and the coefficient of friction C_f are the two variables employed to assess the accuracy of the simulations with respect to the semi-analytical solution of Blasius. For η a single cut-section is employed at the end of the plate, corresponding to the highest local Reynolds number. For the C_f a mid-cut-section of the z axis is used in order to elude any numerical artifacts from the symmetric boundary conditions. The results are plotted on logarithmic scales for both variables to enable a better overview of the dissemblances and to conduct a thorough comparison.

In Figure 6.2 on page 80 the solutions of all grids computed with the WENO 3^{rd}-order scheme are plotted in terms of η and C_f; differences between the prismatic and

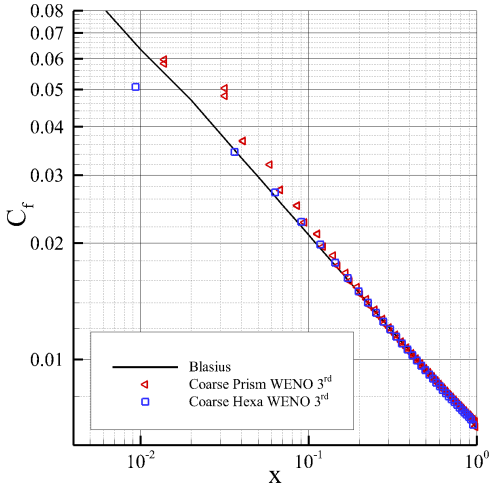

(a) C_f for the coarse grids

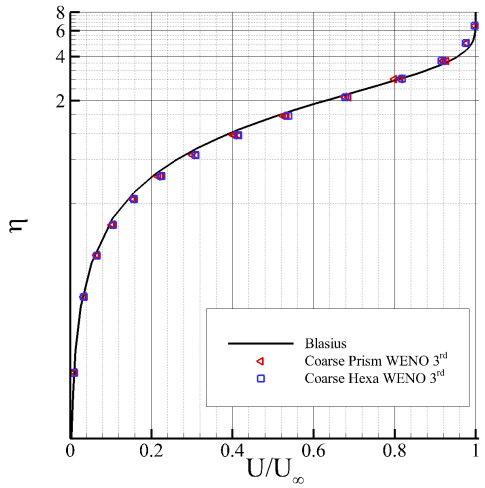

(b) η for the coarse grids

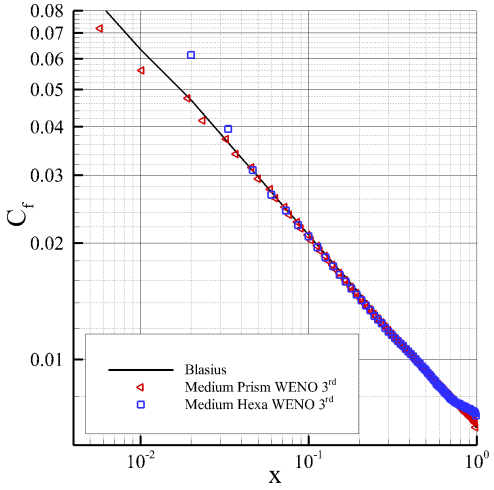

(c) C_f for the medium grids

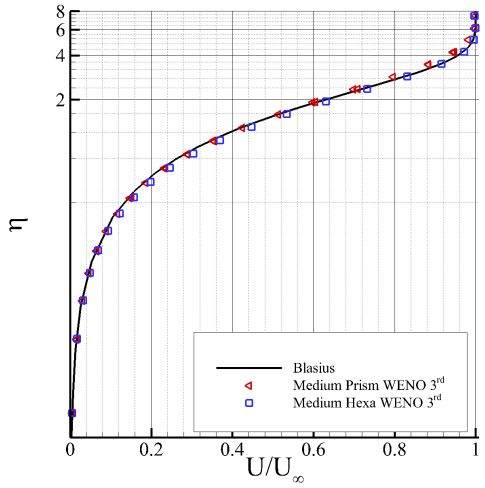

(d) η for the medium grids

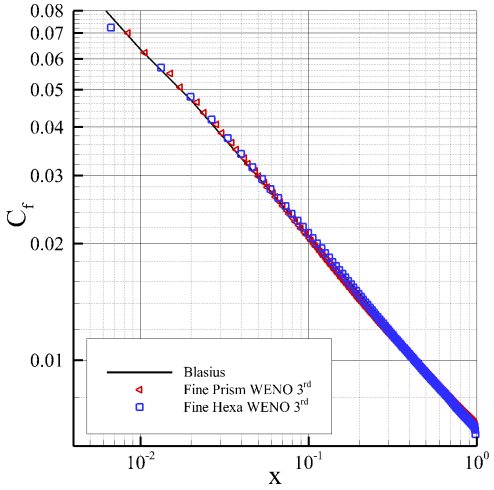

(e) C_f for the fine grids

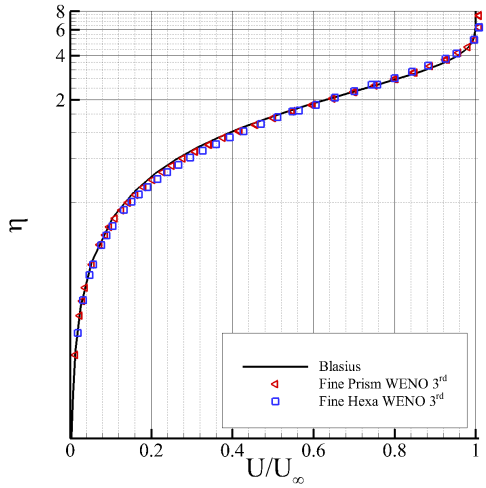

(f) η for the fine grids

Figure 6.2: Comparison of computed solutions with WENO 3^{rd}-order scheme on hexahedral and prismatic based grids for skin friction coefficient (C_f) and the similarity variable (η) against Blasius semi-analytical solution ($M_\infty = 0.5$ and $Re = 10,000$).

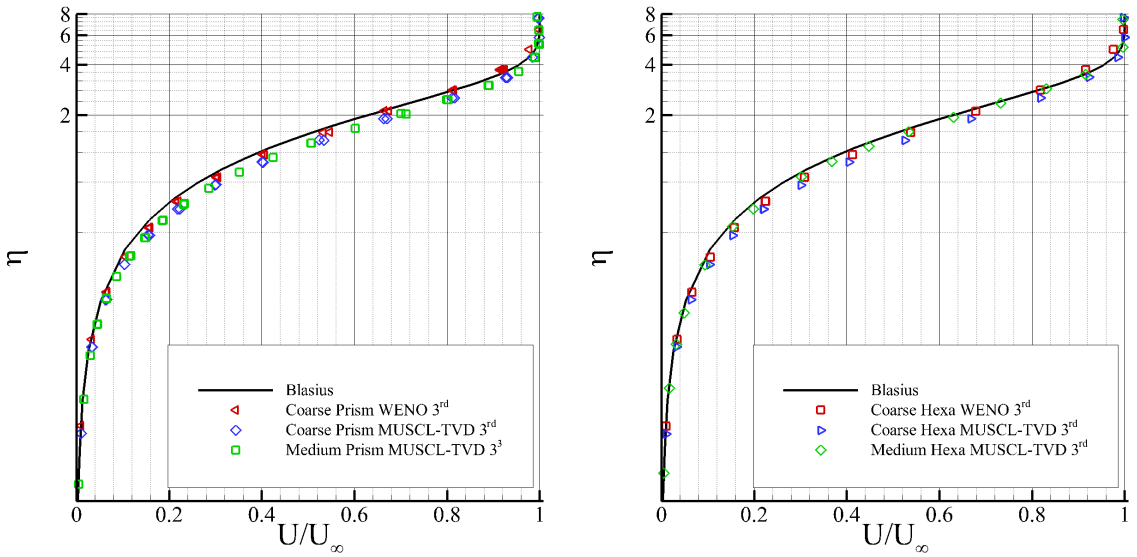

(a) Prismatic grids (b) Hexahedral grids

Figure 6.3: Comparison of computed solutions for the MUSCL-TVD 3^{rd} and WENO 3^{rd}-order schemes on prismatic and hexahedral based grids, similarity variable η against normalised velocity U/U_∞ ($M_\infty = 0.5$ and $Re = 10,000$).

hexahedral based grids for η are difficult to notice, however, when observed closely it seems that the hexahedral captures the parabolic profile of the laminar boundary layer more precisely. The improved performance of the hexahedral grid for η, observed for the coarse and medium grids, stems from the actual construction of the WENO directional stencils. Since, the relatively skewer prisms compose a more compact and disproportionate stencil compared to the hexahedra stencils see in 3.6 and 3.7. Moreover, for the same order of accuracy, the hexahedral employs 50% more Gaussian quadrature integration points on the bounded faces resulting to a more accurate flux evaluation. The small discrepancy for the medium hexahedral in Figure 6.2 on page 80 (c) in the vicinity of the outflow boundary can be attributed to the unfortunate drop of order of accuracy on the boundary itself; this adverse effect on the solution from the outflow boundary, for the laminar flow over a flat plate with high-order upwind schemes is also reported by Drikakis and Tsangaris [198].

The coefficient of friction is also plotted where discrepancies are observed at the singularity point near the leading edge of the flat plate suggesting that the uniform velocity profile of the subsonic inflow boundary has an adverse effect on the reconstruction of the gradients on the wall further agitating the flow downstream, this is also observed by Haselbacher and Blazek [140]. The largest discrepancies appear in

this region for both type of grids, either over or under predicting the value of C_f. By refining the grid the discrepancies considerably decrease. Furthermore, the prismatic grids are in better agreement with Blasius solution, this stems from the fact that the skin friction is computed on the wall, and since the least-square reconstruction employs one point on the wall-bounded face and the prismatic grids have double the number of elements compared with the hexahedral-based grid, they are able to resolve better the wall shear stresses.

As expected, the performance of the MUSCL-TVD is inferior for the same grid for both hexahedral and prismatic compared with the WENO solution, elaborated in Figures 6.3. The plot also suggests, that h-refinement with the prismatic grid is unable to reach the agreement of the WENO predictions with the coarse, furthermore for the hexahedral case, grid refinement and switching from MUSCL-TVD to WENO seems to have an identical agreement.

From the grid convergence study it has been demonstrated that the numerical behaviour of the WENO-3^{rd} scheme for both prismatic and hexahedral base grids converged towards Blasius solution as the grid is further refined, illustrated in figures Figure 6.4 on page 83. The grid convergence is more noticeable for the C_f estimations as both axes are on a logarithmic scale, amplifying the distinctnesses of each solution.

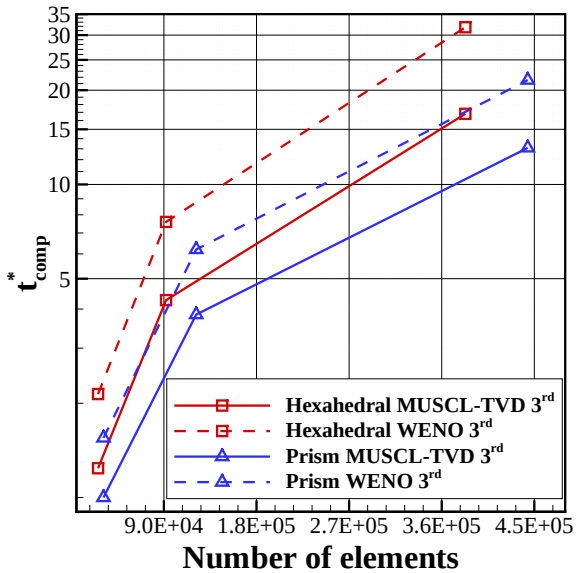

Figure 6.5: Normalised computational times for the MUSCL-TVD and WENO schemes against number of elements for the laminar flow over a flat plate ($M_\infty = 0.5$ and $Re = 10,000$).

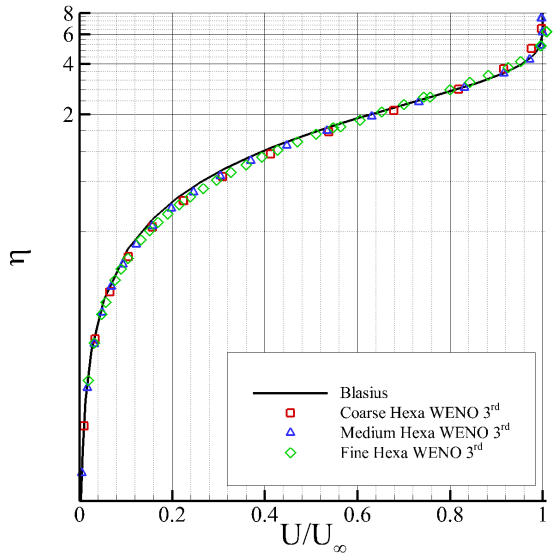

(a) η for hexahedral grids

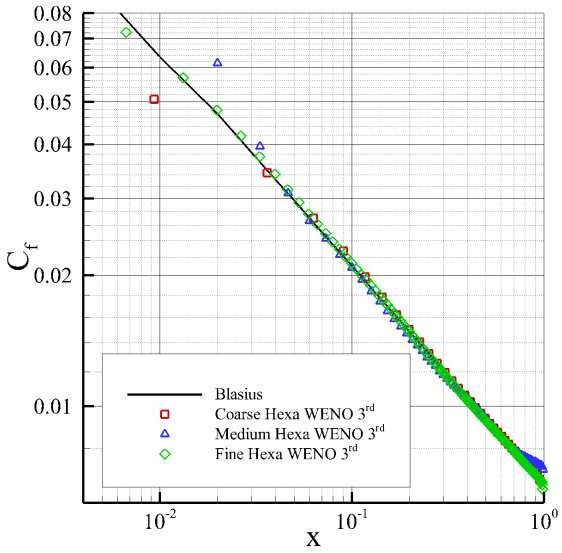

(b) C_f for hexahedral grids

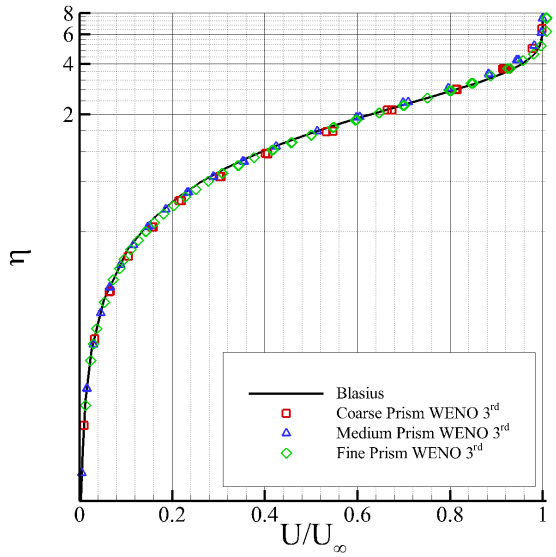

(c) η for prismatic grids

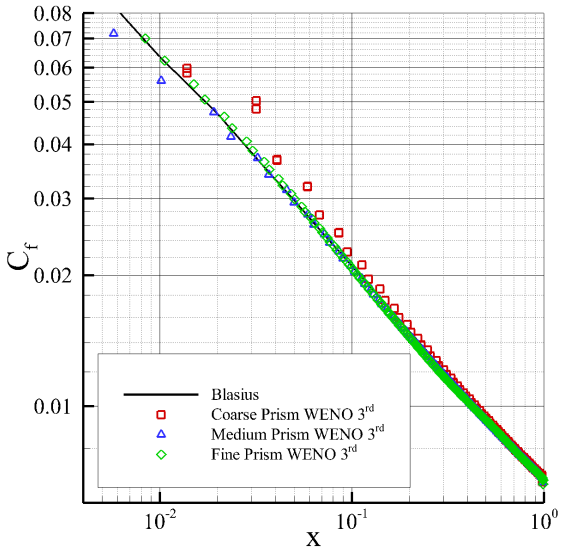

(d) C_f for prismatic grids

Figure 6.4: Grid convergence for the computed solutions with the WENO 3^{rd}-order scheme for the hexahedral and prismatic grids, results shown for the similarity variable η and the coefficient of friction C_f ($M_\infty = 0.5$ and $Re = 10,000$).

The computational efficiency of each algorithm is determined by the time required for each scheme to perform one Runge-Kutta stage, incorporating the time required to perform the computations at each processor i.e. reconstruction and evaluation of fluxes, as well as the time spend for sending and receiving data from other processors through the MPI protocol. Figure 6.5 on page 82 shows the normalised computational times for MUSCL-TVD and WENO simulations for hexahedral and prismatic grids; the computational times are normalised based on the fastest simulation. The hexahedral-based grids are more expensive than the prismatic for the same number of elements for both schemes. Furthermore, the computational efficiency for the hexahedral MUSCL-TVD is very close to the prismatic WENO at $\approx 100,000$. In terms of accuracy it can be depicted from Figure 6.3 on page 81 (b) and Figure 6.4 on page 83 (c) that the medium prismatic WENO 3^{rd}-order results are in better agreement with Blasius solution for η than the medium hexahedral MUSCL-TVD 3^{rd}-order. Without loss of generality, this suggests that WENO schemes inheriting a higher accuracy for smooth problems and depending upon the grid selection, can in fact be more cost-efficient than MUSCL-TVD schemes.

6.2 Subsonic Flow past the NACA-0012 Aerofoil

The laminar flow over the symmetric NACA-0012 aerofoil is simulated at subsonic conditions at a Mach number of $M_\infty = 0.3$, a zero angle of attack $\alpha = 0°$, at a moderate Reynolds number of $Re = 5,000$ based on the aerofoil's chord length and a Prandtl number of $P_r = 1$. This laminar flow past the aerofoil at zero angle incident will theoretically produce zero lift and the relatively thick boundary layers will remain attached to the aerofoil surface. The simulations look at evaluating the accuracy of each scheme on an under-resolved grid composed of $6,568$ nodes and $9,006$ elements, from which $3,840$ are quadrilaterals and $5,166$ are triangles, the far field is located at $[-3 \leq x \leq 4]x[-3 \leq y \leq 3]$; Figure 6.6 on page 85 (a) illustrates a section of the grid near the aerofoil. Three numerical schemes were employed for the considered flow problem, the MUSCL-TVD 3^{rd}, the WENO 3^{rd} and WENO 5^{th}-order schemes. The 3^{rd}-order Runge-Kutta time discretisation was used with a CFL number of 0.3 for all simulations. The computations run until the forces naming the coefficient of drag and lift stabilize. The main objectives of this test case are summarised:

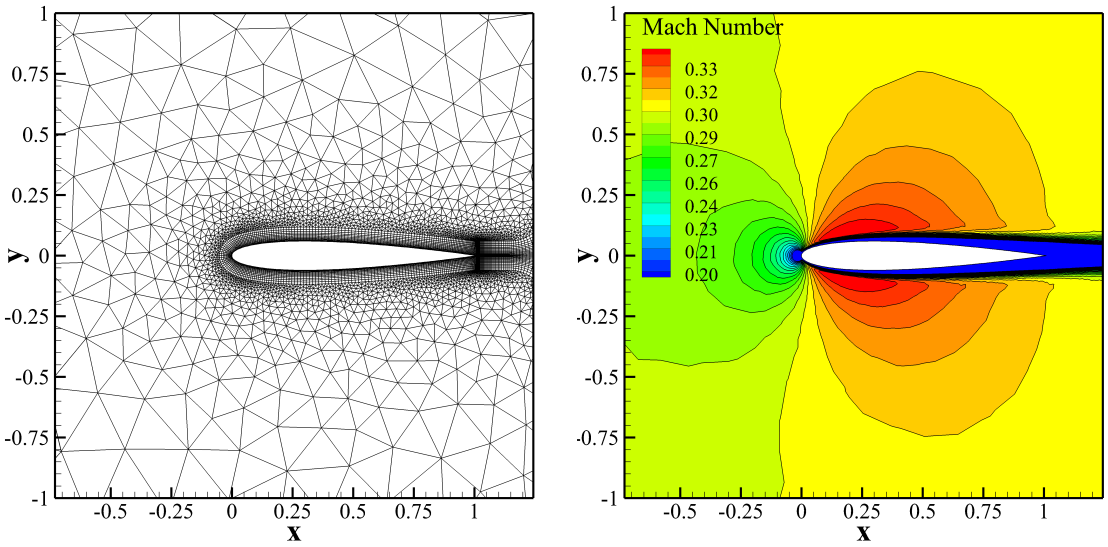

(a) Grid (b) Mach number with WE3

Figure 6.6: Computational grid and Mach number contour plots for the laminar flow past the NACA-0012 aerofoil, with the WENO 3^{rd}-order scheme $(\alpha = 0°, Re : 5,000, M_\infty = 0.3)$.

- validate the implementation of viscous discretisation and gradient reconstruction for two dimensional external laminar flows
- assess the accuracy and performance of the developed scheme on curved wall boundaries

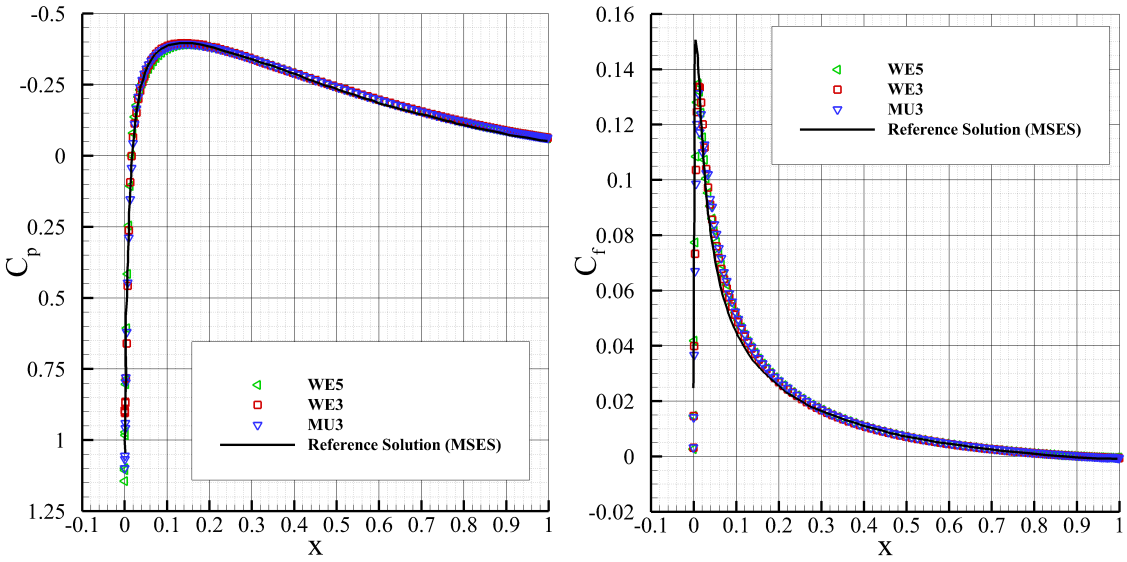

(a) C_p (b) C_f

Figure 6.7: Pressure coefficient (C_p) and skin friction coefficient (C_f) for the laminar flow past the NACA-0012 aerofoil, comparison between MUSCL-TVD 3^{rd}, WENO 3^{rd}, WENO 5^{th}-order schemes and reference solution MSES [126] ($\alpha = 0°, Re : 5,000, M_\infty = 0.3$).

The numerical results are compared with a reliable reference solution from the CFD software MSES [199], data is available for the pressure coefficient C_p and the skin friction coefficient C_f in Figure 6.7 on page 86. For the pressure distribution, the agreement between all employed schemes and the reference solution is very good, small variations are noticeable for the skin friction coefficient, where the WE3 and WE5 schemes predicted a higher spike at the leading edge of the aerofoil, converging towards the reference solution. From the coefficient of lift and drag time evolutions shown in Figure 6.8 on page 87 it is depicted that the increase of the polynomial's order will produce certain oscillations particularly for WE5. This can be attributed to the inherited smaller dissipation error and larger dispersion effects of the scheme in turns associated with the larger stencils covering a wider area; shown in Figure 6.9 on page 87 for WE3 and WE5.

Furthermore, the natural curvature of the aerofoil surface line, feeds the dynamic of the flow for well-resolved simulation to develop vortical structures in the wake as presented in [200] using a DG spectral (h/p) method in three spatial dimensions. The third dimension is fundamental for resolving vortex shedding dominant flows, this requirement is also exemplified with the classical case of the laminar flow past

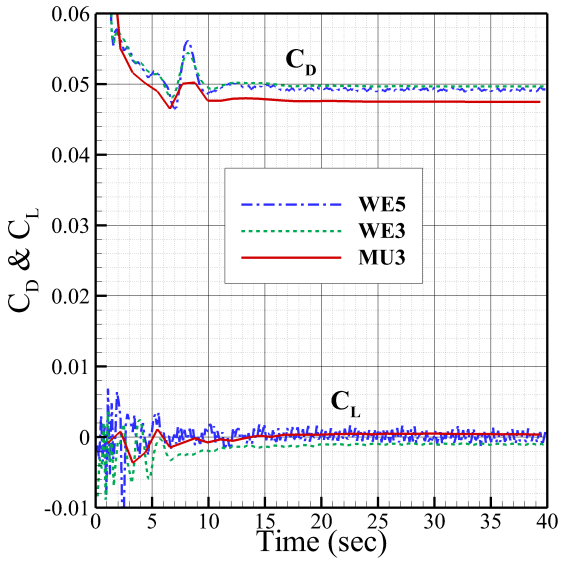

Figure 6.8: Lift coefficient (C_L) and drag coefficient (C_D) convergence histories for the laminar flow over the NACA-0012 aerofoil, for MUSCL-TVD 3^{rd}, WENO 3^{rd}, WENO 5^{th}-order schemes, $(\alpha = 0°, Re : 5,000, M_\infty = 0.3)$.

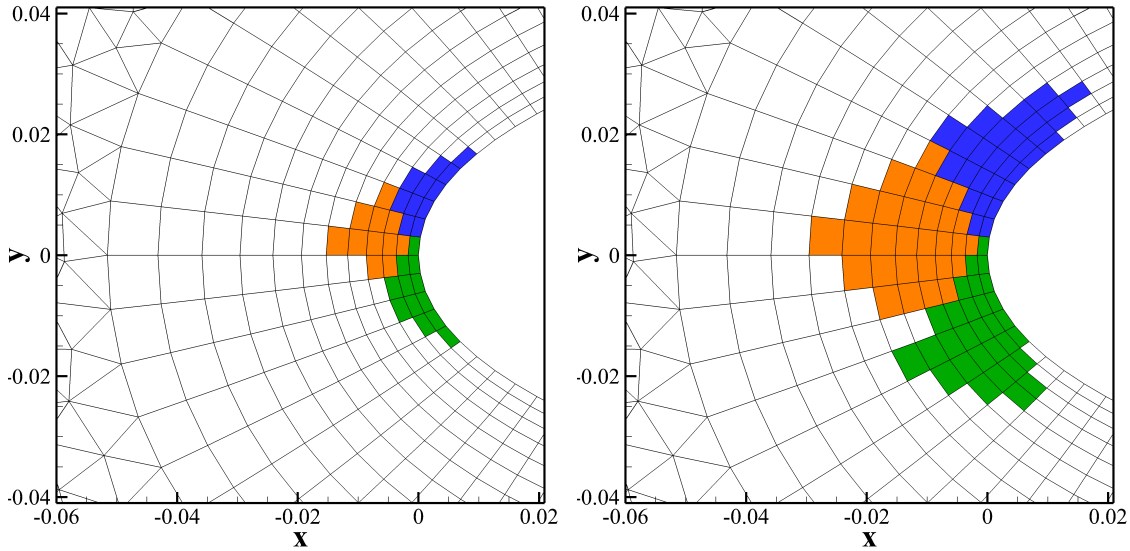

(a) WE3 (b) WE5

Figure 6.9: Directional stencils for the WENO 3^{rd} and WENO 5^{th}-order schemes near the stagnation point of the NACA-0012 aerofoil.

a cylinder, where even with a well refined spatial grid in two dimensions, the flow is characterised by irregularities and asymmetric behaviour in the vortex street illustrated with instantaneous Mach number contours in Figure 6.11 on page 89. This peculiar behaviour is also reported by Breuer [201] and can have an adverse aftermath on the prediction of the forces on the aerofoil, where non-zero mean lift coefficients are often encountered.

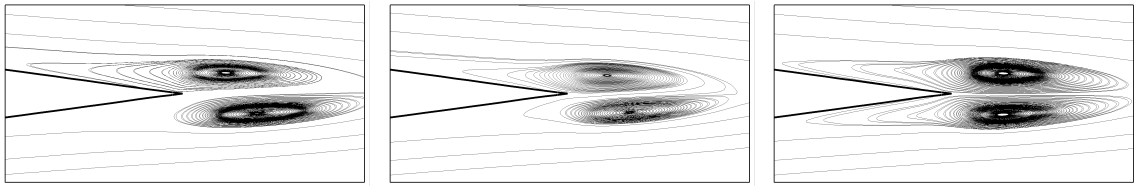

(a) MU3 (b) WE3 (c) WE5

Figure 6.10: Stream-lines near the trailing edge of aerofoil showing the double vortex structure; for the MUSCL-TVD 3^{rd}, WENO 3^{rd} and WENO 5^{th}-order schemes, $(\alpha = 0°, Re = 5,000, M_\infty = 0.3)$.

It has to be noted, that the total mean lift error with the employment of WE5 scheme decreases approximately one order of magnitude compared with both MU3 and WE3 lift predictions. This improvement is also mirrored in Figures 6.10 showing the flow pattern with stream-lines (same location is used for all figures) of the flow in the vicinity of the trailing edge, where the counter rotating vortex pair have a more symmetrical structure with the WE5 scheme and remain noticeably attached to the aerofoil surface. This symmetrical structure of the vortex pair with high-order schemes employing a fine grid is also reported by Chassaing et al. [202].

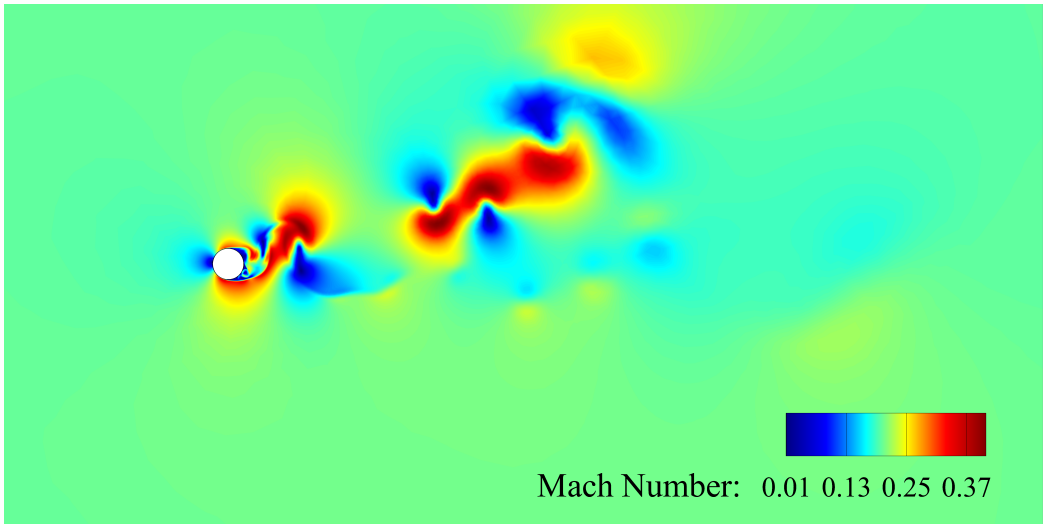

Figure 6.11: Mach number contours for the flow past a cylinder in 2D with the WENO 3^{rd}-order scheme, demonstrating an irregular evolution of the vortex street ($Re = 3,900, M_\infty = 0.2$ with 171,480 elements).

6.3 Transonic Flow past the NACA-0012 Aerofoil

The third case considered is the laminar flow past the NACA-0012 aerofoil, at a chord-based Reynolds of $Re = 500$, an angle of attack of $\alpha = 10°$, at transonic conditions where the Mach number is $M_\infty = 0.8$ and a Prandlt number of $P_r = 0.7$. This test case originally conducted for the GAMM workshop [182] has been extensively employed for validation purposes [203, 204]. At these conditions, viscous effects are dominant where the upper surface exhibits a boundary layer separation creating a large bubble, the flow reattaches at the tip of the trailing edge, while on the lower part of the aerofoil the flow remains attached along its length.

Grid convergence and element-type dependencies are conducted, thus three triangular and three quadrilateral grids are generated corresponding to coarse, medium and fine; grid parameters are tabulated in table Table 6.2 on page 90, where the refinement for each stage follows the rule of doubling the number of nodes on the aerofoil surface and halves the height of the first element from the wall. The grid generation procedure starts with the construction of the quadrilateral grids, then each quadrilateral is split into two triangles to create the triangular grids.

Table 6.2: Grid statistics for the transonic laminar flow over the NACA-0012 aerofoil

	Nodes	Triangles	Quadrilaterals	Nodes on aerofoil
Coarse	3,658	3,599	7,198	60
Medium	5,683	8,591	17,182	120
Fine	13,773	18,375	36,750	240

In contrast to the previous test case, where the angle of attack is zero and a C-type grid was employed as it is more in tune with the flow structure where all flow gradients are concentrated along the horizontal axis behind the trailing edge, for the subject case at $\alpha = 10^{\circ}$ the O-type grid is more congruous, capturing better the wake formation on a smoother mesh. Moreover, O-grid have superior characteristics over C-type for high angles of attack as the gradient of the transformation of the metrics is much smoother, and avoids the utterly skewed elements at the vertical axis near the trailing edge, leading to better convergence and C_l predictions [205]. The far field is located at 400 chord lengths away from the aerofoil, the effects of the far field on the solution are studied by altering the location of the outer boundary.

The MUSCL-TVD 3^{rd} and WENO 3^{rd}-order schemes were utilized for the spatial discretisation, where time advancement was achieved with the 3^{rd}-order Runge-Kutta algorithm with a CFL number of 0.3 for all simulations. Summarising the objectives of this case:

- validate the developed numerical schemes for laminar flows with boundary layer separation phenomena
- assess the performance of triangular and quadrilateral grids with MUSCL-TVD and WENO schemes
- perform grid convergence study and assess the performance of the high-order schemes for 2D highly viscous flows
- analyse the predicted forces by altering the location of the far field with respect to the numerical scheme

Since experimental data are unavailable for the subject case, the performance of the schemes is demonstrated through a grid-refinement study by analysing the

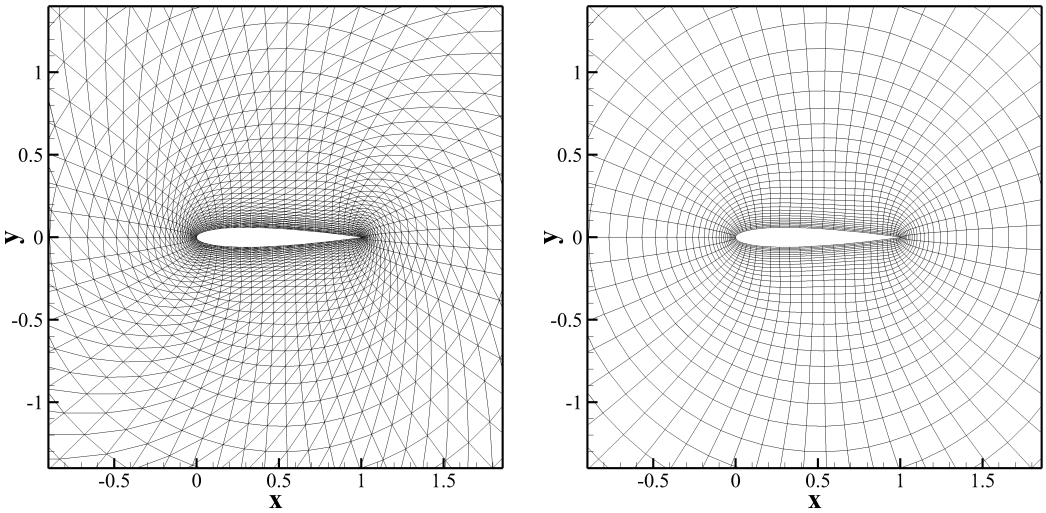

(a) Coarse triangular

(b) Coarse quadrilateral

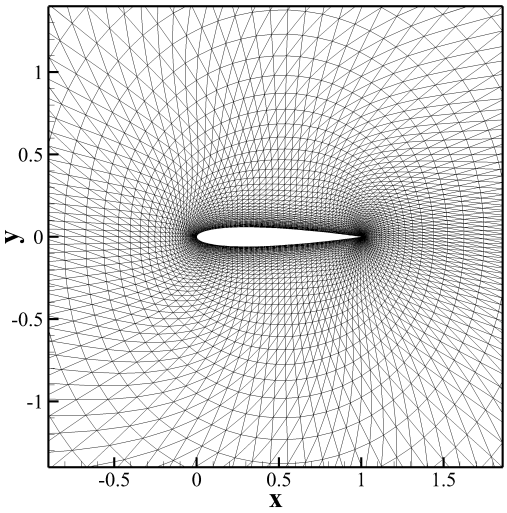

(c) Medium triangular

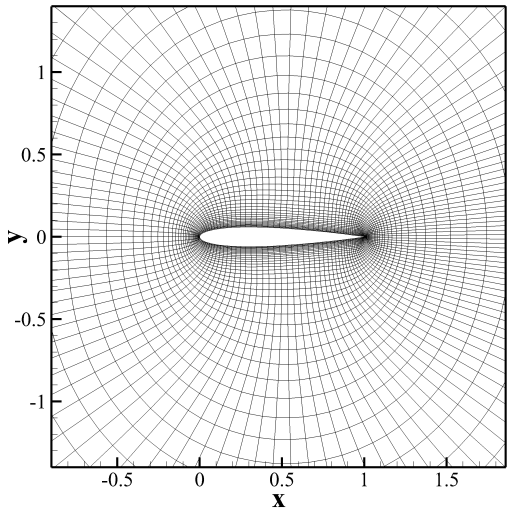

(d) Medium quadrilateral

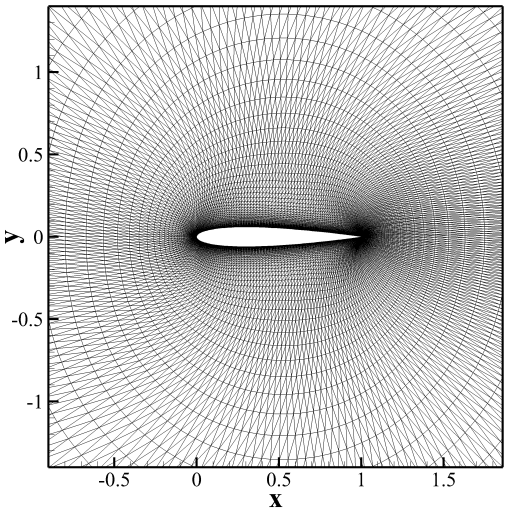

(e) Fine triangular

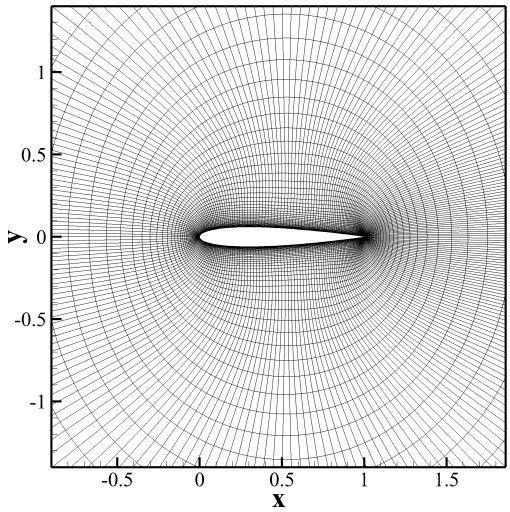

(f) Fine quadrilateral

Figure 6.12: Spatial grids employed for the transonic laminar flow past the NACA-0012 aerofoil $(\alpha = 10^{\circ}, Re : 500, M_{\infty} = 0.8)$.

Table 6.3: Lift and drag predictions for the transonic laminar flow past the NACA-0012 aerofoil

Quadrilateral Grids	C_L	C_D	C_{Df}	C_{Dp}
Coarse MU3	0.4873	0.2823	0.1165	0.1657
Medium MU3	0.4344	0.2596	0.1096	0.1499
Fine MU3	0.4307	0.2579	0.1090	0.1488
Coarse WE3	0.4799	0.2802	0.1144	0.1657
Medium WE3	0.4386	0.2606	0.1090	0.1515
Fine WE3	0.4342	0.2593	0.1091	0.1501
Triangular Grids	C_L	C_D	C_{Df}	C_{Dp}
Coarse MU3	0.4693	0.2728	0.1147	0.1580
Medium MU3	0.4363	0.2576	0.1094	0.1481
Fine MU3	0.4366	0.2590	0.1088	0.1502
Coarse WE3	0.4637	0.2700	0.1126	0.1574
Medium WE3	0.4359	0.2573	0.1086	0.1486
Fine WE3	0.4361	0.2588	0.1089	0.1499

coefficients of drag, lift and pressure. From Table 6.3 on page 92 it is depicted that the difference of the predicted drag coefficient (C_D) and lift coefficient (C_L) between the coarse and medium grids for both schemes and element types is considerably greater than that between the medium and fine. A strict grid-independent solution has not been reached, since the values are not identical; however, with differences occurring in the third decimal digit it can be deduced that the medium and fine grids are very close to the grid-independent solution. Furthermore, the convergence of the triangular grids is not monotone; this has also been observed by Zingg et al. [206], thus it is not related to the employed method.

The flow is dominated by strong viscous forces since the small Reynolds number ($Re : 500$) results in large viscosity. The highly physical diffusion in the flow results in a stable flow field demonstrated through the friction drag coefficient Figure 6.13 on page 93, where differences between grids and schemes are imperceptible. The pressure drag contributions show certain variations for the coarser grids attributed to the flight envelope of the test case, where the angle of attack affects the pressure gradients in the separation region. This is also reflected through the double vortex visualization near the wake of the aerofoil; Figure 6.14 on page 95 shows the computed Mach number contours and stream-lines for all employed grids and schemes. Grid

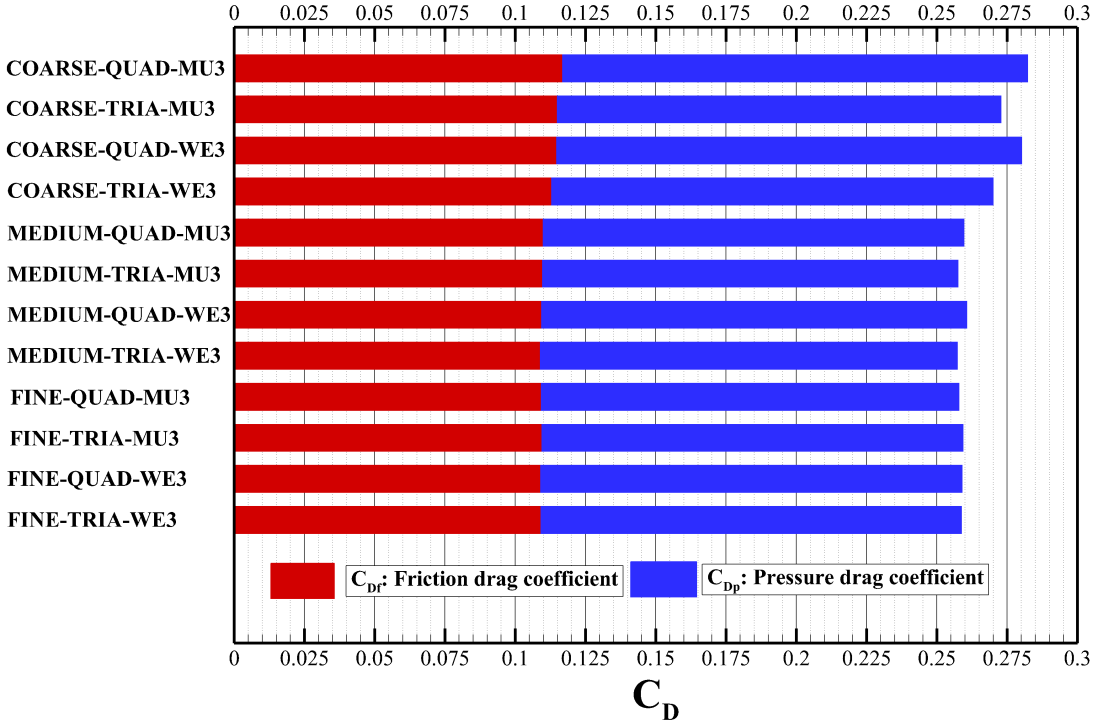

Figure 6.13: Friction drag (C_{Df}) and pressure drag (C_{Dp}) coefficients for the MUSCL-TVD 3^{rd} and WENO 3^{rd}-order schemes; QUAD is the quadrilateral and TRIA the triangular grids ($\alpha = 10°, Re : 500, M_\infty = 0.8$).

dependency ramifications can be depicted effortlessly; grid refinement results in an increase in the wake's length, again greatest disagreement occur between the coarse and medium cases where the vortex structure and intensity are mispredicted.

Variations related to the numerical schemes emerge for the coefficient of pressure (C_p) plots in Figure 6.15 on page 96 for the upper and lower part of the aerofoil. The coarse grids have a large adverse pressure gradient as previously established, nonetheless, both WENO triangular and quadrilateral results are considerably in better agreement than the MUSCL-TVD, converging towards the ostensible grid-independent solutions. For the medium and fine grids it seems that both MUSCL-TVD and WENO results are in accordance. The triangular grids, having double the number of elements, capture better the pressure drop on the upper side and the pressure rise on the lower side of the aerofoil's trailing edge.

Table 6.4: Lift and drag coefficient predictions for three far field locations at $25c$, $100c$ and $400c$ (aerofoil chord) on the quadrilateral medium grid for the MUSCL-TVD 3^{rd} and WENO 3^{rd}-order schemes

	MU3		WE3	
Grid based on c units	C_L	C_D	C_L	C_D
25	0.434400	0.259612	0.438927	0.261001
100	0.434420	0.259624	0.439874	0.261120
400	0.434416	0.259621	0.438615	0.260619

The effect of the far field is studied by altering the outer boundary at $25c$ and $100c$ aerofoil chord lengths for the quadrilateral medium grid. Both MUSCL-TVD and WENO schemes are employed, the predicted C_L and C_D are shown in Table 6.4 on page 94; the main outcome is that closer far field locations to the body seem to have a greater effect on the WENO computed forces compared with these of the MUSCL-TVD.

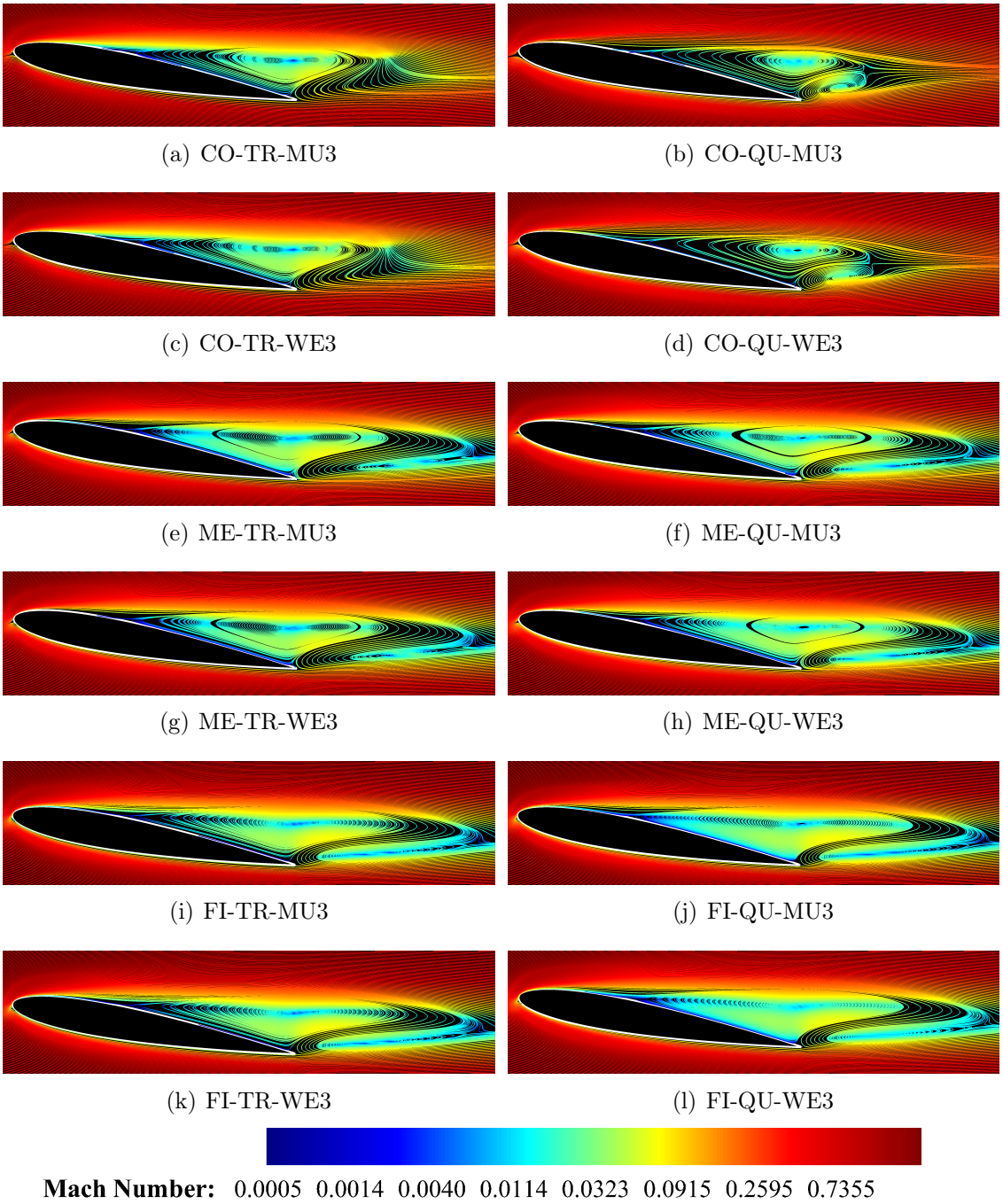

Figure 6.14: Stream-lines and Mach number contours for the transonic flow over the NACA-0012 aerofoil employing the MUSCL-TVD 3^{rd} and WENO 3^{rd}-order schemes; note that the contour levels are in exponential scale; CO, ME, FI refers to the grid size coarse, medium and fine respectively; QU is the quadrilateral and TR the triangular grids $(\alpha = 10^{\circ}, Re : 500, M_{\infty} = 0.8)$.

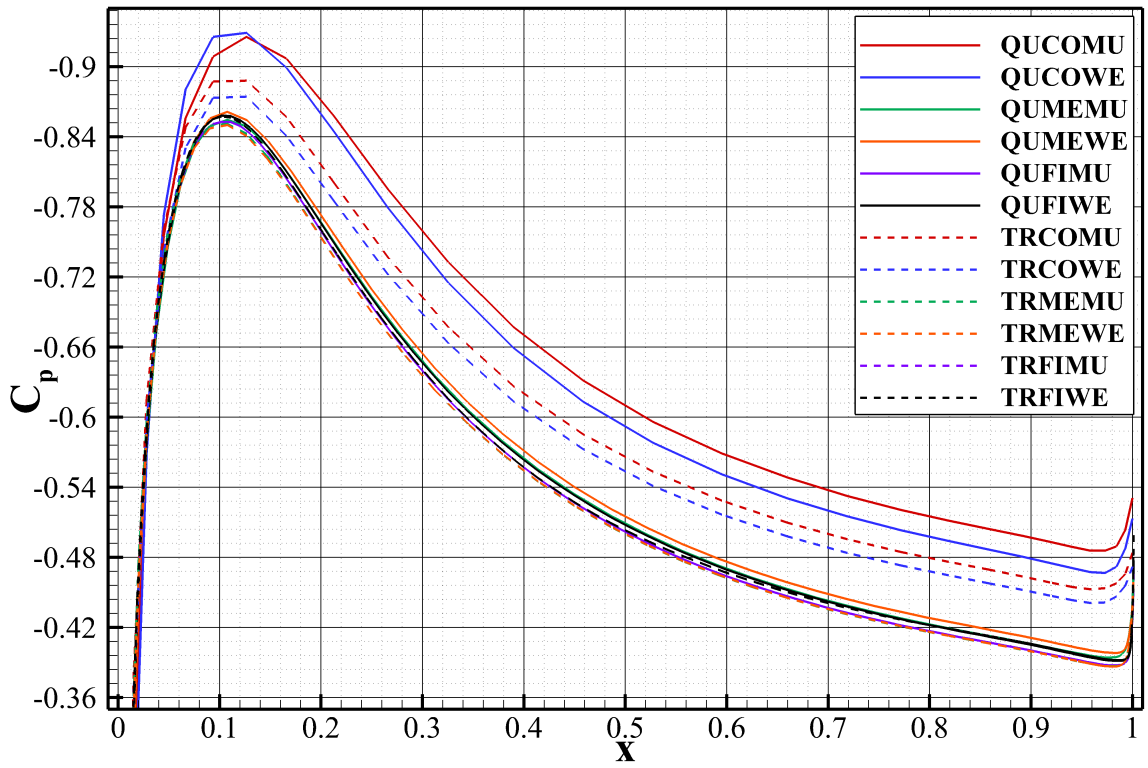

(a) upper aerofoil

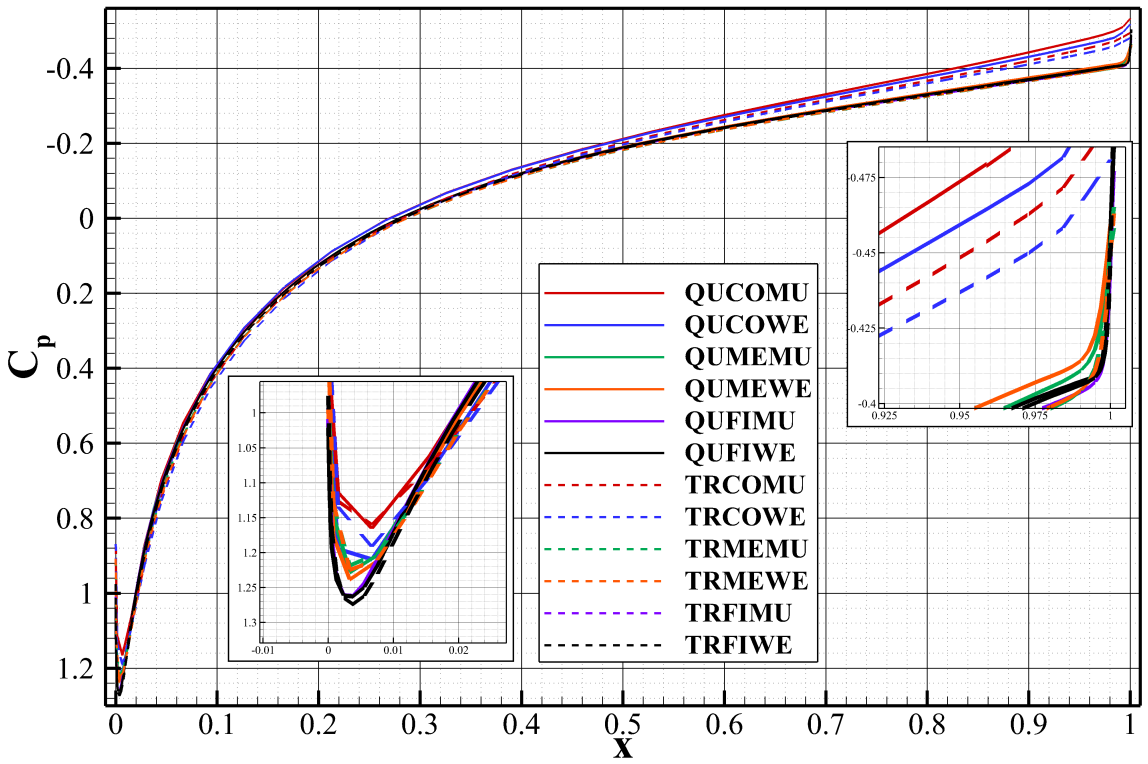

(b) lower aerofoil

Figure 6.15: Coefficient of pressure (C_p) on the upper and lower part of the aerofoil for MUSCL-TVD 3^{rd} and WENO 3^{rd}-order schemes; CO, ME, FI refers to the grid size coarse, medium and fine respectively; QU is the quadrilateral and TR the triangular grids ($\alpha = 10°, Re : 500, M_\infty = 0.8$).

CHAPTER 7

TURBULENT APPLICATIONS

The last chapter is devoted to the applicability of the developed high-order schemes to real life aeronautical applications. Four turbulent flow scenarios are attempted: the subsonic turbulent flow over a flat plate, the subsonic turbulent flow past the NACA-0012 aerofoil at zero degree incident, the fully turbulent subsonic flow over a high-lift three-element aerofoil at a high angle of attack and the supersonic flow through an inclined channel where shock-wave boundary-layer interaction phenomena dominate the subject flow. To account for the high Reynolds number regimes, the Spalart-Allmaras one-equation turbulence model is engaged along with the MUSCL-TVD 2^{nd}, 3^{rd} and the WENO 3^{rd}-order schemes.

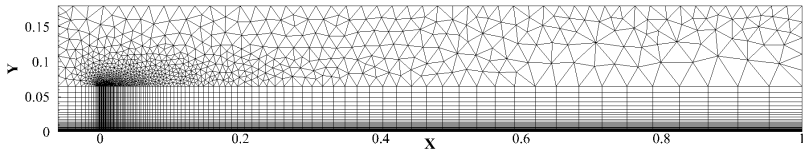

(a) Coarse

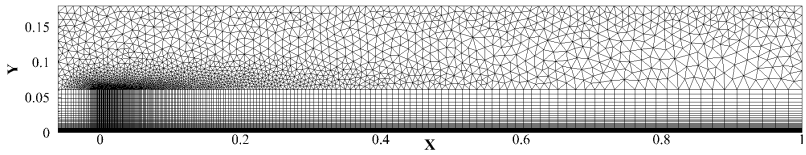

(b) Medium

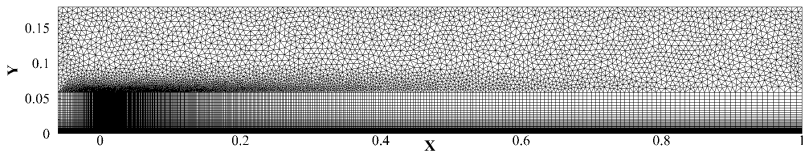

(c) Fine

Figure 7.1: Grids employed for the simulations of the turbulent flow over a flat plate.

7.1 Flow over a Flat Plate

The first turbulent case investigated is the subsonic flow over a flat plate at a free stream Mach number of $M_\infty = 0.2$ and a Reynolds number of $Re = 10{\times}10^6$ based on the length of the plate. This case has as underlying goal to validate the implementation of the SA turbulence model; furthermore, the numerical scheme and turbulence model accuracy are assessed by a grid-refinement analysis. Therefore, three mixed-element grids are generated: a coarse, medium and fine; the grid statistics are tabulated in Table 7.1 on page 98.

Table 7.1: Grid statistics for the turbulent flow over a flat plate

Grid	Nodes	Elements	Quadrilaterals	Triangles	y+
Coarse	5,147	5,940	4,104	1,836	23
Medium	13,489	15,539	10,992	4,547	11
Fine	34,269	39,245	28,520	10,725	5

The refinement of the grids were conceived by doubling the number of nodes on the wall and halving the height of the first wall element; the grids are shown in

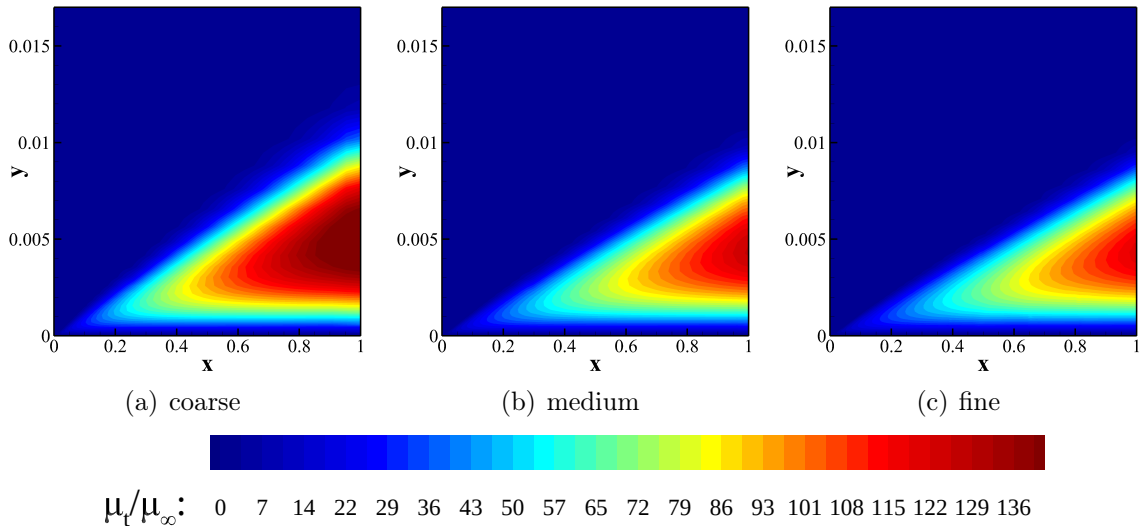

(a) coarse (b) medium (c) fine

Figure 7.2: Normalised eddy viscosity (μ_t/μ_∞) contours computed for the coarse, medium and fine grids with the MUSCL-TVD 2^{nd}-order scheme, for the turbulent flow over a flat plate $\left(Re = 10 \times 10^6, M_\infty = 0.2\right)$.

Figure 7.1 on page 98. The grids span as $[-0.06 \leq x \leq 1.00] \times [0 \leq y \leq 0.180]$ with the length of the plate being unity. A symmetry BC is enforced on the upstream of the plate $[-0.06 \leq x \leq 0.00]$ to avoid numerical error from the inflow uniform velocity profile and to account for the singularity point effect at the leading edge of the plate the grid is locally refined in the stream-wise direction where the plate is set as non-slip adiabatic wall. The MUSCL-TVD 2^{nd}-order scheme is employed along with Forward Euler method for time discretisation, the solution is advanced with a local time stepping procedure.

Figure 7.2 on page 99 shows the amount of turbulent viscosity predicted for the three grids, note that the scaling is independent of the axis; it appears that h-refinement decreases the amount of eddy viscosity which is expected according to the report in [207]. The actual difference in term of eddy viscosity for each grid can be depicted in Figure 7.3 on page 100 (a), furthermore, the disagreement of the coarse with the medium is much more noticeable than that of medium and fine suggesting a convergence trend. Grid convergence can also be observed for the skin friction predictions in Figure 7.3 on page 100, certain discrepancies arise downstream near the outflow boundary particularly noticeable for the coarse grids.

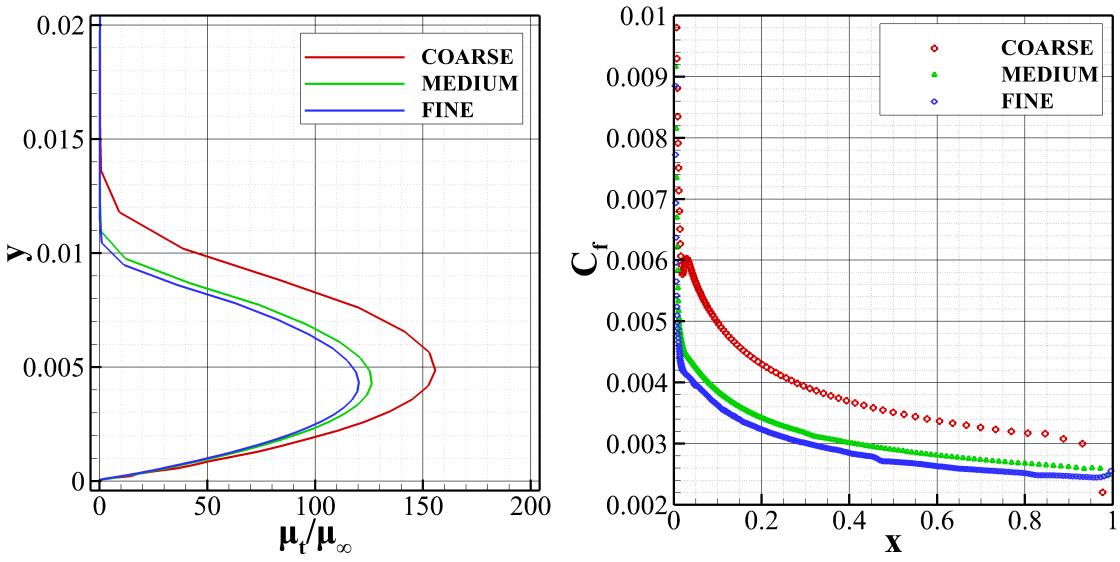

(a) (μ_t/μ_∞) at $x = 0$ (b) C_f

Figure 7.3: Computed eddy viscosity (μ_t/μ_∞) normalised with free-stream viscosity at $x = 1$ and computed skin friction coefficient (C_f) with the MUSCL-TVD 2^{nd}-order scheme, for the turbulent flow over a flat plate $\left(Re = 10 \times 10^6, M_\infty = 0.2\right)$.

7.2 Flow past the NACA-0012 Aerofoil

The subsonic turbulent flow past the NACA-0012 aerofoil is simulated at zero degree incident, the main objective of this test case is to further validate the implementation of the one-equation Spalart-Allmaras turbulence model for a two dimensional aerodynamic flow at high Reynolds number corresponding to real flight conditions: free-stream Mach number of $M_\infty = 0.3$, angle of attack $\alpha = 0°$ and a Reynolds number of $Re = 10 \times 10^6$ based on the aerofoil's chord length, the computations are compared with the NASA-CFL3d solver results [208] at identical conditions. Two C-types mixed-element unstructured grids are utilized for the simulations, where grid parameters are presented in Table 7.2 on page 101. The baseline grid (GRID-1) is the coarsest with a relatively high $y+ \approx 9$, GRID-2 is materialised by locally refining only the quadrilateral zone, since the high Reynolds number induces a de-facto thin boundary layer. The far-field is located at approximately 400 chords lengths where subsonic boundary conditions are enforced, the aerofoil surface is set as adiabatic non-slip wall. Two spatial discretisation schemes are engaged the 2^{nd}-order MUSCL-TVD and the 3^{rd}-order WENO, time advancement is conceived with local time stepping with the 2^{nd}-order forward Euler method and a CFL number of 0.3.

Table 7.2: Grid statistics for the turbulent flow past the NACA-0012 aerofoil

Grid	Nodes	Elements	Quadrilaterals	Triangles	y^+
GRID-1	33,197	46,622	19,200	27,422	9
GRID-2	75,420	88,034	61,360	26,674	2

Summarising the objectives

- validate the SA turbulence model for real aerodynamic applications
- assess the accuracy of MUSCL-TVD and WENO schemes for high Reynolds number flows

From the two dimensional plots of the pressure coefficient in Figure 7.5 on page 103 it is depicted that all results are in good agreement with each other and with the reference solution; it has to be noted that the NASA-CFL3d grid is composed of $525,825$ quadrilaterals with a $y^+ = 0.1$ providing a viable benchmark for the evaluation of the computed results. As expected the greatest discrepancies lie with the predicted C_p of GRID-1 employing a MUSCL-TVD 2^{nd}-order discretisation, for the same grid WENO 3^{rd}-order converges towards the reference solution and the predictions of GRID-2. It is interesting to observe the close-up of the pressure coefficient near the leading edge, where small oscillations are present for the GRID-2 2^{nd}-order scheme, these disturbances are gradually smeared with the employment of high-order discretisation. This behaviour has also been reported in the results of Nguyen et al. [152] utilising a RANS DG high-order methodology. An important point to the aforementioned paper is that amongst the advantages of high-order FV k-exact methods over DG for applications with curved wall boundaries is that it is not necessary to pursue complex adaptations of high-order grids to accurately represent the geometry, since the construction of non-linear WENO stencils covering a wide area with numerous wall-bounded elements implicitly inherits a good approximation of the near-wall flow regime.

The small oscillations observed for the pressure are amplified for the skin friction, where low-order schemes indicate higher frequencies and wider wavelengths; note that, GRID-2 MUSCL-TVD 2^{nd}-order C_f values are discarded for this plot, since severe os-

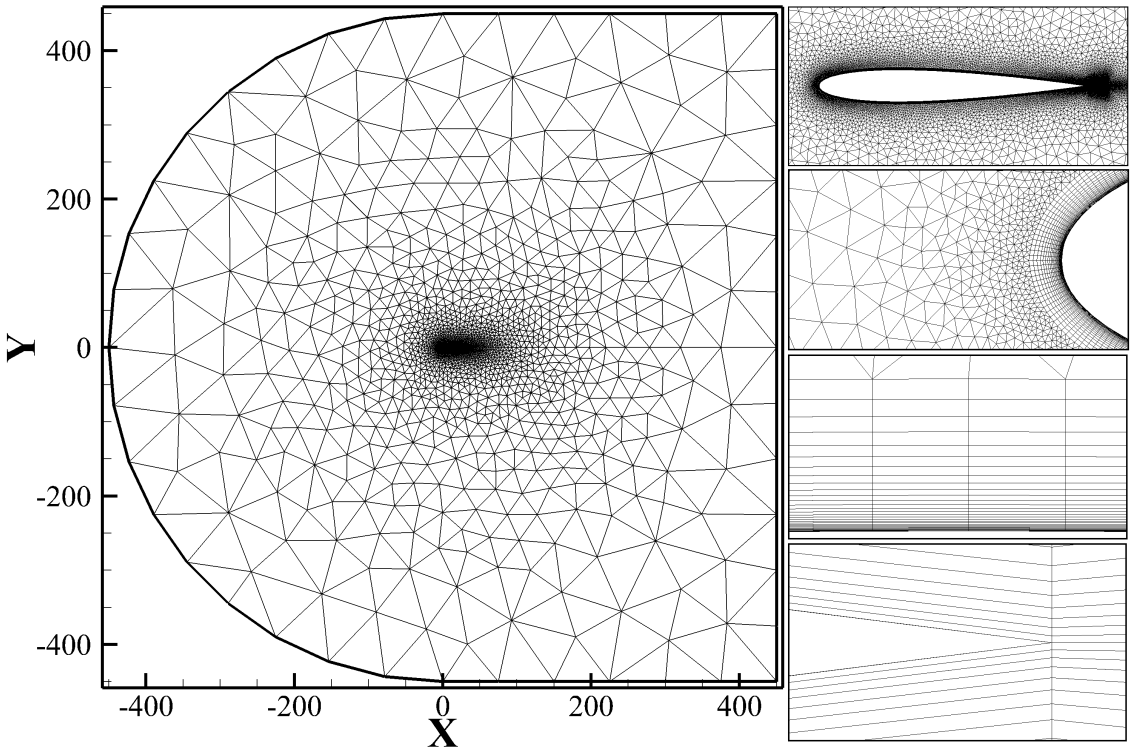

(a) GRID-1

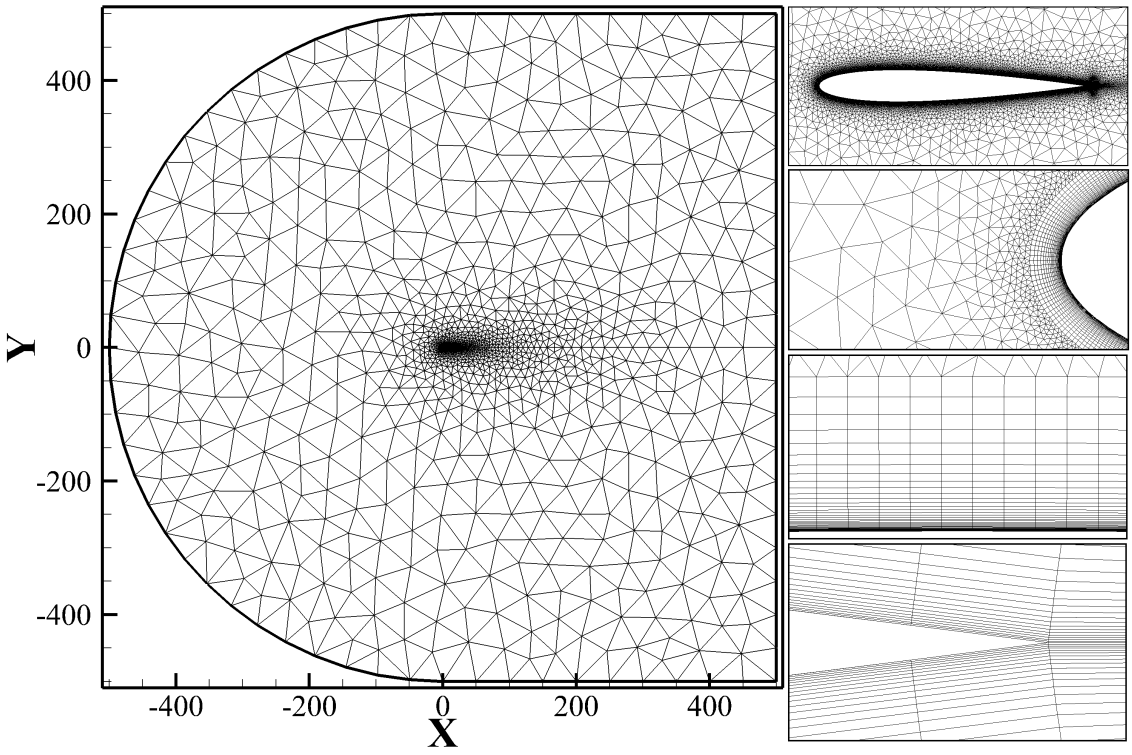

(b) GRID-2

Figure 7.4: Grids employed for the turbulent flow past the NACA-0012 aerofoil.

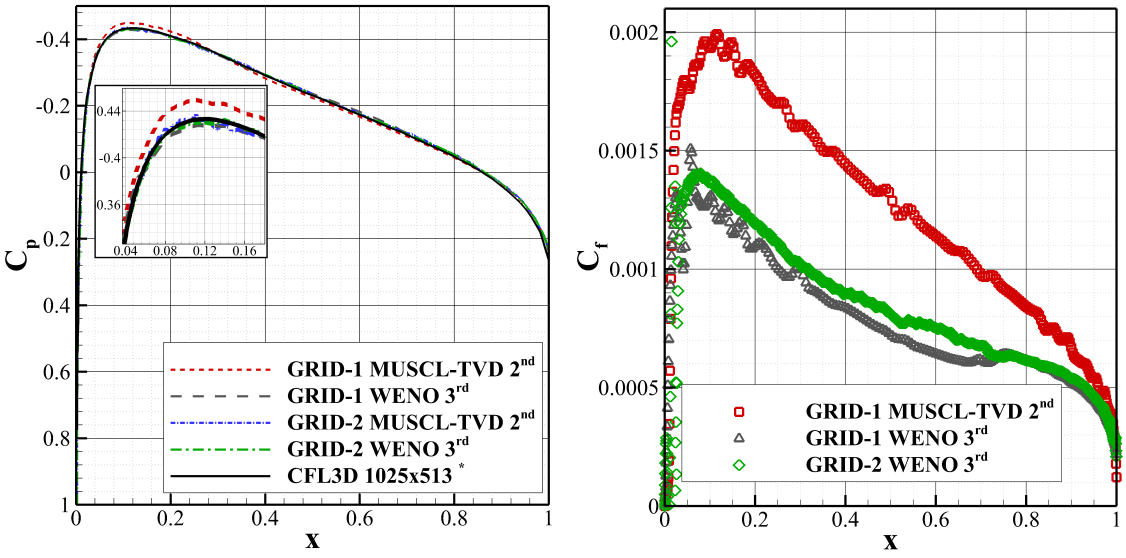

(a) C_p (b) C_f

Figure 7.5: Coefficient of pressure (C_p) and skin friction (C_f) for the turbulent flow past the NACA-0012 aerofoil, results shown for both schemes and grids, C_p results are compared with the NASA-CFL3d solver predictions on a 1025×513 structured grid [208] ($M_\infty = 0.3$, $\alpha = 0°$ and $R_e = 10 \times 10^6$).

cillations dominated the flow. That behaviour seems counterintuitive, one would expect that by employing "h" refinement, the solution would ameliorate; however, the inherited relatively larger numerical dissipation of the coarser grid acts as a stabilizing force by dumping the oscillations of the noticeably over-predicted solution. This problem can be address by employing artificial viscosity or artificial dissipation; these methods were initially developed for shock dominant flows solved with central-based schemes [209, 210] in order to damp spurious oscillation in the vicinity of discontinuities; these dissipative techniques achieve a stable solution by either locally reducing the order or by employing a limiting function for the high frequency solution components. WENO schemes undoubtedly perform better than MUSCL-TVD, suggesting that the required stabilization for the MUSCL-TVD scheme is indigenously present in the WENO. Figure 7.6 on page 104 shows the smooth transition of the the Mach number and normalised viscosities, both laminar and turbulent, computed with the GRID-2 WENO 3^{rd}-order scheme.

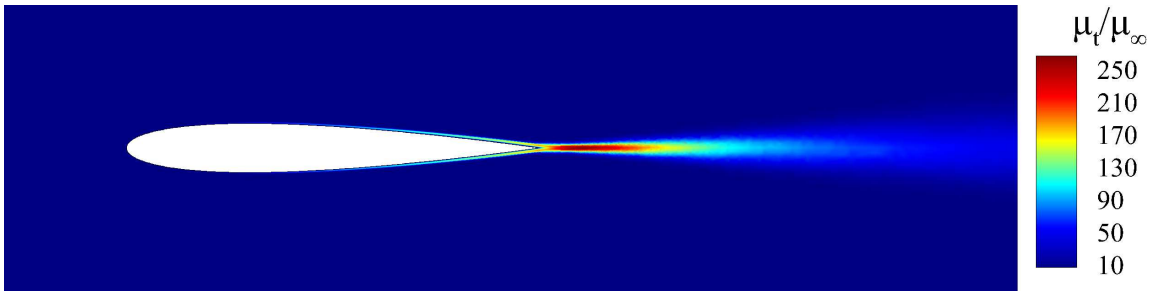

(a) μ_t/μ_∞

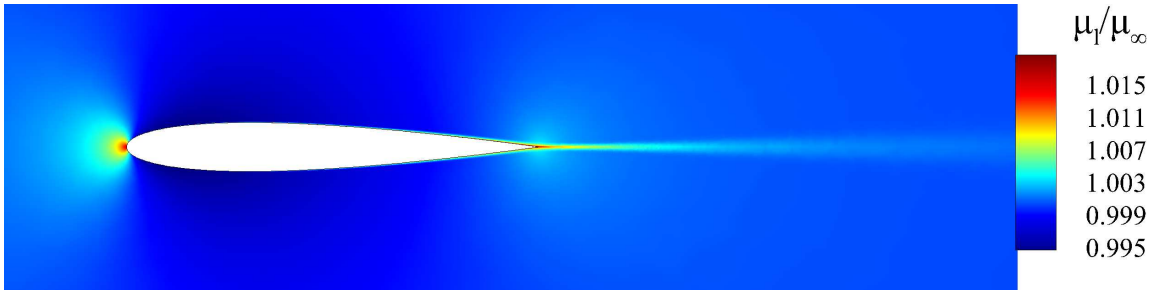

(b) μ_l/μ_∞

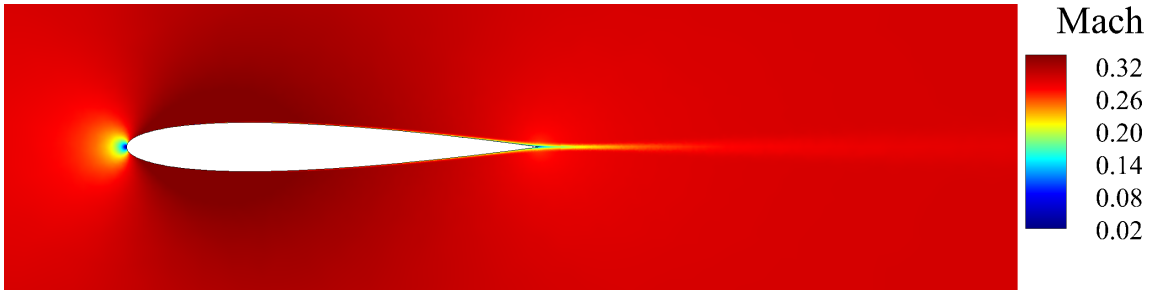

(c) Mach number

Figure 7.6: Computed contours of normalised turbulent (μ_t/μ_∞) and laminar viscosities (μ_l/μ_∞), and Mach number with the 3^{rd}-order WENO scheme on GRID-2 ($M_\infty = 0.3$, $\alpha = 0°$ and $R_e = 10 \times 10^6$).

7.3 Flow past the MD 30P-30N Aerofoil

High-lift devices such as multi-element aerofoils are widely employed in commercial airliners to increase lift for takeoff and landing situations, by delaying flow separation and reducing the pressure rise on each aerofoil element [211]. The flow past a three-element aerofoil will be the subject of the third turbulent case. The configuration employed is the McDonnell-Douglas 30P-30N with deployed slat and flap components shown in Figure 7.7 on page 105, part of the "difficult" cases from the 1^{st} International Workshop on High-Order CFD Methods (2012) [212].

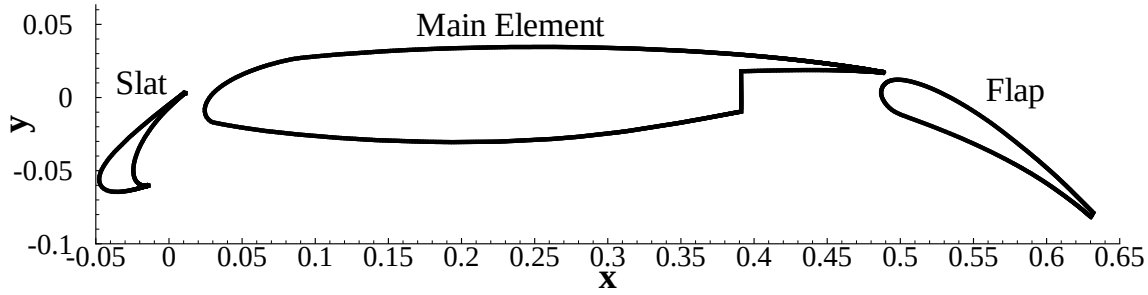

Figure 7.7: McDonnell-Douglas 30P-30N multi-element aerofoil geometry configuration

The flow is characterised by wake interactions between elements, recirculation and displacement thickness of the boundary layer, dictating the overall performance of the device and challenging both experimental and CFD methods. A series of wind-tunnel experiments were conducted at NASA Langley Research Center [213, 214] and at the same time different CFD approaches and turbulence models were assessed and compared with the experimental data [148, 215, 216], with good overall agreement. The actual physical conditions of the fully turbulent flow past the subject multi-element aerofoil are: free-stream Mach number of $M_\infty = 0.2$, angle of attack at $\alpha = 16^\circ$ and a Reynolds number of $Re = 9 \times 10^6$ based on the reference aerofoil chord's length $0.5588\ m$. One mixed-element unstructured grid is employed constituted by $178,356$ nodes, $271,545$ elements from which $81,874$ are quadrilaterals and $189,671$ are triangles with a global $y^+ \approx 5$; Figure 7.8 on page 106 illustrates sections of the grid. The MUSCL-TVD 3^{rd} and WENO 3^{rd}-order schemes are engaged with the local time stepping technique and the 2^{nd}-order forward Euler method for time advancement with a CFL of 0.4. The main aims of this test case are:

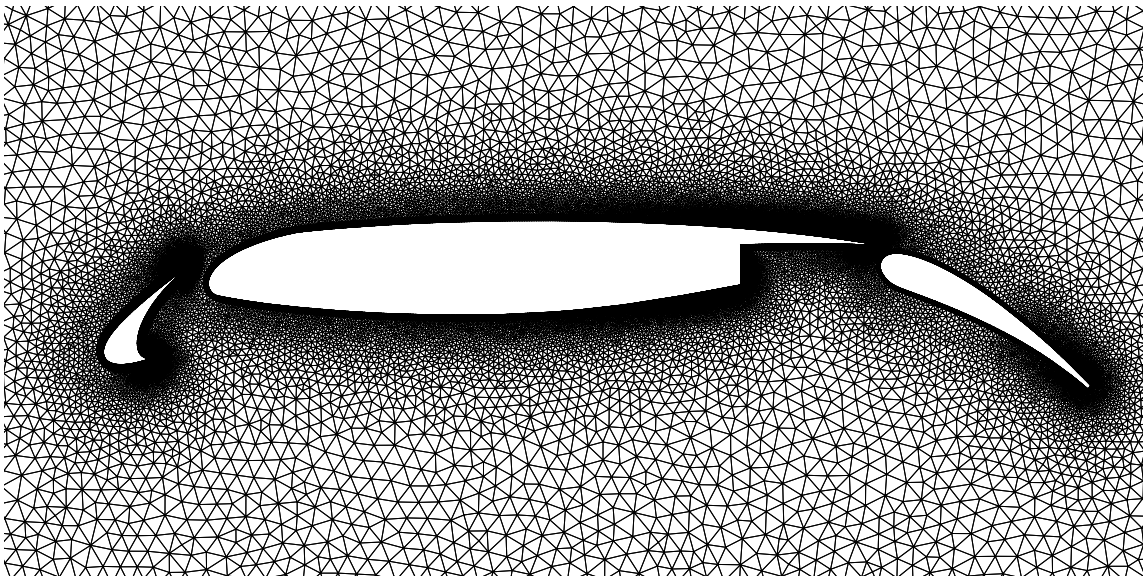

(a) Grid focused on all three elements

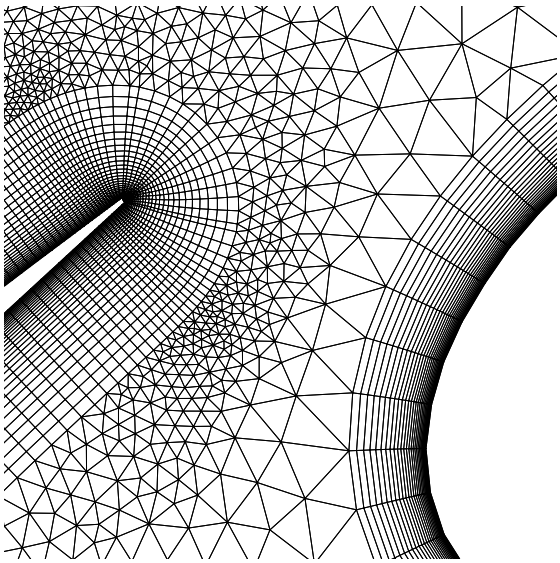

(b) Grid focused on slat and main element

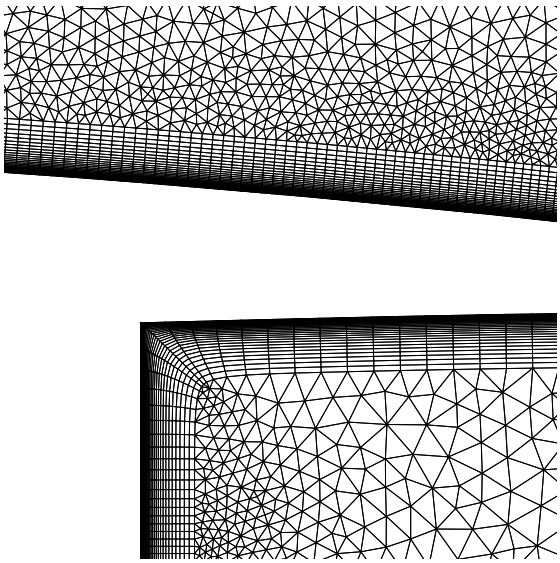

(c) Grid focused on the main element

Figure 7.8: Grid employed for the turbulent flow past the MD 30P-30N multi-element aerofoil.

- address SA model's adequacy for highly turbulent aerodynamic flows combined with high-order discretisation
- assess the SA turbulence model capabilities for strongly separated flows and abilities to produce oscillation-free solution
- compare the predicted solutions of MUSCL-TVD and WENO type schemes

with experimental data

The case under investigation at the designated flight conditions is a topic of continuous research for high-order methods combined with turbulence models, since the numerical performance of the employed solvers is challenged by the strong gradients of the mean flow variables. In addition, the SA model is known for its limited performance for strong vortex dominant flows with larger separation and wake vortices.

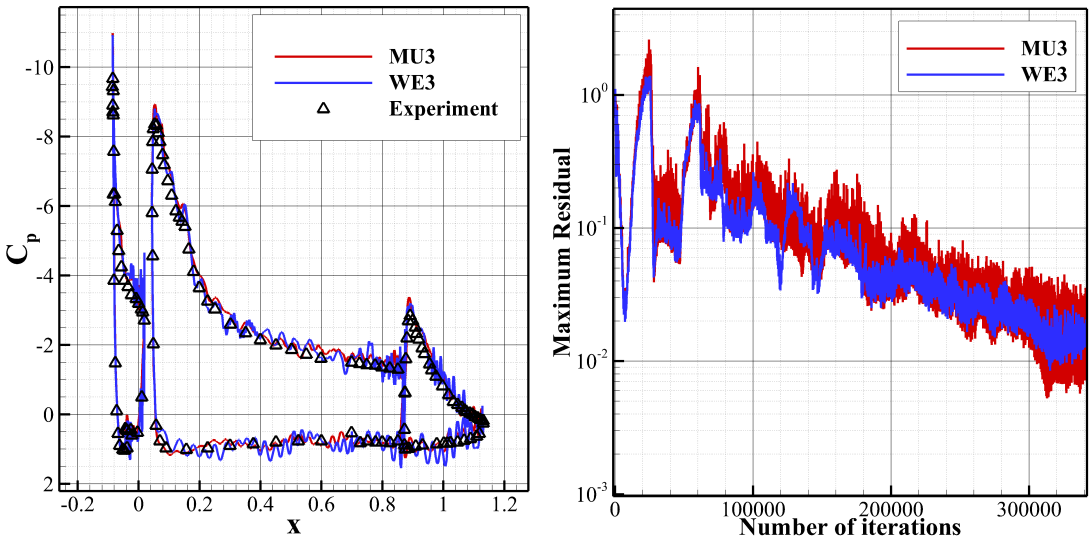

(a) C_p (b) Maximum residual history

Figure 7.9: Coefficient of pressure (C_p) and maximum residual history for the turbulent flow past the MD 30P-30N multi-element aerofoil, results are shown for the MUSCL-TVD 3^{rd} and WENO 3^{rd}-order schemes ($M_\infty = 0.2$, $\alpha = 16°$ and $Re = 9 \times 10^6$).

The flow might appear to be smooth but with h-enrichment, unsteady features are imminently resolved particularly in the vicinity of the flap's trailing edge [148]. This unsteadiness travels upstream as the flow is subsonic, inducing further perturbations on the mean flow variables. These oscillations are mirrored in the plots for the coefficient of pressure, in Figure 7.9 on page 107 where for both schemes the non-smooth behaviour is observed particularly on the trailing edge of the flap. This suggests that there is a lack of required dissipation in order to stabilize the flow. The dissipation can be enhanced either by using a lower-order method, or by employing a coarser grid; in addition, the required physical dissipation through the eddy viscosity seems that is insufficient to produce oscillations-free solutions.

Another possible explanation of the oscillatory effects could lie within the choice of Riemann solver; the HLLC is known for its low numerical dissipation characteristics [136] suggesting that it might be too accurate for the subject case where dissipation is required to stabilise the flow. It is worth noting that, there are no detailed publications and/or studies on the SA model in conjunction with the HLLC Riemann solver. Most high-order discretisation methods with SA turbulence models employ either Roe's [217] or Rusanov's [218] approximate schemes.

In this work, the lower numerical dissipation of the developed WENO type schemes compared with the MUSCL has been extensively proved on several flow problems: inviscid, laminar and turbulent; moreover, WENO schemes inheriting a lower numerical dissipation, try to resolve finer features corresponding to the real physical conditions (non-steady); thus, the pressure coefficient predictions have relatively larger amplitude oscillations than the MUSCL-TVD, particularly noticeable at the trailing edge of the flap. It is also worth noting, that the WENO values for the maximum peaks at the leading edges of all elements are in a better agreement with the experiment. From the history of the maximum residual in Figure 7.9 on page 107 it can be depicted that both schemes have similar convergence trends and rates, additionally, WENO have noticeably smaller oscillations.

The predictions of eddy viscosity for this flow, by employing high-order discretisation combined with the SA model, is known to significantly differ in terms of amount and distribution. The eddy viscosity irregularity is depended upon the type of method (DG or FV) employed and discretisation of the turbulence model equation [219]. Burgess and Mavriplis [219] have studied the effects of high-order methods with the SA model, the main conclusion are:" the increase in turbulence model resolution has an adverse effect on the functional convergence of the simulation and that polynomial refinement substantially increases the amount of eddy viscosity". When switching from MUSCL to WENO for the current case the maximum value increases by approximately 200 units; Figure 7.11 on page 110 shows the distribution of the normalised eddy viscosity with the free-stream viscosity and Figure 7.10 on page 109 illustrates the Mach number contour levels for both simulations, the plots can be considered as indistinguishable.

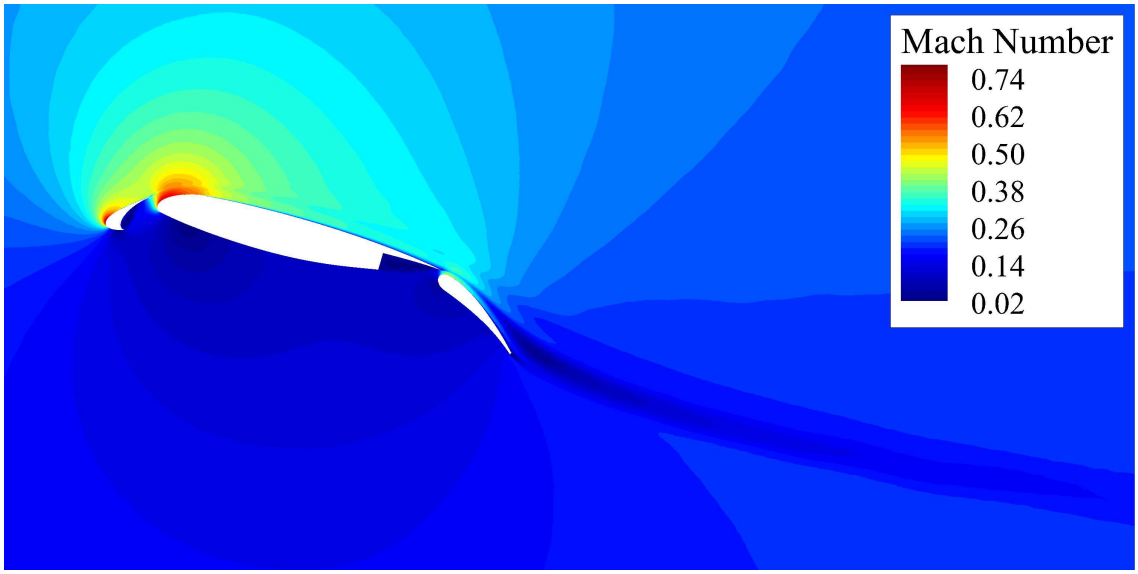

(a) MUSCL-TVD 3^{rd}

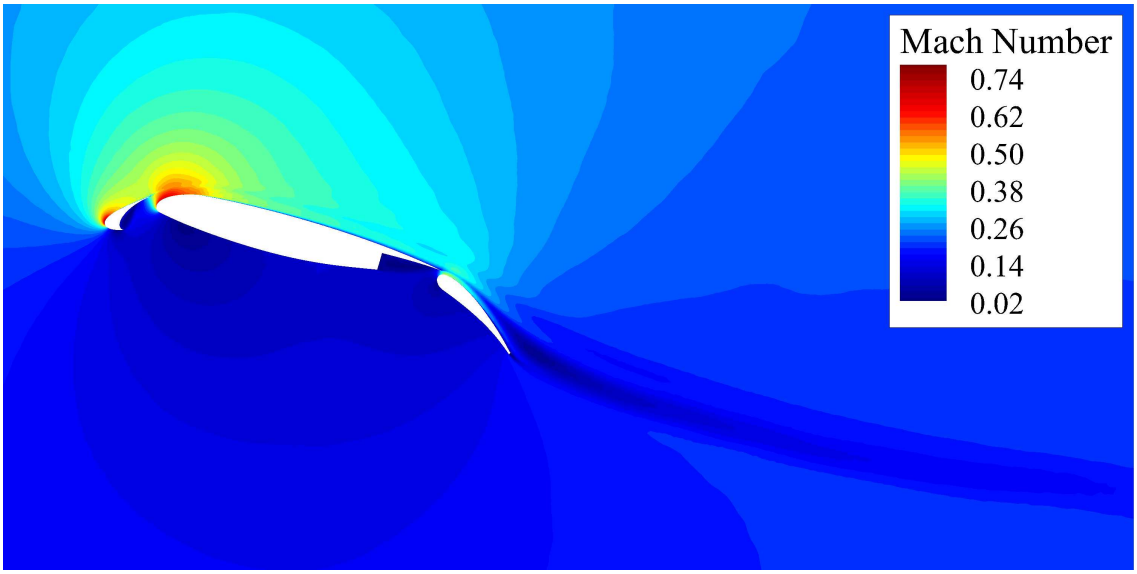

(b) WENO 3^{rd}

Figure 7.10: Mach number contours for the turbulent flow past the MD 30P-30N multi-element aerofoil, results are shown for the MUSCL-TVD 3^{rd} and WENO 3^{rd}-order schemes ($M_\infty = 0.2$, $\alpha = 16^\circ$ and $Re = 9 \times 10^6$).

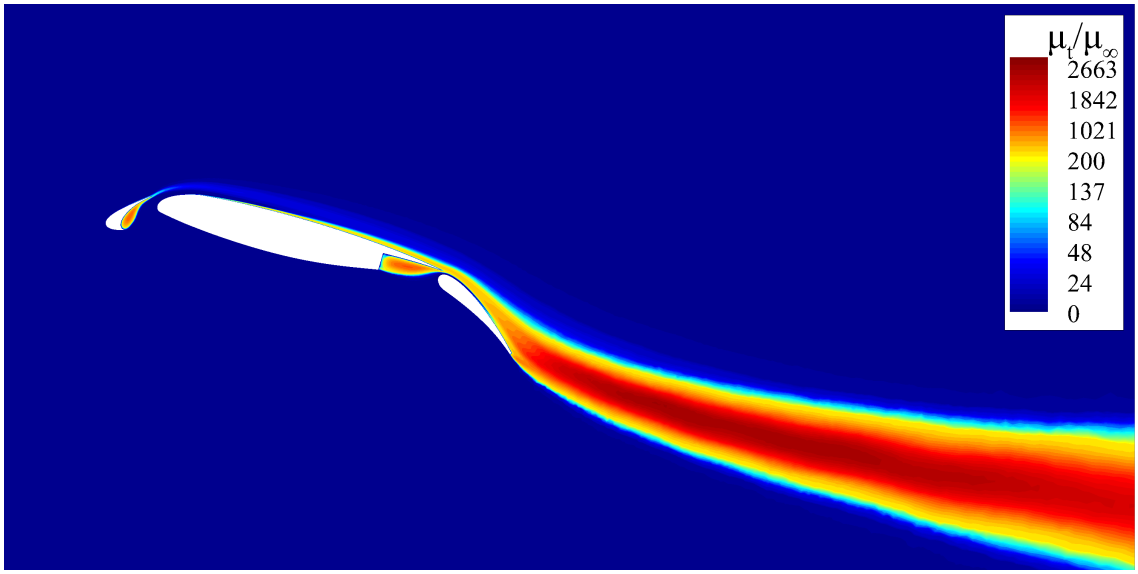

(a) MUSCL-TVD 3^{rd}

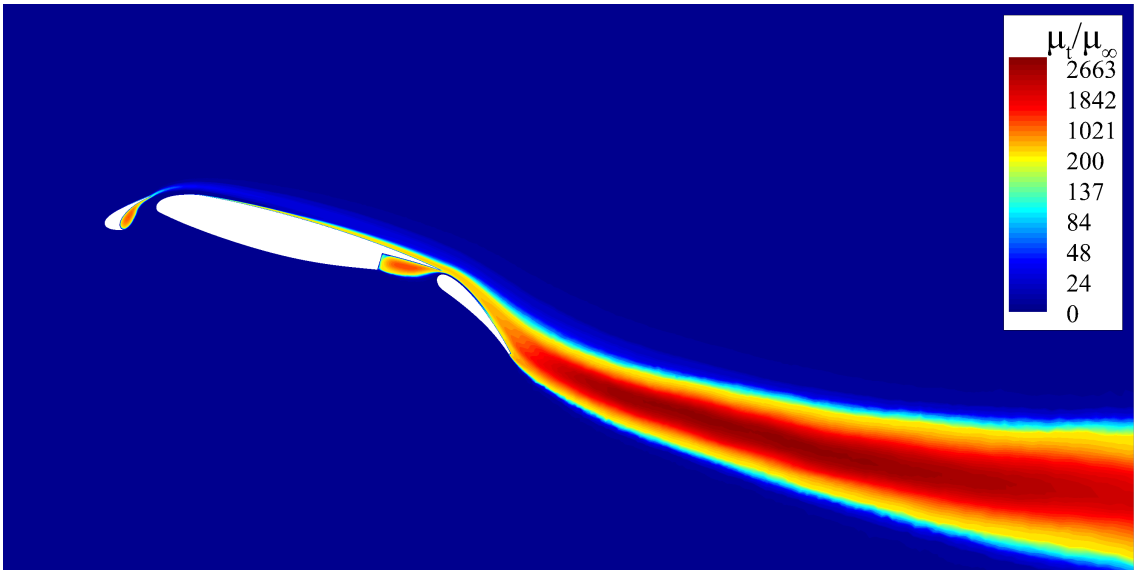

(b) WENO 3^{rd}

Figure 7.11: Normalised eddy viscosity μ_t/μ_∞ with free-stream viscosity contours for the turbulent flow past the MD 30P-30N multi-element aerofoil, results are shown the MUSCL-TVD 3^{rd} and WENO 3^{rd}-order schemes ($M_\infty = 0.2$, $\alpha = 16^\circ$ and $Re = 9 \times 10^6$).

7.4 Shock-Wave Boundary-Layer Interaction

Shock-wave boundary-layer interaction (SWBLI) phenomena is of significant importance for the design of high-speed aircrafts, missiles and projectiles components where the structure is exposed to substantial forces in the presence of fluctuating pressures and excessive thermal loads [220]. Depending upon the Mach number, the angle of the inclined surface acting as a shock generator and the flow regime of the boundary layer, different interactions and shock reflections occur [221].

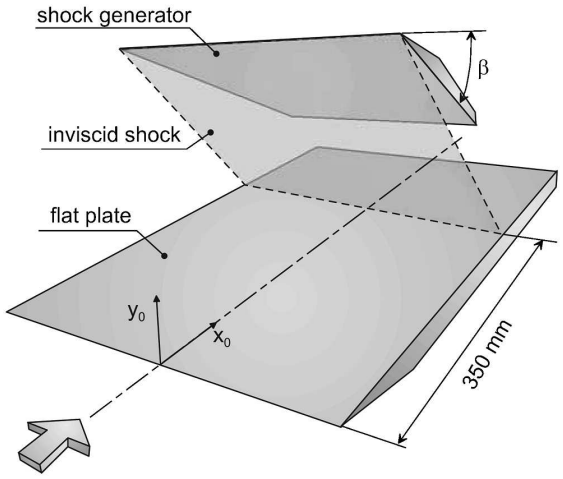

Figure 7.12: Schematics of experimental test model, figure from [222]

Schülein [222] conducted experimental measurements of skin friction and pressure wall distributions for SWBLI flow at three deflection angles at 6°, 10° and 14°, the experiment test model is detailed in Figure 7.12 on page 111. The flow conditions chosen for the numerical computations based on the experiment are: angle of shock generator $\beta = 10°$, freestream Mach number $M_\infty = 5.0$ at a Reynolds number of $Re = 37 \times 10^6/m$ based on the length of the lower flat plate.

The flow is characterised by a high shock intensity of the incident oblique shock impinging on the opposed wall boundary layer. Figure 7.13 on page 112 illustrates the complexity of the flow, where multiple compression waves and expansion fans are created leading to boundary layer separation, which in turn generates a recirculation bubble, independent of the shock intensity, which drastically increases the local pressures and temperatures. The turbulent boundary layer reattaches downstream,

further agitating the flow by generating additional waves and expansion fans and for certain cases redundant fluctuations will disturb the boundary layer [223]. Numerical methods for simulating SWBLI flows is an active area of research as current turbulence models poorly predict skin friction coefficient, wall pressure, separation and reattachment locations compared with experimental data [224].

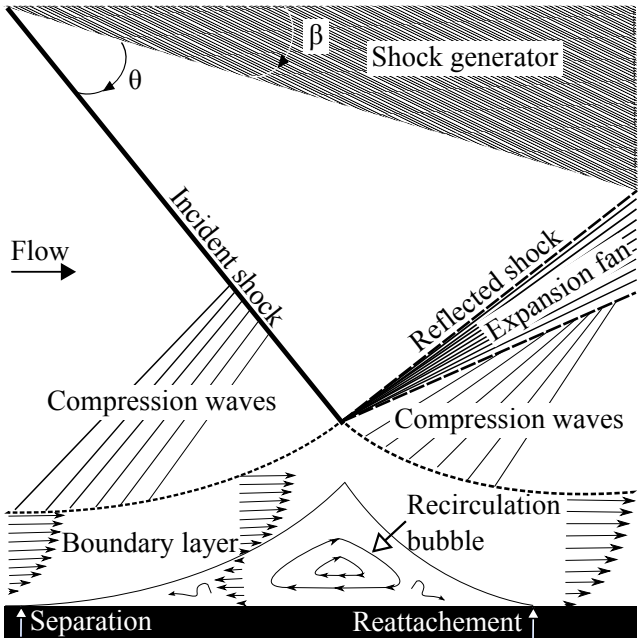

Figure 7.13: Schematics of shock-wave boundary-layer interactions

Table 7.3: Grid statistics for the shock-wave boundary-layer interaction flow.

	Nodes	Elements	Triangles	Quadrilaterals	y^+
GRID-1	45,560	54,796	19,442	35,354	15
GRID-2	116,192	147,212	64,517	82,695	4

Two spatial grids are employed for the subject case, a baseline grid referred to GRID-1 and a secondary grid as GRID-2, which is locally refined to increase the shocks resolution as shown in Figure 7.14 on page 113; the detail parameters of each grids are shown in Table 7.3 on page 112. To speed-up the simulations process, the flow was initialised as inviscid with 1^{st}-order spatial discretisation, prior to switching to either the MUSCL-TVD 3^{rd} or the WENO 3^{rd}-order schemes. Local time stepping is employed since only the steady state flow is considered. Supersonic boundary inflow and outflow conditions are imposed, non-slip adiabatic boundary conditions for the

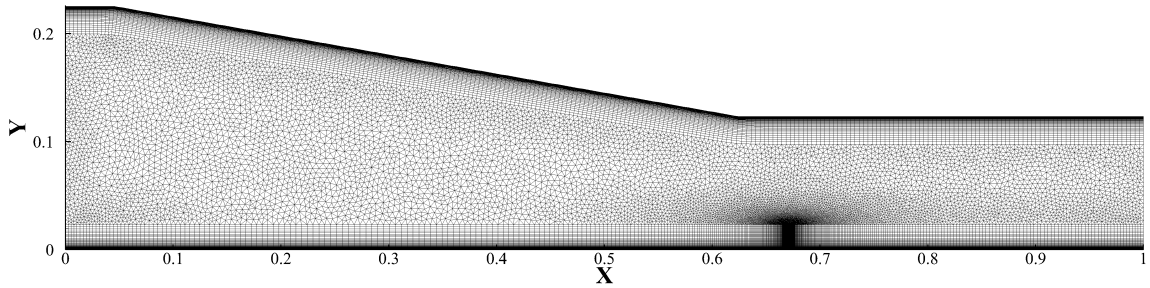

(a) GRID-1

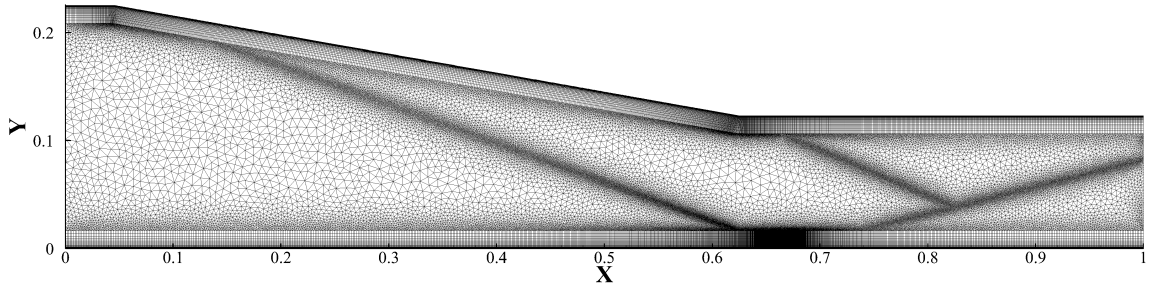

(b) GRID-2

Figure 7.14: Grids employed for the shock-wave boundary-layer interaction flow ($M_\infty = 5.0$, $\beta = 10^\circ$ and $R_e = 37 \times 10^6/m$).

upper and lower walls, where the leading edge on the upper wall downstream from the shock generator is set as symmetry condition. The main objectives of the subject test case are :

- address the challenges of current numerical and turbulence models for SWBLI flows
- employ two types of high-order schemes and analyse their performance for two grids
- compare and assess the computed results with experimental data

There are several aspects that need to be considered for SWBLI flows: the most important being the assumption of the gas dynamics ideal gas law which is on the verge of its validity at hypersonic high temperature conditions, moreover, the non-equilibrium dominance in the boundary layer suggests that the Reynolds analogy between momentum and heat transfer might not stand. Unsteadiness due to shock separation, external turbulence and induced acoustic waves in the boundary layer

transition region are real physical phenomena that ultimately challenge numerical algorithms and turbulence models. Computed heat transfer and skin friction mispredictions are often encountered for SWBLI flows and have been reported by several authors [224–227], with turbulence modelling being the apparent inception of the disagreement with experimental data. The inherent assumption of Morkovin's hypothesis [228] in turbulence models is only valid for moderate Mach numbers and heat loads where viscosity fluctuations can be eligibly discarded [229].

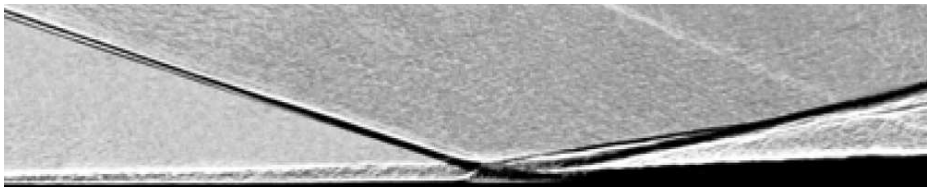

(a) Experimental shadowgraph

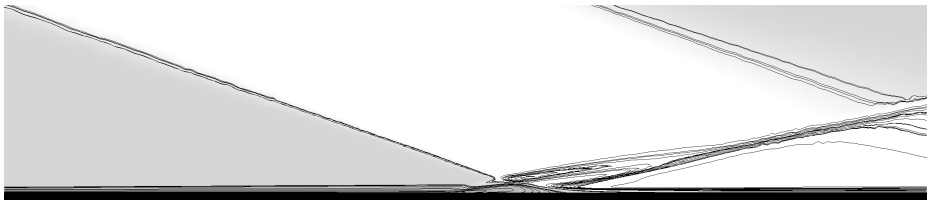

(b) ρ

Figure 7.15: Spark shadowgraph visualisation from the experiment [222] and computed density contours and lines, with the 3^{rd}-order WENO scheme (GRID-1) ($M_\infty = 5.0$, $\beta = 10°$ and $R_e = 37 \times 10^6/m$).

The separation bubble formed under the λ-structure shock interaction region has inherited unsteadiness attributed to its three-dimensional nature [230] inducing the formation of spanwise Taylor-Görtler vortices. Even though the original experimental set up is three dimensional, the two dimensional model employed here, adequately captures the shock's structure as shown in Figure 7.15 on page 114, with the separation and reattachment locations satisfactorily predicted. The separation-region size can also be depicted from the normalised wall pressure plots on the flat plate in Figure 7.16 on page 115. The computed wall pressure and experiment data are in good agreement, with the finer grid (GRID-2) predicting the separation point further downstream, closer to the experimental measurement recovering slightly faster than the computed pressures of GRID-1.

It has been reported by several authors [230, 231] that the increase of shock intensity worsens the agreement between experimental and numerical results, furthermore,

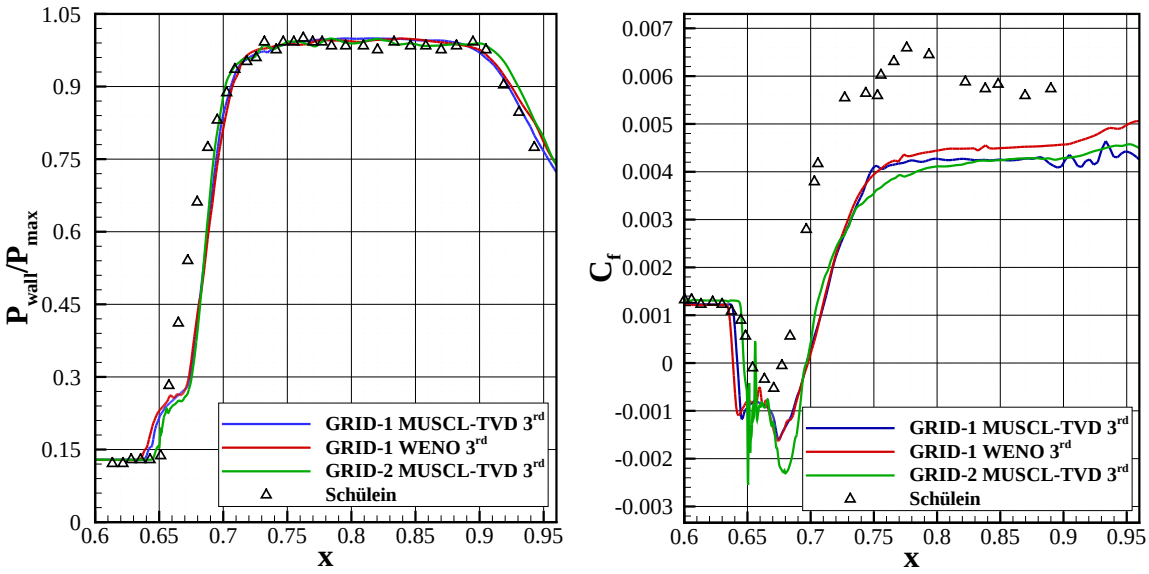

(a) P_{wall}/P_{max} (b) C_f

Figure 7.16: Normalised wall pressure (P_{wall}/P_{max}) and skin friction coefficient (C_f) for the shock-wave boundary-layer interaction flow for GRID-1 and GRID-2 employing the MUSCL-TVD 3^{rd} and WENO 3^{rd}-order schemes, compared with experimental measurements [222] ($M_\infty = 5.0$, $\beta = 10°$ and $R_e = 37 \times 10^6/m$).

turbulence models underestimate the amount of wall shear stress and skin friction values downstream the λ-structure separation region. Even with modification such as variable turbulent Prandtl number [229], and incorporation of shock-unsteadiness operators, the skin friction [232] remains utterly under-resolved. The estimated skin friction for all computed solutions is no exception, the amount is underestimated from the interaction region to the end of the plate. Nevertheless, the WE3 seems to recover with a higher value suggesting that the reduction of numerical dissipation with high-order non-linear schemes would be beneficial for improving wall shear stresses estimations. It has to be noted that the skin friction coefficient in the separation region was not measured by the precise GISF technique, it was estimated by conventional oil-flow visualization method [222].

It is worth noting that the skin friction values in the recirculation zone for the MUSCL-TVD 3^{rd}-order scheme with GRID-2, where at the separation point ($x \approx 0.65$) oscillations are exhibited convulsing the flow downstream with wall shear stresses being underestimated. The presence of these disturbances can be attributed to the relatively smaller amounts of eddy viscosity in the separation region compared with the results using GRID-1; Figure 7.17 on page 117 illustrates the normalised eddy

viscosity in proximity to the lower wall. This is expected with the SA model as similar reduction of the eddy viscosity with h-refinement has been observed with the turbulent flow over a flat plate in Section 7.1. Nevertheless, the lack of turbulent viscosity coupled with the lower numerical error of the finer grid counterbalances the equilibrium of the flow by excessively endorsing the dominance of the convective forces (shocks). In addition, high-order methods inherited lower dissipation properties and are unable to perform steady state solutions (WENO 3^{rd}-order in GRID-2) under these circumstances which require induced dissipation either in the form of a coarse gird or through a dissipative property.

Figure 7.18 on page 118 illustrates the flowfield of the SWBLI flow using Mach number contours for all three simulations; even with the zoomed subfigure to the λ shock recirculation region it is difficult to depict any apparent differences, nevertheless, the resolution of the shock is sharper with the locally refined grid (GRID-2).

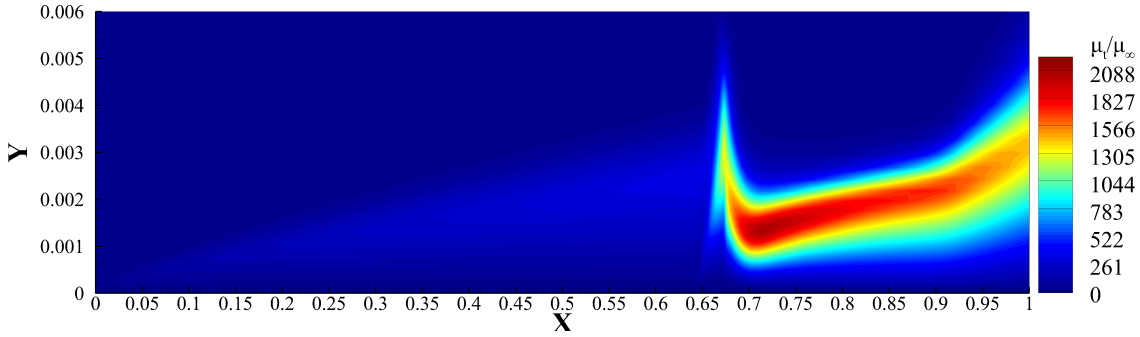

(a) GRID-1 MU3

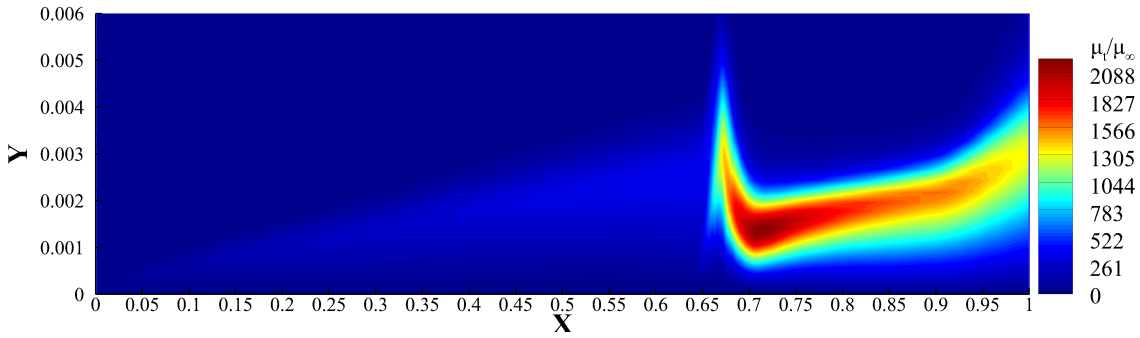

(b) GRID-1 WE3

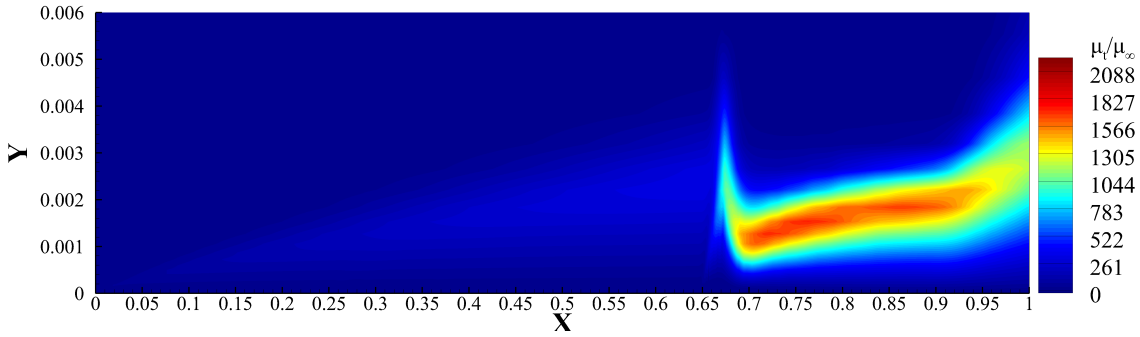

(c) GRID-2 MU3

Figure 7.17: Normalised eddy viscosity μ_t/μ_∞ contours for the shock-wave boundary-layer flow ($M_\infty = 5.0$, $\beta = 10^\circ$ and $R_e = 37 \times 10^6/m$)

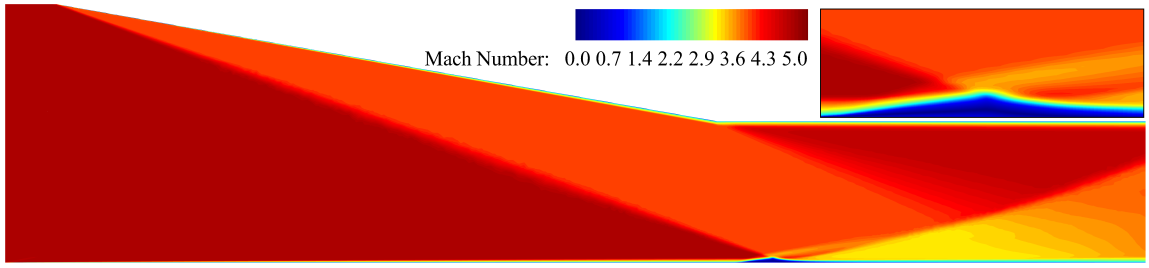

(a) GRID-1 MU3

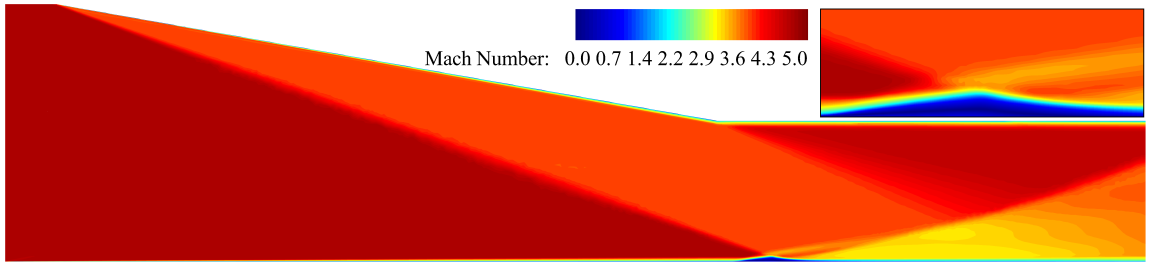

(b) GRID-1 WE3

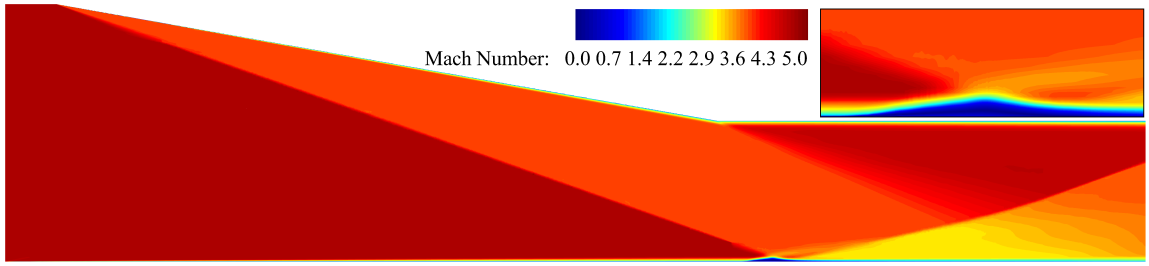

(c) GRID-2 MU3

Figure 7.18: Computed Mach number contours for the shock-wave boundary-layer interaction flow ($M_\infty = 5.0$, $\beta = 10^\circ$ and $R_e = 37 \times 10^6/m$)

CHAPTER 8

CONCLUSIONS AND FUTURE WORK

8.1 Conclusions

Methods

This research work has as underlying goals the development, validation and assessment of two and three dimensional high-order finite volume schemes on mixed-element unstructured grids applied to aeronautical flows. The high-order schemes initially implemented by Tsoutsanis et al. [87] for arbitrary three-dimensional unstructured grids for the Euler's equations are extended to the compressible Navier-Stokes equations to account for viscous dominant applications. The industrial requirement of inexpensive simulations, motivated the adaptation of the original three dimensional solver to two dimensions, furthermore, real aerodynamic flows were conceived with the implementation of the Spalart-Allmaras turbulence model.

The developed method is based on the k-exact reconstruction and can be categorised into two main frameworks: the conventional MUSCL-TVD and the WENO type schemes. The first one employs one central stencil and the solution is piecewise linear inside the element, with discontinuities being captured with a limiting TVD function, whereas the WENO methods utilize a solution adaptive technique with a weighted combination of several stencils resulting in higher resolution in the smooth regions but at the same time damping spurious oscillations in the vicinity of strong gradients.

Scaling effects are omitted by employing a transformation procedure where the coordinates are mapped from the Cartesian space to a reference space. For the WENO type method the admitted stencil elements are submitted to several geometrical conditions to ensure a smooth stencil construction and to reinforce the overall robustness of the scheme. In addition, WENO-type methods make use of the characteristic variables, providing higher efficiency and accuracy compared with the conserved variable formulation. The evaluation of the fluxes follows the same high-order philosophy by utilizing high-order Gaussian quadrature formula on the element's faces for both inviscid and viscous components. Furthermore, the HLLC Riemann solver is engaged for the accurate estimation of the inviscid waves, whereas a compact formulation handles the computation of the viscous terms for which the gradients are evaluated based on the high-order reconstruction. A special treatment for wall-bounded elements is conceived that ensures stability and robustness of the reconstructed system.

Applications

The three-dimensional Taylor-Green vortex flow is simulated with the Euler's equations for hexahedral and tetrahedral grids. The numerical dissipation of the WENO 3^{rd} and WENO 5^{th}-order schemes is assessed on three consecutive refined grids. Tetrahedral elements inherit better kinetic energy conservation properties than hexahedral, suggesting a lower numerical dissipation, attributed to their compactness and arbitrary geometrical orientation which is more in tune with highly vortex dominated flows. Tetrahedral elements achieve a higher maxima of kinetic energy decay rate corresponding to a higher Reynolds number. The developed WENO 5^{th}-order scheme outperforms in terms of numerical dissipation the predictions of the original WENO 5^{th}-order formulation.

The shock capturing abilities of the WENO algorithms are demonstrated with the inviscid transonic flow past the ONERA-M6 wing. Two spatial grids were utilized for the simulations with the computed solutions matching considerably well with the experiment. Polynomial refinement through the engagement of WENO 5^{th}-order scheme substantially ameliorates the agreement and h-refinement enables a noticeably better shock resolution. There are certain small discrepancies accredited to the fact that Euler equations neglect viscosity and shear effects.

The three-dimensional laminar flow over a flat-plate is attempted; the main object-

ive is to evaluate the performance of hexahedral and prismatic elements for boundary layer computations by employing the WENO 3^{rd}-order numerical algorithm. The hexahedral elements seem to be more efficient for estimating the boundary layer growth by resolving the parabolic velocity profile more precisely, however, prismatic elements inheriting the flexibility for capturing better wall surfaces are in better agreement for the estimation of wall shear stresses with the analytical solution.

Computations of the subsonic laminar flow over the NACA-0012 aerofoil at zero angle of attack were performed with the MUSCL-TVD 3^{rd}, WENO 3^{rd} and WENO 5^{th}-order schemes performing adequately well compared with a reference solution. Switching form MUSCL-TVD to WENO improves the estimation of the exerted forces on the body, moreover, small oscillations are observed on the convergence of the forces with the 5^{th}-order scheme associated with its incorporated low numerical dissipation, endeavoring to resolve smaller scale features which are present on the actual three dimensional flow.

The cross comparison of MUSCL-TVD 3^{rd} and WENO 3^{rd}-order schemes for the transonic laminar flow at a positive angle of attack through a grid convergence study with triangular and quadrilateral grids enables a thorough evaluation of the numerical scheme's performance. From the results it can be depicted that WENO outperform MUSCL-TVD schemes with the most substantial differences occurring for the coarsest grids. However, it seems that WENO schemes are more sensitive to the proximity of the far-field location with respect to the aerofoil.

The validation of the implementation of the Spalart-Allmaras turbulence model is achieved with the subsonic turbulent flow over a flat plate employing the MUSCL-TVD 2^{nd}-order discretisation method. A grid convergence study on three consecutive refined grids allows to confidently confirm a correct functioning of the model, demonstrated by the convergence of the computed solutions.

Further validation of the turbulence model is accomplished with the computations of the turbulent flow past the NACA-0012 aerofoil at a high Reynolds number where the computed results are compared with a well proven reference solution. For these cases, in addition to the MUSCL-TVD 2^{nd}-order scheme, the WENO 3^{rd}-order was engaged. Two mixed-element grids are used for the simulations and interesting conclusions are drawn: firstly, h-refinement does not guarantee a stable solution for

the low-order scheme, this might suggest the requirement for an artificial viscosity stabilization technique and secondly, high-order schemes perform much better with resolving the flow with noticeable lesser oscillations.

The fully turbulent flow over a three-element aerofoil (MD 30P-30N) is attempted with the MUSCL-TVD 3^{rd} and WENO 3^{rd}-order schemes and compared with experimental data. The trend of the computed solutions are in good agreement with the experiment. However, there are certain oscillations attributed to the imbalanced dissipation between the low-dissipative schemes, the fine employed grid and the mispredicted amounts of eddy viscosity from the Spalart-Allmaras model.

The supersonic flow through an inclined channel is considered where shock-wave boundary-layer interactions are dominantly controlling the dynamics of the flow field. Two spatial grids are generated and the MUSCL-TVD 3^{rd} and the WENO 3^{rd}-order schemes are engaged for the computations. Turbulence models inherit several physical assumptions, ergo their applicability becomes limited when physical conditions exceed the barrier of their initial design frontier. This is the case with the subject flow, even if pressures are in good agreement with the experiment, the computed shear stresses are undeniably under-predicted. Similar trends are observed with the previous case, where grid refinement in conjunction with polynomial refinement induces the creation of oscillations for the estimation of wall shear stresses.

8.2 Future Work

The main challenge of high-order methods with turbulence modelling is associated with the actual model's inabilities to provide oscillation free solutions without reducing the order of accuracy. Furthermore, in this work this behaviour has been established in the context of high-order k-exact MUSCL-TVD and WENO schemes in conjunction with the Spalart-Allmaras model. This has been recently reported by other authors, employing high-order discontinuous Galerkin type methods to the RANS equations [65, 153, 233, 234]. Furthermore, there are certain techniques that have been applied to the aforementioned publications to avoid non-smooth behaviours and enhance the robustness of the subject high-order solver. However, these

stabilization techniques have to be thoroughly examined and studied as they have counter-effects such as, locally decreasing the order of accuracy and producing negative eddy viscosity. It appears that aspects constituting high resolution in the context of high-order discretisation have to be altered in order to accommodate the outdated but popular RANS techniques e.g. HLLC Riemann solver.

There is a great potential for future research to re-calibrate current turbulence models or even develop new ones that will be more in tune with high-order methods and acquire the advantages of both worlds: maintain smaller discretisation error and numerical dissipation (high-order schemes) and extend their applicability to an abundant type of fluid dynamic flows (RANS).

There are several future research directions regarding high-order methods on mixed-element unstructured grids that can be pursued. They can be categorised into two main frameworks: methodology and applicability. Both are strongly interconnected and one depends on the other's success; in detail:

- Implement Spalart-Allmaras turbulence model to account for 3D real aerodynamic flows in the context of the k-exact finite volume methods and assess the performance of MUSCL-TVD against WENO type schemes. Investigate further the test cases presented in this work by: constructing 3D grids for the ONERA-M6 wing and SWBLI case to account for viscous regimes and three-dimensional effects respectively.
- Assess and study the limitations of current turbulence models in conjunction with high-order methods (WENO) on unstructured grids in 2D and 3D and analyse model's sub-parameters, constants and functions for simple flow problems.
- ILES-RANS, for what kind of applications would this combination be more suited ? Address the challenges of turbulence modelling for resolving near-wall regions and analyse the possible coupling procedures with LES or ILES methods employed for the wake of the flow and the far-wall regions.
- Study in a systematic way the effects of accurate, low-dissipation Riemann solvers combined with turbulence models and assess their capabilities and limitations in a broad range of applications.

- Investigate oscillatory behavior for well-refined grids with high-order methods and the Spalart-Allmaras model; in addition, quantify the amount of inherited numerical dissipation in high-order fluid dynamic computations, including dissipation due to: the spatial domain, spatial discretisation, evaluation of inviscid and viscous fluxes, gradients reconstruction and approximation, boundary conditions and turbulence model terms. Correlate each numerical dissipation source for arbitrary unstructured grids with respect to the order of accuracy.

- Extend the applicability of the methods by: coupling with local control-volume distributed schemes to account for porous media and multi-phase flows [235], develop and implement high-order schemes for the time-domain solution of Maxwell's equations for magnetohydrodynamic applications [236].

- Weakly and strongly couple the developed finite volume high-order schemes with finite element based structural solvers to be able to study fluid-structure interaction flow problems by adopting adaptive grid refinement techniques.

- Adopt well proven front tracking methods [237] and shock capturing sensor techniques [238] to perform automated polynomial refinement in the flow regions of interest.

- Address the hampered accuracy on the boundaries for unstructured grids with a relatively simple, elegant and robust approximation method.

Bibliography

[1] J. C. Vassberg. Expectations for computational fluid dynamics. International Journal of Computational Fluid Dynamics, 19(8):549–558, 2005.

[2] B. Sanderse, S. P. Van Der Pijl, and B. Koren. Review of computational fluid dynamics for wind turbine wake aerodynamics. Wind Energy, 14(7):799–819, 2011.

[3] B. Blocken and C. Gualtieri. Ten iterative steps for model development and evaluation applied to computational fluid dynamics for environmental fluid mechanics. Environmental Modelling and Software, 33:1–22, 2012.

[4] R. Ramponi and B. Blocken. CFD simulation of cross-ventilation for a generic isolated building: Impact of computational parameters. Building and Environment, 53:34–48, 2012.

[5] P. Edge, M. Gharebaghi, R. Irons, R. Porter, R. T. J. Porter, M. Pourkashanian, D. Smith, P. Stephenson, and A. Williams. Combustion modelling opportunities and challenges for oxy-coal carbon capture technology. Chemical Engineering Research and Design, 89(9):1470–1493, 2011.

[6] P. Middha and O. R. Hansen. Using computational fluid dynamics as a tool for hydrogen safety studies. Journal of Loss Prevention in the Process Industries, 22(3):295–302, 2009.

[7] N. Djilali. Computational modelling of polymer electrolyte membrane (PEM) fuel cells: Challenges and opportunities. Energy, 32(4):269–280, 2007.

[8] K. H. Fraser, M. E. Taskin, B. P. Griffith, and Z. J. Wu. The use of computational fluid dynamics in the development of ventricular assist devices. Medical Engineering and Physics, 33(3):263–280, 2011.

[9] A. Rahimian, I. Lashuk, S. K. Veerapaneni, A. Chandramowlishwaran, D. Malhotra, L. Moon, R. Sampath, A. Shringarpure, J. Vetter, R. Vuduc, D. Zorin, and G. Biros. Petascale direct numerical simulation of blood flow on 200k cores and heterogeneous architectures. In 2010 ACM/IEEE International Conference for High Performance Computing, Networking, Storage and Analysis, SC 2010, 2010.

[10] D. Y. Arifin, L. Y. Lee, and C. Wang. Mathematical modeling and simulation of drug release from microspheres: Implications to drug delivery systems. Advanced Drug Delivery Reviews, 58(12-13):1274–1325, 2006.

[11] T. Norton and D. Sun. Computational fluid dynamics (CFD) - an effective and efficient design and analysis tool for the food industry: A review. Trends in Food Science and Technology, 17(11):600–620, 2006.

[12] J. B. Vos, A. Rizzi, D. Darracq, and E. H. Hirschel. Navier-stokes solvers in european aircraft design. Progress in Aerospace Sciences, 38(8), 2002.

[13] K. Becker and J. Vassberg. Numerical aerodynamics in transport aircraft design, volume 100 of Notes on Numerical Fluid Mechanics. 2009.

[14] C. C. Rossow and L. Cambier. European numerical aerodynamics simulation systems, volume 100 of Notes on Numerical Fluid Mechanics. 2009.

[15] Z.G. Wang. High-order methods for the Euler and Navier-Stokes equations on unstructured grids. Progress in Aerospace Sciences, 43:1–41, 2007.

[16] P. J. Roache. Quantification of uncertainty in computational fluid dynamics, volume 29 of Annual Review of Fluid Mechanics. 1997.

[17] A. F. Antoniadis, D. Drikakis, B. Zhong, G. Barakos, R. Steijl, M. Biava, L. Vigevano, A. Brocklehurst, O. Boelens, M. Dietz, M. Embacher, and W. Khier. Assessment of CFD methods against experimental flow measurements for helicopter flows. Aerospace Science and Technology, 19(1):86–100, 2012.

[18] M. R. Visbal and D. V. Gaitonde. On the use of higher-order finite-difference schemes on curvilinear and deforming meshes. Journal of Computational Physics, 181(1):155–185, 2002.

[19] S. Pirozzoli. Numerical methods for high-speed flows, volume 43 of Annual Review of Fluid Mechanics. 2011.

[20] M. Aftosmis, D. Gaitonde, and T. S. Tavares. Behavior of linear reconstruction techniques on unstructured meshes. AIAA Journal, 33(11):2038–2049, 1995.

[21] K.W. Anderson. A grid generation and flow solution method for the Euler equations on unstructured grids. Journal of Computational Physics, 110(1): 23–38, 1994.

[22] T.J. Barth and D.C. Jespersen. The design and application of upwind schemes on unstructured meshes. AAIA, Aerospace science meeting, 89(0366), 1989.

[23] R.J. Leveque. Finite Volume methods for hyberbolic problems. Cambridge University Press, 2002.

[24] A. Harten. High resolution schemes for hyperbolic conservation laws. Journal of Computational Physics, 49(3):357–393, 1983.

[25] J. L. Steger and R. F. Warming. Flux vector splitting of the inviscid gas-dynamic equations with application to Finite-Difference methods. Journal of Computational Physics, 40(2):263–293, 1981.

[26] J. A. Ekaterinaris. High-order accurate, low numerical diffusion methods for aerodynamics. Progress in Aerospace Sciences, 41(3-4):192–300, 2005.

[27] T. J. R. Hughes, L. P. Franca, and M. Balestra. A new Finite Element formulation for Computational Fluid Dynamics: V. circumventing the babuŽka-brezzi condition: a stable Petrov-Galerkin formulation of the Stokes problem accommodating equal-order interpolations. Computer Methods in Applied Mechanics and Engineering, 59(1):85–99, 1986.

[28] R. Löhner, K. Morgan, and O. C. Zienkiewicz. An adaptive Finite Element procedure for compressible high speed flows. Computer Methods in Applied Mechanics and Engineering, 51(1-3):441–465, 1985.

[29] B. Cockburn and C. W. Shu. The Runge-Kutta Discontinuous Galerkin method for conservation laws V: Multidimensional systems. Journal of Computational Physics, 141(2):199–224, 1998.

[30] L. T. Diosady and D. L. Darmofal. Preconditioning methods for Discontinuous Galerkin solutions of the Navier-Stokes equations. Journal of Computational Physics, 228(11):3917–3935, 2009.

[31] B. Cockburn and C. . Shu. The local Discontinuous Galerkin method for time-dependent convection-diffusion systems. SIAM Journal on Numerical Analysis, 35(6):2440–2463, 1998.

[32] B. Cockburn and C. W. Shu. Runge-Kutta Discontinuous Galerkin methods for convection-dominated problems. Journal of Scientific Computing, 16(3): 173–261, 2001.

[33] A. Harten, B. Engquist, S. Osher, and S. R. Chakravarthy. Uniformly high order accurate Essentially Non-Oscillatory schemes, III. Journal of Computational Physics, 71(2):231–303, 1987.

[34] C.W. Shu and S. Osher. Efficient implementation of Essentially Non-Oscillatory shock-capturing schemes. Journal of Computational Physics, 77(2):439–471, 1988.

[35] C. W. Shu and S. Osher. Efficient implementation of Essentially Non-Oscillatory shock-capturing schemes, II. Journal of Computational Physics, 83(1):32–78, 1989.

[36] R. Abgrall. On Essentially Non-Oscillatory schemes on unstructured meshes: analysis and implementation. Journal of Computational Physics, 114(1):45–58, 1994.

[37] O. Friedrich. Weighted Essentially Non-Oscillatory schemes for the interpolation of mean values on unstructured grids. Journal of Computational Physics, 144(1):194–212, 1998.

[38] X. Liu, S. Osher, and T. Chan. Weighted Essentially Non-Oscillatory schemes. Journal of Computational Physics, 115(1):200–212, 1994.

[39] C. Hu and C.W. Shu. Weighted Essentially Non-Oscillatory schemes on triangular meshes. Journal of Computational Physics, 150(1):97–127, 1999.

[40] G. Jiang and C. W. Shu. Efficient implementation of weighted ENO schemes. Journal of Computational Physics, 126(1):202–228, 1996.

[41] P. L. Roe. Characteristic-based schemes for the Euler equations. Annual Review of Fluid Mechanics, 1:337–365, 1986.

[42] R. Abgrall. Essentially Non-Oscillatory Residual Distribution schemes for hyperbolic problems. Journal of Computational Physics, 214(2):773–808, 2006.

[43] R. Abgrall and M. Mezine. Construction of second order accurate monotone and stable Residual Distribution schemes for unsteady flow problems. Journal of Computational Physics, 188(1):16–55, 2003.

[44] H. Nishikawa. High order discretization of diffusion terms in Residual Distribution methods. CFD-higher order discretization methods, von Karman Institute for Fluid Dynamics, 2006.

[45] R. E. Harris and Z. J. Wang. High-order adaptive quadrature-free spectral volume method on unstructured grids. Computers and Fluids, 38(10):2006–2025, 2009.

[46] Y. Liu, M. Vinokur, and Z. J. Wang. Spectral (finite) volume method for conservation laws on unstructured grids v: Extension to three-dimensional systems. Journal of Computational Physics, 212(2):454–472, 2006.

[47] T. Haga, K. Sawada, and Z. J. Wang. An implicit LU-SGS scheme for the spectral volume method on unstructured tetrahedral grids. Communications in Computational Physics, 6(5):978–986, 2009.

[48] A. T. Patera. A Spectral Element method for fluid dynamics: Laminar flow in a channel expansion. Journal of Computational Physics, 54(3):468–488, 1984.

[49] Y. Sun, Z. J. Wang, and Y. Liu. High-order multidomain Spectral Difference method for the Navier-Stokes equations on unstructured hexahedral grids. Communications in Computational Physics, 2(2):310–333, 2007.

[50] A. Jameson. A proof of the stability of the Spectral Difference method for all orders of accuracy. Journal of Scientific Computing, 45(1-3):348–358, 2010.

[51] C. Liang, R. Kannan, and Z. J. Wang. A p-multigrid Spectral Difference method with explicit and implicit smoothers on unstructured triangular grids. Computers and Fluids, 38(2):254–265, 2009.

[52] K. Van Den Abeele, C. Lacor, and Z. J. Wang. On the stability and accuracy of the Spectral Difference method. Journal of Scientific Computing, 37(2):162–188, 2008.

[53] Mehdi R. Khorrami. Chebyshev Spectral Collocation method using a staggered grid for the stability of cylindrical flows. International Journal for Numerical Methods in Fluids, 12(9):825–833, 1991.

[54] D. A. Kopriva. A Staggered-Grid Multidomain Spectral Method for the compressible Navier-Stokes equations. Journal of Computational Physics, 143(1): 125–158, 1998.

[55] A. Suresh and H. T. Huynh. Accurate monotonicity-preserving schemes with Runge-Kutta time stepping. Journal of Computational Physics, 136(1):83–99, 1997.

[56] V. Daru and C. Tenaud. High order one-step monotonicity-preserving schemes for unsteady compressible flow calculations. Journal of Computational Physics, 193(2):563–594, 2004.

[57] Y. Chen and S. Jiang. An optimization-based rezoning for ALE methods. Communications in Computational Physics, 4(5):1216–1244, 2008.

[58] J. S. Peery and D. E. Carroll. Multi-material ALE methods in unstructured grids. Computer Methods in Applied Mechanics and Engineering, 187(3-4): 591–619, 2000.

[59] S. Étienne, A. Garon, and D. Pelletier. Perspective on the geometric conservation law and Finite Element methods for ALE simulations of incompressible flow. Journal of Computational Physics, 228(7):2313–2333, 2009.

[60] J. E. Hicken and D. W. Zingg. Superconvergent functional estimates from Summation-By-Parts Finite-Difference discretizations. SIAM Journal on Scientific Computing, 33(2):893–922, 2011.

[61] M. Svärd. On coordinate transformations for Summation-By-Parts operators. Journal of Scientific Computing, 20(1):29–42, 2004.

[62] K. Mattsson and J. Nordström. Summation-By-Parts operators for Finite Difference approximations of second derivatives. Journal of Computational Physics, 199(2):503–540, 2004.

[63] Z. J. Wang and H. Gao. A unifying Lifting Collocation Penalty formulation including the Discontinuous Galerkin, Spectral Volume/Difference methods for conservation laws on mixed grids. Journal of Computational Physics, 228(21): 8161–8186, 2009.

[64] H. Gao and Z. J. Wang. A high-order Lifting Collocation Penalty formulation for the Navier-Stokes equations on 2d mixed grids. In AIAA, editor, 19th AIAA Computational Fluid Dynamics Conference, 2009.

[65] N. K. Burgess and D. J. Mavriplis. Robust computation of turbulent flows using a Discontinuous Galerkin Method. In 50th Aerospace Sciences Meeting and Exhibit, number 0457, 2012.

[66] F. Bassi, L. Botti, A. Colombo, A. Crivellini, N. Franchina, A. Ghidoni, and S. Rebay. Very high-order accurate Discontinuous Galerkin computation of transonic turbulent flows on aeronautical configurations, volume 113 of Notes on Numerical Fluid Mechanics. 2010.

[67] B. Landmann, M. Kessler, S. Wagner, and E. Krämer. A parallel, high-order Discontinuous Galerkin code for laminar and turbulent flows. Computers and Fluids, 37(4):427–438, 2008.

[68] A.F. Antoniadis, K.H. Iqbal, E. Shapiro, N. Asproulis, and D. Drikakis. Comparison of high-order Finite Volume and Discontinious Galerkin methods on 3D unstructured grids. pages 1886–1889, 2011.

[69] M. Iskandarani, J. C. Levin, B. J. Choi, and D. B. Haidvogel. Comparison of advection schemes for high-order h-p Finite Element and Finite Volume methods. Ocean Modelling, 10(1-2 SPEC. ISS.):233–252, 2005.

[70] X. Nogueira, L. Cueto-Felgueroso, I. Colominas, H. Gómez, F. Navarrina, and M. Casteleiro. On the accuracy of Finite Volume and Discontinuous Galerkin discretizations for compressible flow on unstructured grids. International Journal for Numerical Methods in Engineering, 78(13):1553–1584, 2009.

[71] J. Zhu, J. Qiu, C. Shu, and M. Dumbser. Runge-Kutta Discontinuous Galerkin method using WENO limiters II: Unstructured meshes. Journal of Computational Physics, 227(9):4330–4353, 2008.

[72] M. Zhang and C. W. Shu. An analysis of and a comparison between the Discontinuous Galerkin and the Spectral Finite Volume methods. Computers and Fluids, 34(4-5 SPEC.ISS.):581–592, 2005.

[73] T. Zhou, Y. Li, and C. . Shu. Numerical comparison of WENO finite volume and Runge-Kutta discontinuous Galerkin methods. Journal of Scientific Computing, 16(2):145–171, 2001.

[74] M. Remaki and L. Fezoui. Comparison between Discontinuous Galerkin method and a Finite Volume time-domain method in solving Maxwell equations, in heterogeneous media. Annual Review of Progress in Applied Computational Electromagnetics, 1, 1999.

[75] C.W. Shu. High-order finite difference and finite volume WENO schemes and discontinuous Galerkin methods for CFD. International Journal of Computational Fluid Dynamics, 17(2):107–118, 2003.

[76] J. Cheng and C. W. Shu. High order schemes for CFD: A review. Jisuan Wuli/Chinese Journal of Computational Physics, 26(5):633–655, 2009.

[77] X. Deng, M. Mao, G. Tu, H. Zhang, and Y. Zhang. High-order and high accurate CFD methods and their applications for complex grid problems. Communications in Computational Physics, 11(4):1081–1102, 2012.

[78] T. H. Lê, J.M. Le Gouez, and E. Garnier. High accuracy flow simulations: Advances and challenges for future needs in aeronautics. Computers and Fluids, 43(1):90–97, 2011.

[79] M. Murayama, T. Imamura, K. Yamamoto, and K. Kobayashi. Comparison of Reynolds-averaged Navier-Stokes simulations of multi-element high-lift configurations. Journal of Aircraft, 44(1):175–186, 2007.

[80] Inc. Pointwise. POINTWISE, 2012. URL www.pointwise.com.

[81] Inc Ansys. ANSYS Fluent, 2012. URL http://www.ansys.com.

[82] George Karypis. Metis - serial graph partitioning and fill-reducing matrix ordering, 2006-2011. URL http://glaros.dtc.umn.edu/gkhome/views/metis.

[83] J.F. Thompson, K.Bharat Soni, and P.N. Weatherill. Handbook of Grid Generation. CRC PRESS, Boca Raton, Florida, 1999.

[84] Neal T. Frink. Upwind scheme for solving the Euler equations on unstructured tetrahedral meshes. AIAA Journal, 30(1):70–77, 1992.

[85] B. Diskin, J. L. Thomas, E. J. Nielsen, H. Nishikawa, and J. A. White. Comparison of node-centered and cell-centered unstructured finite-volume discretizations: Viscous fluxes. AIAA Journal, 48(7):1326–1338, 2010.

[86] M. T. Nair and T. K. Sengupta. Orthogonal grid generation for Navier-Stokes computations. International Journal for Numerical Methods in Fluids, 28(2): 215–224, 1998.

[87] P. Tsoutsanis, V. A. Titarev, and D. Drikakis. WENO schemes on arbitrary mixed-element unstructured meshes in three space dimensions. Journal of Computational Physics, 230(4):1585–1601, 2011.

[88] M. Dumbser and M. Käser. Arbitrary high order Non-Oscillatory Finite Volume schemes on unstructured meshes for linear hyperbolic systems. Journal of Computational Physics, 221(2):693–723, 2007.

[89] T.J. Barth and P.O. Frederickson. Higher order solution of the Euler equations on unstructured grids using quadratic reconstruction. AAIA, Aerospace sciences meeting January 1990, 12(90-0013), 1990.

[90] S. K. Godunov. A Finite-Difference method for the numerical computation of discontinuous solutions of the equations of fluid dynamics. Mat. Sb., 47(271), 1959.

[91] B. van Leer. Towards the ultimate conservative difference scheme: A second-order sequel to Godunov's method. Journal of Computational Physics, 32(1): 101–136, 1979.

[92] P. Colella and P. R. Woodward. The Piecewise Parabolic Method (PPM) for gas-dynamical simulations. Journal of Computational Physics, 54(1):174–201, 1984.

[93] N.T. Frink. Recent progress toward a three-dimensional Navier-Stokes solver. AIAA Paper Report, (94-0061), 1994.

[94] T.J. Barth. Numerical aspects of computing high-reynolds number flows on unstructured meshes. AIAA Paper Report, (91-0721), 1991.

[95] L. J. Engquist. Triangle based adaptive stencils for the solution of hyperbolic conservation laws. Journal of Computational Physics, 98(1):64–73, 1992.

[96] B. Perthame. A variant of van Leer's method for multidimensional systems of conservation laws. Journal of Computational Physics, 112(2):370–381, 1994.

[97] A. Jameson and D. Mavriplis. Finite Volume solution of the two-dimensional Euler equations on a regular triangular mesh. AIAA Journal, 24(4):611–618, 1986.

[98] T. Tillaeva. A generalization of the modified Godunov scheme to arbitrary unstructured meshes. Transactions of the Central Aerodynamics Institute, 17 (2):18–26, 1986.

[99] V. Venkatakrishnan. Convergence to steady state solutions of the Euler equations on unstructured grids with limiters. Journal of Computational Physics, 118(1):120–130, 1995.

[100] L. Fezoul and B. Stoufflet. A class of implicit upwind schemes for Euler simulations with unstructured meshes. Journal of Computational Physics, 84(1): 174–206, 1989.

[101] V. Venkatakrishnan and D. J. Mavriplis. Implicit solvers for unstructured meshes. Journal of Computational Physics, 105(1):83–91, 1993.

[102] W. K. Anderson and D. L. Bonhaus. An implicit upwind algorithm for computing turbulent flows on unstructured grids. Computers and Fluids, 23(1):1–21, 1994.

[103] Dartzi Pan and Jen-Chieh Cheng. Second-order upwind Finite-Volume method for the Euler solution on unstructured triangular meshes. International Journal for Numerical Methods in Fluids, 16(12):1079–1098, 1993.

[104] C. Ollivier-Gooch and M. Van Altena. A high-order-accurate unstructured mesh Finite-Volume scheme for the advection-diffusion equation. Journal of Computational Physics, 181(2):729–752, 2002.

[105] L. Cueto-Felgueroso, I. Colominas, X. Nogueira, F. Navarrina, and M. Casteleiro. Finite Volume solvers and Moving Least-Squares approximations for the compressible Navier-Stokes equations on unstructured grids. Computer Methods in Applied Mechanics and Engineering, 196(45-48):4712–4736, 2007.

[106] J. Fürst. A weighted least square scheme for compressible flows. Flow, Turbulence and Combustion, 76(4):331–342, 2006.

[107] X. Nogueira, L. Cueto-Felgueroso, I. Colominas, F. Navarrina, and M. Casteleiro. A new shock-capturing technique based on Moving Least Squares for higher-order numerical schemes on unstructured grids. Computer Methods in Applied Mechanics and Engineering, 199(37-40):2544–2558, 2010.

[108] M Delanaye and Y. Liu. Quadratic reconstruction Finite Volume schemes on 3D arbitrary unstructured polyhedral grids. AIAA Report, (Paper No. 99-3259-CP), 1999.

[109] C. F. Ollivier-Gooch. Quasi-ENO schemes for unstructured meshes based on unlimited data-dependent least-squares reconstruction. Journal of Computational Physics, 133(1):6–17, 1997.

[110] S. K. Godunov. Different Methods for Shock Waves. PhD thesis, Moscow State University, 1954.

[111] S. K. Godunov. A difference method for numerical calculation of discontinuous solutions of the equations of hydrodynamics. Mat. Sb. (N.S.), (47(89):3): 271Ű306, 1959.

[112] C. Shu and S. Osher. Efficient implementation of essentially non-oscillatory shock-capturing schemes. Journal of Computational Physics, 77(2):439–471, 1988.

[113] P. K. Sweby. High resolution schemes using flux limiters for hyberbolic conservation laws. SIAM Journal on Numerical Analysis, 21(5):995–1011, 1984.

[114] T. Tanaka. Finite volume TVD scheme on an unstructured grid system for three-dimensional MHD simulation of inhomogeneous systems including strong background potential fields. Journal of Computational Physics, 111(2):381–389, 1994.

[115] M.E. Hubbard. Multidimensional slope limiters for MUSCL-type finite volume schemes on unstructured grids. Journal of Computational Physics, 155(1):54–74, 1999.

[116] M. S. Darwish and F. Moukalled. TVD schemes for unstructured grids. International Journal of Heat and Mass Transfer, 46(4):599–611, 2003.

[117] D. V. Patil and K. N. Lakshmisha. Finite volume TVD formulation of lattice boltzmann simulation on unstructured mesh. Journal of Computational Physics, 228(14):5262–5279, 2009.

[118] S. Spekreijse. Multigrid solution of monotone second-order discretizations of hyperbolic conservation laws. Mathematics of computation, 49(179):135–155, 1987.

[119] J. B. Goodman and R. LeVeque. A geometric approach to high resolution TVD schemes. SIAM Journal of Numerical Analysis, 25(2):268–284, 1988.

[120] CD-adapco. STAR-CCM+, 2012. URL http://www.cd-adapco.com/products/star_ccm_plus/.

[121] OpenCFD Ltd (ESI Group). Open source cfd toolbox, 2004-2012. URL http://www.openfoam.com/.

[122] G. D. van Albada, B. van Leer, and W.W. Roberts. A comparative study of computational methods in cosmic gas dynamics. Astronomy and Astrophysics, 108,1:76–84, 1982.

[123] D. S. Balsara and C. W. Shu. Monotonicity preserving weighted essentially non-oscillatory schemes with increasingly high order of accuracy. Journal of Computational Physics, 160(2):405–452, 2000.

[124] J. Shi, C. Hu, and C. Shu. A technique of treating negative weights in WENO schemes. Journal of Computational Physics, 175(1):108–127, 2002.

[125] Y. T. Zhang and C. W. Shu. Third order WENO scheme on three dimensional tetrahedral meshes. Communications in Computational Physics, 5(2-4):836–848, 2009.

[126] M. Dumbser. Arbitrary high order pnpm schemes on unstructured meshes for the compressible navier-stokes equations. Computers and Fluids, 39(1):60–76, 2010.

[127] V. A. Titarev, P. Tsoutsanis, and D. Drikakis. WENO schemes for mixed-element unstructured meshes. Communications in Computational Physics, 8 (3):585–609, 2010.

[128] V. A. Titarev and D. Drikakis. Uniformly high-order schemes on arbitrary unstructured meshes for advection-diffusion equations. Computers and Fluids, 2010. Article in Press.

[129] J. Qiu and C. W. Shu. Hermite WENO schemes and their application as limiters for Runge-Kutta discontinuous Galerkin method II: Two dimensional case. Computers and Fluids, 34(6):642–663, 2005.

[130] W. R. Wolf and J. L. F. Azevedo. High-order ENO and WENO schemes for unstructured grids. International Journal for Numerical Methods in Fluids, 55 (10):917–943, 2007.

[131] O. Friedrich. Weighted essentially non-oscillatory schemes for the interpolation of mean values on unstructured grids. Journal of Computational Physics, 144 (1):194–212, 1998.

[132] M. Dumbser, M. Käser, V. A. Titarev, and E. F. Toro. Quadrature-free non-oscillatory finite volume schemes on unstructured meshes for nonlinear hyperbolic systems. Journal of Computational Physics, 226(1):204–243, 2007.

[133] V. A. Titarev and E. F. Toro. Finite-volume WENO schemes for three-dimensional conservation laws. Journal of Computational Physics, 201(1):238–260, 2004.

[134] D. A. Dunavant. High degree efficient symmetrical gaussian quadrature rules for the triangle. International Journal for Numerical Methods in Engineering, 21(6):1129–1148, 1985.

[135] G. R. Cowper. Gaussian quadrature formulas for triangles. International Journal for Numerical Methods in Engineering, Vol. 7-3:405–408, 1973.

[136] Eleuterio F. Toro. Riemann Solvers and Numerical Methods for Fluid Dynamics. Springer, third edition, 2009.

[137] J. Blazek. Computational Fluid Dynamics: Principles and Applications. Elsevier Science Ltd, Kidlington, Oxford, UK, 2001.

[138] E. F. Toro, M. Spruce, and W. Speares. Restoration of the contact surface in the hll-riemann solver. Shock Waves, 4(1):25–34, 1994.

[139] K Sharov, D. Nakahashi. Low speed preconditioning and LU-SGS scheme for 3-D viscous flow computations on unstructured grids. AIAA Paper Report, (98-0614), 1998.

[140] A. Haselbacher and J. Blazek. Accurate and efficient discretization of Navier-Stokes equations on mixed grids. AIAA Journal, 38(11):2094–2102, 2000.

[141] G. Gassner, F. Lörcher, and C.D. Munz. A discontinuous galerkin scheme based on a space-time expansion ii. viscous flow equations in multi dimensions. Journal of Scientific Computing, 34(3):260–286, 2008.

[142] G. Gassner, F. Lörcher, and C.D. Munz. A contribution to the construction of diffusion fluxes for finite volume and discontinuous Galerkin schemes. Journal of Computational Physics, 224(2):1049–1063, 2007.

[143] D. Drikakis and W. Rider. High-Resolution Methods for Imcompressible and Low-Speed Flows. Springer-Verlag Berlin Heidelberg, 2005.

[144] D. L. Whitfield and J. M. Janus. Three-dimensional unsteady Euler equations solution using flux vector splitting. In AIAA Paper, 1984.

[145] K. A. Hoffmann and S. T. Chiang. Computational Fluid Dynamics. Engineering Education System, 4th edition, 2000.

[146] P. Moin and K. Mahesh. Direct numerical simulation: A Tool in Turbulence Research, volume 30 of Annual Review of Fluid Mechanics. 1998.

[147] M. J. Boussinesq. Memoire sur l'influence des frottements dans les mouvements reguliers des fluides. Journal des mathematiques pures et appliquees, 13(2): 377–424, 1868.

[148] S. E. Rogers, F. Menter, P. A. Durbin, and N. N. Mansour. A comparison of turbulence models in computing multi-element airfoil flows. AIAA Journal, (94-0291), 1994.

[149] J. E. Bardina, P.G. Huang, and T. J. Coakley. Turbulence modeling validation, testing, and development. NASA Technical Memorandum, (110446), 1997.

[150] P. R. Spalart and S. R. Allmaras. One-equation turbulence model for aerodynamic flows. Recherche aerospatiale, (1):5–21, 1994.

[151] J. R. Edwards and S. Chandra. Comparison of eddy viscosity-transport turbulence models for three-dimensional, shock-separated flowfields. AIAA Journal, 34(4):756–763, 1996.

[152] N.C Nguyen, Per-O. Persson, and J. Peraire. RANS solutions using high-order Discontinuous Galerkin methods. In AIAA, editor, Aerospace Sciences Meeting and Exhibit, number AIAA 2007-914, Reno, Nevada, January 2007.

[153] T.A. Oliver and D.L. Darmofal. An unsteady adaptation algorithm for Discontinuous Galerkin discretizations of the RANS equations. In AIAA, editor, Aerospace Sciences Meeting and Exhibit, number AIAA 2007-3940, Miami, Florida, June 2007.

[154] A. O. Todd. A high-order, Adaptive, Discontinuous Galerkin Finite Element Method for the Reynolds-Averaged Navier-Stokes Equations. PhD thesis, Massachusetts Institute of Technology, 2008.

[155] R. Rudnik, S. Melber, A. Ronzheimer, and O. Brodersen. Three-dimensional Navier-Stokes simulations for transport aircraft high-lift configurations. Journal of Aircraft, 38(5):895–903, 2001.

[156] O. Brodersen, B. Eisfeld, J. Raddatz, and P. Frohnapfel. DLR results from the third AIAA computational fluid dynamics drag prediction workshop. Journal of Aircraft, 45(3):823–836, 2008.

[157] R. P. Dwight. Efficiency improvements of RANS-based analysis and optimization using implicit and adjoint methods on unstructured grids. PhD thesis, University of Manchester,UK, 2006.

[158] P. Keast. Moderate-degree tetrahedral quadrature formulas. Computer Methods in Applied Mechanics and Engineering, 55(3):339–348, 1986.

[159] S. Catris and B. Aupoix. Density corrections for turbulence models. Aerospace Science and Technology, 4(1):1–11, 2000.

[160] S. Deck, P. Duveau, P. D'Espiney, and P. Guillen. Development and application of Spalart-Allmaras one equation turbulence model to three-dimensional supersonic complex configurations. Aerospace Science and Technology, 6(3):171–183, 2002.

[161] M. E. Brachet, U. Frisch, D. I. Meiron, S. A. Orszag, B. G. Nickel, and R. H. Morf. Small-scale structure of the Taylor-Green vortex. Journal of Fluid Mechanics, 130 , May 1983:411–452, 1983.

[162] J. P. Boris, F. F. Grinstein, E. S. Oran, and R. L. Kolbe. New insights into large eddy simulation. Fluid Dynamics Research, 10(4-6):199–228, 1992.

[163] P. Sagaut. Large Eddy Simulation for Incompressibe Flows. Springer - Scientific Compution, Berlin, Germany, 2006.

[164] J. P. Boris. On large eddy simulation using subgrid turbulence models. Springer, New York, USA, in j.l. lumley (ed.), whither turbulence? turbulence at the crossroads edition, 1990.

[165] D. Drikakis, M. Hahn, A. Mosedale, and B. Thornber. Large eddy simulation using high-resolution and high-order methods. Philosophical Transactions of the Royal Society A: Mathematical, Physical and Engineering Sciences, 367(1899): 2985–2997, 2009.

[166] S. Hickel, N.A. Adams, and J.A. Domaradzki. Letter to the Editor: On the evolution of dissipation rate and resolved kinetic energy in ALDM simulations of the Taylor-Green flow. Journal of Computational Physics, 229(6):2422–2423, 2010.

[167] M. E. Brachet. Direct simulation of three-dimensional turbulence in the Taylor-Green vortex. Fluid Dynamics Research, 8(1-4):1–8, 1991.

[168] C. Shu, W. Don, D. Gottlieb, O. Schilling, and L. Jameson. Numerical convergence study of nearly incompressible, inviscid Taylor-Green vortex flow. Journal of Scientific Computing, 24(1):569–595, 2005.

[169] B. Thornber, A. Mosedale, and D. Drikakis. On the implicit large eddy simulations of homogeneous decaying turbulence. Journal of Computational Physics, 226(2):1902–1929, 2007.

[170] F. F. Grinstein and D. Drikakis. Computing turbulent flow dynamics with implicit large eddy simulation. Journal of Fluids Engineering, Transactions of the ASME, 129(12):1481–1482, 2007.

[171] U. Frisch. Turbulence - The Legacy of A.N. Kolmogorov. 1995. Chapter 5.1.

[172] G. Haller. An objective definition of a vortex. Journal of Fluid Mechanics, 525: 1–26, 2005.

[173] D. Drikakis, C. Fureby, F. F. Grinstein, and D. Youngs. Simulation of transition and turbulence decay in the Taylor-Green vortex. Journal of Turbulence, 8:1–12, 2007.

[174] Schmitt V. and Charpin. Pressure distributions on the ONERA-M6-WING at transonic mach numbers. Office National D' Etudes et de Recherces Aerospatiales, 1979.

[175] P. Furmanek, J. Dobes, J. Furst, J. Fort, M. Kladrubsky, and K. Kozel. Numerical simulations of 3D transonic inviscid flow over a swept wing. In Proceedings of the CzechŰJapanese Seminar in Applied Mathematics 2008, pages 31–39, Miyazaki, Japan, 2008.

[176] Z. Qian and C. H. Lee. A class of large time step Godunov schemes for hyperbolic conservation laws and applications. Journal of Computational Physics, 230(19):7418–7440, 2011.

[177] Z. Qian and C. H. Lee. On large time step TVD scheme for hyperbolic conservation laws and its efficiency evaluation. Journal of Computational Physics, 231(21):7415–7430, 2012.

[178] A. Dadone and B. Grossman. Ghost-cell method for analysis of inviscid three-dimensional flows on Cartesian-grids. Computers and Fluids, 36(10):1513–1528, 2007.

[179] Rainald Lohner and Paresh Parikh. Generation of three-dimensional unstructured grids by the advancing-front method. International Journal for Numerical Methods in Fluids, 8(10):1135–1149, 1988.

[180] H. Luo, J. R. Edwards, D. L. Stefanski, and S. C. Spiegel. On the computation of compressible flows on unstructured hybrid grids. In 47th AIAA Aerospace Sciences Meeting, number 2009-14/4, Orlando Florida, 2009.

[181] AGARD Working Group 07. Test cases for inviscid flow field methods. Technical Report AGARD-AR-211, 1985.

[182] M. O. Bristeau, R. Glowinski, and J. Periaux. Numerical methods for the Navier-Stokes equations. applications to the simulation of compressible and incompressible viscous flows. Computer Physics Reports, 6(1-6):73–187, 1987.

[183] S.R. Allmars. Contamination of laminar boundary layers by artificial dissipation in NavierŰStokes solutions. Numerical Methods for Fluid Dynamics, Clarendon Oxford, UK, edited by m.j.baines and k.w. morton edition, 1993.

[184] H. Blasius. Grenzschichten in flussigkeiten mit kleiner reibung (boundary layers in fluids with low friction). Z . Math. Physik, 56(1), 1908.

[185] H Schlichting. Boundary-Layer Theory. McGraw-Hill Book Company, seventh edition, 1979.

[186] S. Liao. An explicit, totally analytic approximate solution for Blasius' viscous flow problems. International Journal of Non-Linear Mechanics, 34(4):759–778, 1999. Cited By (since 1996): 224.

[187] J. He. Approximate analytical solution of Blasius' equation. Communications in Nonlinear Science and Numerical Simulation, 4(1):75–78, 1999.

[188] I. K. Khabibrakhmanov and D. Summers. The use of generalized Laguerre polynomials in spectral methods for nonlinear differential equations. Computers and Mathematics with Applications, 36(2):65–70, 1998.

[189] J. Lin. A new approximate iteration solution of Blasius equation. Communications in Nonlinear Science and Numerical Simulation, 4(2):91–94, 1999.

[190] L. Wang. A new algorithm for solving classical Blasius equation. Applied Mathematics and Computation, 157(1):1–9, 2004.

[191] F. M. Allan and M. I. Syam. On the analytic solutions of the nonhomogeneous Blasius problem. Journal of Computational and Applied Mathematics, 182(2): 362–371, 2005.

[192] L. Yu and C. Chen. The solution of the Blasius equation by the differential transformation method. Mathematical and Computer Modelling, 28(1):101–111, 1998.

[193] A. Wazwaz. The variational iteration method for solving two forms of Blasius equation on a half-infinite domain. Applied Mathematics and Computation, 188(1):485–491, 2007.

[194] S. Abbasbandy. A numerical solution of Blasius equation by Adomian's decomposition method and comparison with homotopy perturbation method. Chaos, Solitons and Fractals, 31(1):257–260, 2007.

[195] F. Ahmad and W. H. Al-Barakati. An approximate analytic solution of the Blasius problem. Communications in Nonlinear Science and Numerical Simulation, 14(4):1021–1024, 2009.

[196] T. Tajvidi, M. Razzaghi, and M. Dehghan. Modified rational legendre approach to laminar viscous flow over a semi-infinite flat plate. Chaos, Solitons and Fractals, 35(1):59–66, 2008.

[197] D. Meksyn. New Methods in Laminar Boundary-layer Theory. Pergamon Press, Bath, UK, 1961.

[198] D. Drikakis and S. Tsangaris. On the solution of the compressible navier- stokes equations using improved flux vector splitting methods. Applied Mathematical Modelling, 17(6):282–297, 1993.

[199] Massachusetts Institute of Technology Aerospace Computational Design Laboratory. MSES, multi-element airfoil design/analysis software, May 1994. URL http://raphael.mit.edu/research.html.

[200] R. M. Kirby, T. C. Warburton, I. Lomtev, and G. E. Karniadakis. Discontinuous Galerkin spectral/hp method on hybrid grids. Applied Numerical Mathematics, 33(1):393–405, 2000.

[201] M. Breuer. Large eddy simulation of the subcritical flow past a circular cylinder: Numerical and modeling aspects. International Journal for Numerical Methods in Fluids, 28(9):1281–1302, 1998.

[202] J. C. Chassaing, S. Khelladi, and X. Nogueira. Accuracy assessment of a high-order moving least squares finite volume method for compressible flows. Computers and Fluids, 71:41–53, 2012.

[203] A. Haselbacher. A Grid-Transparent numerical method for compressible viscous flows on mixed unstructured grids. PhD thesis, Loughborough University,UK, 1999.

[204] P.C. Walsh. Adaptive Solution of Viscous Aerodynamic Flows Using Unstructured Grids. PhD thesis, University of Toronto, 1998.

[205] M.L. Lutton. Comparison of C- and O- Grid generation methods using a NACA-0012 airfoil. PhD thesis, Air University, USA, 1989.

[206] D. W. Zingg, S. De Rango, M. Nemec, and T. H. Pulliam. Comparison of several spatial discretizations for the Navier-Stokes equations. Journal of Computational Physics, 160(2):683–704, 2000.

[207] R. H. Nichols. Turbulence models and their application to comlpex flows. Technical Report Revision 4.01, University of Alabama at Birmingham.

[208] C.L. Rumsey. Cfl3d test/validation cases - nasa langley geometry laboratory, August 2012. URL http://cfl3d.larc.nasa.gov/Cfl3dv6/cfl3dv6_testcases.html#n0012.

[209] P. Woodward and P. Colella. The numerical simulation of two-dimensional fluid flow with strong shocks. Journal of Computational Physics, 54(1):115–173, 1984.

[210] D. S. Balsara. Von Neumann stability analysis of smoothed particle hydrodynamics - suggestions for optimal algorithms. Journal of Computational Physics, 121(2):357–372, 1995.

[211] A. M. O. Smith. High-lift aerodynamics. Journal of Aircraft, 12(6):501–530, 1975.

[212] N. Kroll and Z.J. Wang. 1st international workshop on high-order cfd methods, January 2012. URL http://zjw.public.iastate.edu/hiocfd.html.

[213] F. W. Spaid. High reynolds number, multielement airfoil flowfield measurements. Journal of Aircraft, 37(3):499–507, 2000.

[214] C. L. Rumsey, E. M. Lee-Rausch, and R. D. Watson. Three-dimensional effects in multi-element high lift computations. Computers and Fluids, 32(5):631–657, 2003.

[215] W. K. Anderson, Daryl L. Bonhaus, Robert J. McGhee, and Betty S. Walker. Navier-Stokes computations and experimental comparisons for multielement airfoil configurations. Journal of Aircraft, 32(6):1246–1253, 1995.

[216] S. Kim, J. J. Alonso, and A. Jameson. Multi-element high-lift configuration design optimization using viscous continuous adjoint method. Journal of Aircraft, 41(5):1082–1097, 2004.

[217] P. L. Roe. Approximate Riemann solvers, parameter vectors, and difference schemes. Journal of Computational Physics, 43(2):357–372, 1981.

[218] V.V. Rusanov. Calculation of interaction of non-steady shock waves with obstacles. J. Comput. Math. Phys., 1(USSR):267–279, 1961.

[219] D. A. Burgess and M. B. Giles. Renumbering unstructured grids to improve the performance of codes on hierarchical memory machines. Advances in Engineering Software, 28(3):189–201, 1997.

[220] D. S. Dolling. Fifty years of shock-wave/boundary-layer interaction research: What next? AIAA Journal, 39(8):1517–1531, 2001.

[221] L. F. Henderson. The reflexion of a shock wave at a rigid wall in the presence of a boundary layer. Journal of Fluid Mechanics, 30, part 4:699–722, 1967.

[222] E. Schülein. Skin-friction and heat flux measurements in shock/boundary-layer interaction flows. AIAA Journal, 44(8):1732–1741, 2006.

[223] Y. Andreopoulos, J. H. Agui, and G. Briassulis. Shock wave-turbulence interactions, volume 32 of Annual Review of Fluid Mechanics. 2000.

[224] G.A. Gerolymos, E. Sauret, and I. Vallet. Oblique-shock-wave/boundary-layer interaction using near-wall reynolds stress models. AIAA Journal, 42(6):1089–1100, 2004.

[225] F. Grasso and M. Marini. Analysis of hypersonic shock-wave laminar boundary-layer interaction phenomena. Computers and Fluids, 25(6):561–581, 1996.

[226] F. Grasso, M. Marini, G. Ranuzzi, S. Cuttica, and B. Chanetz. Shock-wave/turbulent boundary-layer interactions in nonequilibrium flows. AIAA Journal, 39(11):2131–2140, 2001.

[227] S. Pirozzoli and F. Grasso. Direct numerical simulation of impinging shock wave/turbulent boundary layer interaction at m=2.25. Physics of Fluids, 18(6), 2006.

[228] M. Morkovin. Effects of compressibility on turbulent flows. Mecanique de le Turbulence, pages 367–380, 1964.

[229] X. Xiao, H. A. Hassan, J. R. Edwards, and R. L. Gaffney Jr. Role of turbulent Prandtl numbers on heat flux at hypersonic mach numbers. AIAA Journal, 45 (4):806–813, 2007.

[230] J.-P. Dussauge, P. Dupont, and J.-F. Debiève. Unsteadiness in shock wave boundary layer interactions with separation. Aerospace Science and Technology, 10(2):85–91, 2006.

[231] N. N. Fedorova and I.A. Fedrochenko. Computations of interaction of incident oblique shock-wave with a turbulent boundary layer on a flat plate. Journal of Applied Mechanics and Technical Physics, 45(3):358–366, 2004.

[232] A.P. Amjad and Krishne n.S. Shock-unsteadiness model applied to oblique shock wave-turbulent boundary-layer interaction. International Journal of Computational Fluid Dynamics, 22(8):569–582, 2008.

[233] D. Moro, N.C. Nguyen, and J. Peraire. Navier-Stokes solution using hybridizable discontinuous Galerkin methods. In AIAA, editor, 20th Computational Fluid Dynamics conference, number AIAA 2011-3407, Honolulu, Hawaii, June 2011.

[234] T.A Oliver and D.L. Darmofal. Impact of turbulence model irregularity on high-order discretizations. In AIAA, editor, 47th AIAA Aerospace Sciences Meeting Including The New Horizons Forum and Aerospace Exposition, number AIAA 2009-953, Orlando, Florida, January 2009.

[235] M. G. Edwards. Higher resolution hyperbolic-coupled-elliptic flux-continuous CVD schemes on structured and unstructured grids in 3-D. International Journal for Numerical Methods in Fluids, 51(9-10):1079–1095, 2006.

[236] M. Dumbser and O. Zanotti. Very high order PNPM schemes on unstructured meshes for the resistive relativistic MHD equations. Journal of Computational Physics, 228(18):6991–7006, 2009.

[237] J. Hua, J. F. Stene, and P. Lin. Numerical simulation of 3D bubbles rising in viscous liquids using a front tracking method. Journal of Computational Physics, 227(6):3358–3382, 2008.

[238] A. Burbeau and P. Sagaut. A dynamic p-adaptive discontinuous Galerkin method for viscous flow with shocks. Computers and Fluids, 34(4-5 SPEC.ISS.): 401–417, 2005.

CHAPTER 9

Appendix

9.1 Projection of the Inviscid Flux Tensor

The projection of the inviscid flux tensor of the Euler equations computed at the average state is the Jacobian matrix J_j which is given by

$$\mathrm{J}_j = \frac{\partial \vec{F}^c_{\hat{n}}}{\partial \vec{W}} = \begin{bmatrix} 0 & 1 & 0 & 0 & 0 \\ (\gamma-1)\,h - u^2 - a^2 & (3-\gamma)\,u & -(\gamma-1)\,v & -(\gamma-1)\,w & (\gamma-1) \\ -uv & v & u & 0 & 0 \\ -uw & w & 0 & u & 0 \\ \frac{1}{2}u\left[(\gamma-3)\,h - a^2\right] & h-(\gamma-1)\,u^2 & -(\gamma-1)\,uv & -(\gamma-1)\,uw & \gamma u \end{bmatrix} \tag{9.1.1}$$

where h is the enthalpy given by

$$h = (E+p)/\rho = \frac{1}{2}\mathcal{V}^2 + \frac{a^2}{(\gamma-1)} \tag{9.1.2}$$

where a is the speed of sound given by

$$a = \sqrt{\frac{\gamma p}{\rho}} \tag{9.1.3}$$

the right eigenvectors R_j is defined as

$$\mathrm{R}_j = \begin{bmatrix} 1 & 1 & 0 & 0 & 1 \\ u-a & u & 0 & 0 & u+a \\ v & v & 1 & 0 & v \\ w & w & 0 & 1 & w \\ h-ua & \frac{1}{2}\mathcal{V}^2 & v & w & h+ua \end{bmatrix} \tag{9.1.4}$$

and the left eigenvectors L_j written as

$$\mathrm{L}_j = \frac{(\gamma-1)}{2a^2} \begin{bmatrix} h+\frac{a}{(\gamma-1)}(u-a) & -\left(u-\frac{a}{(\gamma-1)}\right) & -v & -w & 1 \\ -2h+\frac{4}{(\gamma-1)}a^2 & 2u & 2v & 2w & -2 \\ -\frac{2va^2}{(\gamma-1)} & 0 & \frac{2a^2}{(\gamma-1)} & 0 & 0 \\ -\frac{2wa^2}{(\gamma-1)} & 0 & 0 & \frac{2a^2}{(\gamma-1)} & 0 \\ h-\frac{a}{(\gamma-1)}(u-a) & -u+\frac{a}{(\gamma-1)} & -v & -w & 1 \end{bmatrix} \tag{9.1.5}$$